

Design and Analysis of a **Distributed TRIC** **Concept Seamless** **Smart Morphing Wing**

Technische Universiteit Delft

N.R. Thakrar

Design and Analysis of a Distributed TRIC Concept Seamless Smart Morphing Wing

by

N.R. Thakrar

to obtain the degree of Master of Science

at the Delft University of Technology,

to be defended publicly on Friday November 27, 2020 at 1:00 PM.

Student number: 4916514
Project duration: November 1, 2019 – November 27, 2020
Thesis committee: Dr. ir. R. De Breuker, TU Delft, supervisor
Dr. J. Sodja, TU Delft, supervisor
Ir. T. Mkhoyan, TU Delft, supervisor
Dr. ir. O.K. Bergsma, TU Delft
Dr. ir. D.M.J. Peeters TU Delft

An electronic version of this thesis is available at <http://repository.tudelft.nl/>.

Abstract

This thesis embarked upon establishing and verifying a design process to build and control a seamlessly distributed smart TRIC concept morphing wing to achieve simultaneous load alleviation, flutter suppression and drag minimization capabilities. A $1.8m$ span, by $0.5m$ chord morphing wing with six independent trailing edge morphing modules, that were seamlessly connected with a silicone elastomer was designed and built. In addition, a surrogate model of a single morphing module was built to predict increments in the lift for provided actuation inputs and angles of attack. This wing, designated the title Smart-X Alpha, was tested at the TU Delft Open Jet Facility.

The design and surrogate modelling work of the main wing structure was based on the foundations of a static aeroelastic simulation model that was built to consider the fluid-structure interaction between the wing and surrounding airflow. The simulation model interfaced MSC NASTRAN with XFOIL in an iterative simulation loop used to define the static aeroelastic equilibrium shape of the wing structure for the given aerodynamic environment, using aerodynamic strip model assumptions. A laminate design optimized for minimal actuation loads was found by introducing the NASTRAN optimization solver (SOL200) into the aeroelastic analysis framework. A variable thickness woven fibre-glass laminate structure was found with this analysis, which could be actuated by the VOLZ DA22-12-4112 servo motors. The surrogate model was built with the coupling of the linear structural solver (SOL101) with an inviscid flow model in XFOIL to be able to provide a mapping of actuation inputs and angle-of-attack to an increment in the lift, relative to the baseline undeformed shape of the wing.

The integration of the silicone elastomer system to connect modules was designed with analysis and testing of several design concepts in a trial and error fashion. The first design iterations were simulated within ABAQUS, followed by conducting further testing on printed prototypes to better assess performance parameters that were not captured within simulation due to difficulties with convergence. This process honed in on a design that was integrated onto the final morphing wing structure, enabling distributed morphing with seamless skin continuity.

The complete design and analysis work carried out was additionally validated against measured test results from the digital image correlation tests on a single wing module. Results showed that the designed morphing range was not entirely possible due to compliance in the TRIC mechanism; however, strong correlations in deformations were witnessed for matching trailing edge tip deflections between simulated and measured results for camber morphing conditions. Further testing on the influence of the flexible silicone system showed that the independent morphing range was compromised when the actuators would attempt to morph the wing upwards, relative to an adjacent module which is morphed down. The downwards morphing range was only partially compromised.

From work conducted, further recommendations were made to enhance the design and analysis framework to overcome the compliances of the TRIC interface, improve the skin continuity design and increase accuracies of the surrogate model.

Acknowledgements

On the front page, only one name is engraved to the thesis that of the author's but it must be said that one name is many too less to associate the success of this work to.

It cannot be understated enough that the work completed to reach this end goal was only made possible by the multitude of the effort of so many crucial people. This report will never even come close to conveying the love, motivation, sacrifices, compromises and endeavours put forward by so many people to make it's completion possible. Still, we will certainly do our best to capture it in the acknowledgements. I can only hope that every reader who appreciates the work of this thesis takes the time to read off all the fantastic people who made it come together.

My first acknowledgement has to go to my immediate supervisor, PhD—candidate Tigran Mkhoyan. Words will never describe the level of contribution put forward by Tigran to drive the development of the Smart-X Alpha wing to unequivocal successes in its first year of creation. This has only benefited me in my future endeavours. The time and energy Tigran committed into not only this project, but into my personal development, no matter the time of day will always go above and beyond what is required from a supervisor. I will always appreciate and cherish his selfless investment to make me a better student and person.

An exceptional dreamer in a supervisor has to be balanced by the extraordinary realist, who will provide the direction to reach the goals that are set out. This is where Dr. Jurij Sodja was the perfect grounding to our team of three. Jurij's knowledge and direction underpinned the successes of the works carried out here. His ability to guide and direct ensured that I was never a deer-in-headlights, not knowing where to go. I always had a clear foresight on this thesis because of Jurij, and this is why so much was achieved in such a short time-frame.

Crossing paths with these two outstanding supervisors was the workings of the brilliant mind of Associate Professor Roeland De Breuker. I will always cherish the first meeting where this topic was proposed to me. A simple question was asked as a test to see if I was up to the task of taking this project on: In the TV show FRIENDS "What is Ross' pager number". I would never have expected that knowing the answer was "55JIMBO" would mean I undertake a sensational project. Of course, Roeland knew better than to make the basis of this decision over a question about FRIENDS. Still, when asked, I will always say I got the chance to work on this thesis because I loved the TV show FRIENDS. Roeland's mind is impeccable, and even though my interactions with him were limited, I will always appreciate that his thought process put the right people together to achieve something amazing.

There is, of course, more of a story that is built around achieving this work. This is because of the contributions of people out there, selflessly giving up their heart and soul for you to get ahead in the world. None more other than my parents, Priti and Rashmin Thakrar. If you are lucky enough to have parents who make it a priority for you to get ahead, you can never take that for granted. Looking beyond the years spent with the personal sacrifice to care for you, and to build savings to support you on your journey to complete a master's degree, the constant support they have given is unsurmountable. Their contributions to my success can never be overlooked.

It is without a doubt that a master thesis will take a mental toll on you. Although, if you are as fortunate as me, you will have the best of friends who will be there for you in times of hardship to get you through it. They will motivate, support you and cheer you on to be able to achieve.

In my team of exceptional friends, I have the amazing Anna Carolina Darboven, Antonio Johman, Alex De Bont, Alex Kasses, Haisam Daouk, Madeleine Bartlett, Nina Hübner, Sushruta Kokkula and Thom

van den Homberg. These are only names of the few of many, but their sacrifices and contributions to supporting me were too important to not acknowledge.

Anna Carolina has been the non-stop cheerleader, the shoulder to cry on, the motivator for my work, always. Her esteemed commitment to my wellbeing and tolerance to my stubbornness has been one of the key reasons I was able to survive the mental toll that came about with treachery that is a master thesis. As often as our interactions can be remote, conversations with Anna always were a source of comfort which I will never take for granted. Rarely, a person can so easily make you happy just from a simple interaction, but I was so lucky to have that in Anna.

I have to thank my TU clan Antonio Johman and Alex Kasses. If you'd know me, you'd know that I'm the guy who does too much and then has no time for anything. This means come actually doing university work, I was unbelievably behind. Lucky for me, Alex and Antonio kept me afloat, when I was drowning in work from every direction. Their genuine friendship, support and tolerance of my schedule and whining has meant so much to me. They are the reason that I was able to even get to point in the curriculum to be able to start a thesis. Without their efforts, I can honestly see myself taking many more years finishing this degree.

Haisam is one of the best housemates, friend and advisers you can ever ask for in a single person. It goes without saying that when you embark on a thesis, your state of personal wellbeing deteriorates, mentally and physically. Your immediate priority will always be meeting the deadlines, but there is only so much you can do by yourself before your mind and body is exhausted. With Haisam, this limit was reached so much later as I could always count on him when I was physically unable to take care of myself. Whether it was having some of the best meals for dinner, or an impeccably clean house which kept your spirits high, and the fun in our conversations, he kept me afloat physically even when I couldn't do the same for myself. In times of COVID, interactions with your housemates are all you have, so you certainly have to be as lucky as I was to have a good friend in a housemate.

Maddy was my source of home away from home. Taking on not only a new degree, but doing it in a new country with new cultures, new challenges and new people, there was always going to be some very tough days. Yet, it was always more comfortable and nicer to have my best friend keeping me grounded, supporting me, providing me with the right advice to adult and listening to my heartaches with no judgement at all.

Now let's be frank. The frankest of conversations are had with people who are the most comfortable people in the world. They are also one of the most fun. This was Nina to me. It will be hard to convey to the reader the conversations and discussions we will have had to more often than not just help me figure out life. If we categorized the topic of discussion as sorting out an existential dilemma, having Nina in my life meant that I could never stop having fun trying to figure out these dilemmas. It is without a doubt that I can say if she wasn't there to help me figure out life, I'm not so sure we would have finished this thesis.

Sushruta, or let's say Sushi. Well, words just can't really describe her can they? The spirit, enthusiasm, joy and love that pocket rocket has brought to me has been unbelievable. Sometimes she'll be the stand-in mom, making sure I eat and sleep; sometimes she'll be my partner in crime, being just as immature as me; sometimes she'll be life adviser, but always she'll be the person keeping me smiling on the worst of days. The bedrock to my adventurous life, she just kept me happy.

When I started this master's, I was optimistic, thinking I could work on this and a dream team. Mistakes in a way were certainly made; the work involved was crazy, with many sleepless nights. Even then, I will still be graduating with no regrets because I will have met Thom and Alex. If you think you've met someone genuinely nice, I will question it, unless you have met Thom and Alex. They started off as being my teammates but ended up as some of my closest friends. Their sheer support of me to handle a thesis and dream-team was the reason that I was able to do both. The work I couldn't do for the dream-team, they had to take on. This meant, if I wasn't sleeping, they were extra not sleeping, to pick up my slack. I can't thank them enough in not just doing this to help me, but now continuing on to be some of my closest friends who continue to provide me with judgement free life advise.

Final acknowledgements have to go towards my current boss and mentor Vincent Peters, providing me with the flexibility in employment to work on my thesis at the same time. To Vincent Stuber for being a great partner in the Smart-X project to help see it to award-winning success, beyond having some great conversations from which I will have learnt a lot. To Sherry Wang and Irèn Mkhoyan for supporting the wind-tunnel testing campaign. To Martin Weberschock, who without a doubt managed the production of the Smart-X wing so well, that only with his direction and capabilities could it have been an award winner. To Nakash Nazeer and George Wijnschenk Dom for supporting the Smart-X design work. To Paul Lancelot in being my go-to advisor on everything NASTRAN. To Silverwing, James Murdza and Victor Sonneveld for being some great friends, managers, teammates and providers of one of the best life experiences I have had. To Victor Horbowiec and Fred Bosch for being great advisors and support for everything composites in the DASML.

Honestly, let's call this the tip of the iceberg of people helping me to my successes. There were so many more who will have helped me, and to everyone involved thank you. I am graduating as a very satisfied student, having achieved so much from this thesis and every other project I embarked on, only because of the support and assistance you provided me.

N.R. Thakrar
Den Haag, November 2020

List of Figures

1.1	Dornier droop nose morphing concept [12] which served as the basis of the design by Kintscher et al. [33]	2
1.2	Droop nose morphing demonstrator used in experimental evaluation by Sodja et al. [46]	2
1.3	Trailing Edge (TE) camber morphing concept featuring a gap sealed by a corrugation, shown in different morphed conditions [45]	2
1.4	TE camber morphing concept featuring a corrugated flexible skin [39]	2
1.5	FlexSys FlexFoil™ morphing technology patent shown in the undeformed (1.5a) and deformed (1.5b) conditions at the TE	3
1.6	An overview and presentation of the operation of the FishBAC concept [54]	3
1.7	lattice based, structural adaptive module designs	4
1.8	Piezo-electric skin actuation concept design by Bilgen and Friswell [19]	4
1.9	Deformed camber morphing wing employing Macro-fibre Composite (MFC) skin actuation [44]	4
1.10	Overview of TRanslation Induced Camber morphing (TRIC) concept employed to enable camber and twist morphing on the Combined morphing Assessment software using flight Envelope data and mission based morphing prototype wing development (CHANGE) wing [47]	5
1.11	Distributed morphing wing concepts found in literature	6
1.12	Distributed morphing concepts built by FlexSys [2]	6
2.1	Simplified representation of the TRIC concept	11
2.2	Critical features to be included in the design to achieve TRIC morphing	11
2.3	Actuators placed in the leading and trailing edge volume for the CHANGE project [47] . .	12
2.4	Kinematic system for actuating free edge	12
2.5	Linkage force as a function of rotation	13
2.6	DA22 and DA26 series actuator representations shown enveloped by the wing box . . .	13
2.7	Response time vs load capacity of VOLZ servo range [11]	13
2.8	Sensor and componentry layout in Smart-X wing	14
2.9	wing mounting design inspiration, with wing standing upright on the left, and a close up of the mounting boss (red) bonded to the wing shown on the right	14

2.10 Envisioned moulding and production process of the Smart-X wing	15
2.11 Mould design to support production of discontinuous lower wing	15
2.12 Smart-X Alpha wing concept with six independent modules trailing edge morphing modules seamlessly connected with a flexible material (red)	16
3.1 Free Body Diagram (FBD) representation of the aerodynamic load evaluation for the CHANGE wing [47]	18
3.2 Static aeroelastic simulation iteration loop in the work of Molinari et al. [38]	18
3.3 Fluid Structure Interaction (FSI) evaluation algorithm employed by Previtali et al. [45]	18
3.4 FSI analysis iteration loop utilized by Bilgen et al. [20]	19
3.5 Cantilever beam analysis model built in PATRAN	22
3.6 An example Bulk Data File (BDF) of a cantilevered beam	22
3.7 An example of a results file showing nodal deformations and elemental stresses for a cantilevered beam	23
3.8 XFOIL user interface to evaluate pressure distributions across an airfoil	24
3.9 Aeroelastic analysis method overview	25
3.10 Visualization of the boundary conditions applied in the structural analysis model	27
3.11 Resolution of structural mesh employed for aeroelastic analysis	27
3.12 Airfoil extraction process carried out with slicing of structural mesh	29
3.13 Influence of airfoil definition coordinate resolution on aerodynamic analysis	30
3.14 Resolution of aerodynamic mesh employed in aeroelastic analysis	30
3.15 C_L evaluated on a baseline airfoil with viscous and inviscid flow models for varying α	31
3.16 Simplified visualization of strip modelling method employed	31
3.17 Interpolation method to sample $c_{p\ fem}$	32
3.18 Aeroelastic analysis convergence assessment for models with varying levels of flexibility	33
3.19 Variation in C_L from changing panelling parameters in XFOIL	34
3.20 Structural mesh convergence study	34
3.21 Linear and non-linear analysis comparison	35
3.22 Representation of the distinction between analysis and design models [40]	36
3.23 Simplified interaction between numerical optimizer working with the design model and the Finite Element Methods (FEM) model [40]	37
3.24 Detailed interaction between numerical optimizer working with the design model and the FEM model [40]	37
3.25 Aeroelastic optimization framework	38

3.26 Design constraints employed in the optimization model	39
3.27 Discrete design regions enforced in optimization analyses	40
3.28 Two-dimensional (2D) representation of deformed wing shape for bend up configuration from stand alone analysis of trial 2	41
3.29 2D representation of deformed wing for bend up/down configuration with no curvature constraints	42
3.30 Method to enforce target shape on wing surface shown for the bend up subcase	42
3.31 Laminate ply distribution on morphing trailing surface	43
3.32 Morphing deformations for all subcases	44
3.33 Simulation results with lip integrated into model	44
3.34 Simulation results with lip integrated into model and added thickness	44
3.35 Laminate ply distribution on morphing trailing surface with offset lip	45
3.36 Morphing deformations for all subcases with lip integrated	45
3.37 Translation required at the free edge to achieve full morphing range	46
3.38 VOLZ servo product range, usable servos	46
3.39 Wingbox and leading edge analysis	47
3.40 Wingbox and leading edge analysis results	47
4.1 Chordwise arrangement of all mounting components for the actuation system	50
4.2 Kinematic relationship between actuator position and chordwise translation of sliding surface	50
4.3 Sullivan 3mm aluminium ball connectors	51
4.4 Analysis results from fork simulation, presented at 5x deformation	52
5.1 Graphical representation of actuation in the analysis model	58
5.2 Tip deflections (<i>mm</i>) achieved with discontinuous modules	58
5.3 Patterned silicone elastomer system trialled in first analysis	59
5.4 Tip deflections [<i>mm</i>] achieved with first elastomer system concept	59
5.5 Elastomer system trialled in the second concept, with increase in volume of silicone	60
5.6 Tip deflections (<i>mm</i>) achieved with second elastomer system concept	60
5.7 Elastomer system implemented in final concept, with the bridge completely filled with silicone	61
5.8 Tip deflections (<i>mm</i>) achieved with second elastomer system concept	61
5.9 Printable test rig assembly to test different elastomer connection methods	62

5.10	Test sample which thin silicone joints trialled to achieve continuity	63
5.11	Second design prototype, with a 15mm wide shear area provided on the bottom surface terminating to a 3mm tip on the top surface	63
5.12	Bulging effect seen on the second prototype during anti-symmetric actuation	64
5.13	Third design prototype, featuring a 30mm wide silicone connection on the bottom surface, terminating to a 10mm wide tip on the top surface	64
5.14	Bulging effect still prominent on the third concept, however to a lesser effect	64
5.15	Peak anti-symmetric tip deflections captured on the final prototype	65
5.16	Preparations of wing skin to be able to connect adjacent modules with silicone	65
5.17	Application of the silicone on top wing surface through the underside of the wing	66
5.18	Elastomer system cured on final wing shown for the connection between two wing modules	66
6.1	Influence of free-stream velocity on ΔC_L	68
6.2	Influence of α on ΔC_L	69
6.3	Influence of actuation inputs on ΔC_L	70
6.4	Single module surrogate model presenting a lift increment (ΔC_L) relative to baseline for given actuation inputs and angles-of-attack	70
7.1	Digital Image Correlation (DIC) test setup to measure deformations on bottom wing surface	71
7.2	Areas measured on the top and bottom surfaces in DIC testing	72
7.3	Rudimentary test setup to measure trailing edge tip deflections with a Vernier scale height gauge	73
7.4	Comparison of results between DIC measurements and calliper measurements	73
7.5	Comparison of baseline measured surfaces with baseline NACA 6510 airfoil to judge for repeatability	75
7.6	Comparison of out-of-plane deflections measured on top and bottom surfaces between trials for peak bend up, bend down tests	76
7.7	Baseline measurements carried out before starting the first bend up test shown in comparison to the ideal NACA 6510 airfoil shape	77
7.8	Comparison in tip deflections measured and simulated	78
7.9	Out-of-plane deflections compared between simulated and measured conditions for the peak bend up actuation of 25°	78
7.10	Chordwise deflections compared between simulated and measured conditions for the peak bend up actuation of 25°	79
7.11	Pivoting effect witnessed under actuation, shown in the elastomer test setup during a camber morphing configuration	79

7.12 comparison of measured surfaces with reduced simulation actuation inputs	80
7.13 Comparison in 2D deformations between measured and simulated conditions for matching trailing edge tip deflections	80
7.14 Influence of silicone on measured trailing edge tip deflections	81
7.15 Out-of-plane defections compared for peak bending cases with and without silicone shearing on the top surface	82
7.16 Out-of-plane defections compared for the peak bend up case with/without silicone shearing on the bottom surface	82
C.1 Baseline measured surfaces compared to the ideal NACA6510 airfoil, bottom surface .	104
C.2 Baseline measured surfaces compared to the ideal NACA6510 airfoil, top surface	105
C.3 Out-of-plane measurements on bottom surface for all tests at 5° actuation	106
C.4 Out-of-plane measurements on top surface surface for all tests at 5° actuation	107
C.5 Out-of-plane measurements on bottom surface for all tests at 10° actuation	108
C.6 Out-of-plane measurements on top surface surface for all tests at 10° actuation	109
C.7 Out-of-plane measurements on bottom surface for all tests at 15° actuation	110
C.8 Out-of-plane measurements on top surface surface for all tests at 15° actuation	111
C.9 Out-of-plane measurements on bottom surface for all tests at 20° actuation	112
C.10 Out-of-plane measurements on top surface surface for all tests at 20° actuation	113
C.11 Out-of-plane measurements on bottom surface for all tests at 25° actuation	114
C.12 Out-of-plane measurements on top surface surface for all tests at 25° actuation	115
C.13 Chordwise translation measurements on bottom surface for all tests at 5° actuation . . .	116
C.14 Chordwise translation measurements on top surface surface for all tests at 5° actuation	117
C.15 Chordwise translation measurements on bottom surface for all tests at 10° actuation . .	118
C.16 Chordwise translation measurements on top surface surface for all tests at 10° actuation	119
C.17 Chordwise translation measurements on bottom surface for all tests at 15° actuation . .	120
C.18 Chordwise translation measurements on top surface surface for all tests at 15° actuation	121
C.19 Chordwise translation measurements on bottom surface for all tests at 20° actuation . .	122
C.20 Chordwise translation measurements on top surface surface for all tests at 20° actuation	123
C.21 Chordwise translation measurements on bottom surface for all tests at 25° actuation . .	124
C.22 Chordwise translation measurements on top surface surface for all tests at 25° actuation	125

List of Tables

2.1	Summary of the design parameters and functional requirements to be satisfied by the Smart-X structural design	10
2.2	Analysis conditions for design subcases	11
3.1	Material properties	28
3.2	Thickness specification	28
3.3	Comparison in lift with linear and non-linear structural models	35
3.4	Tip deflection constraints for various subcases	39
3.5	Material properties used for optimization analyses	40
3.6	Actuation forces and nodal translations for each subcases	43
5.1	Wacker Elastosil Silicone Properties [10]	57
5.2	Summary of actuator travel and loads measured in simulating different elastomer connection concepts	61
A.1	VOLZ SERVOS Performance Specifications [11]	87

List of Abbreviations

- 2D** Two-dimensional. xi, xiii, 18, 19, 20, 24, 27, 29, 30, 31, 41, 42, 49, 75, 79, 80
- 3D** Three-dimensional. 21, 24, 25, 27, 30, 50, 83, 86
- ACARE** Advisory Council for Aeronautics Research in Europe. 1
- BDF** Bulk Data File. x, 22, 23, 25, 27, 28, 32, 69
- CFD** Computational Fluid Dynamics. 21
- CFRP** Carbon-fibre reinforced plastic. 5, 17
- CHANGE** Combined morphing Assessment software using flight Envelope data and mission based morphing prototype wing development. ix, 5, 9, 10, 12, 17
- DIC** Digital Image Correlation. xii, xxiii, 71, 72, 73, 74, 75, 77, 79, 81, 85
- ELLT** Non-linear Extended Lifting Line Theory. 19, 21, 83
- EMC** Elastomeric Matrix Composite. 3, 56, 84
- FBD** Free Body Diagram. x, 17, 18
- FEM** Finite Element Methods. x, xxii, 18, 19, 20, 25, 27, 31, 36, 37, 51, 86
- FSI** Fluid Structure Interaction. x, 18, 19, 20, 25, 35, 38, 41, 42, 85
- GUI** Graphical User Interface. 22, 23, 28
- LE** Leading Edge. 9, 10, 24, 34
- MFC** Macro-fibre Composite. ix, 4, 19
- OJF** TU Delft Open Jet Facility. xxi, xxii, 1, 6, 10, 14, 16, 51, 86
- SMA** Shape Memory Alloys. 2
- TE** Trailing Edge. ix, 2, 3, 9, 10, 24, 34, 42
- TRIC** TRanslation Induced Camber morphing. ix, xxi, 5, 9, 11, 15, 16, 25, 27, 51, 63, 84, 85
- TRL** Technology Readiness Level. 4
- UAV** Unmanned Aerial Vehicle. 5, 9
- VCCTEF** Variable Camber Continuous Trailing Edge Flap. 5

List of Symbols

C_L Lift coefficient [-]. x, xxiii, 10, 19, 30, 31, 33, 34, 35, 47, 68, 69

$C_{\mathcal{L}}$ Rolling moment coefficient [-]. 18

F_{act} Actuator force [N]. 12

$F_{linkage}$ Linkage force [N]. 12

L/D Lift-to-Drag Ratio [-]. 2, 9, 83

S Shore A Hardness. 57

V_{∞} Air speed [m/s]. 67

α Angle-of-attack [$^{\circ}$]. x, 10, 11, 24, 30, 31, 35

θ_{act} Actuator rotation [$^{\circ}$]. 12, 46

$\theta_{linkage}$ Included angle between F_{act} and $F_{linkage}$ [$^{\circ}$]. 12

r_{act} Torque arm length [m]. 12

$c_{p_{fem}}$ Pressure coefficient mapping on structural mesh. x, 32

Contents

List of Figures	ix
List of Tables	xv
List of Abbreviations	xvii
List of Symbols	xix
1 Introduction	1
2 Design Objectives and Concept Development	9
2.1 Design Goals and Functional Requirements	9
2.2 Design constraints	11
2.2.1 Integration of TRIC	11
2.2.2 Actuation system	12
2.2.3 Integration of sensors and bi-morphs	14
2.2.4 OJF mounting.	14
2.2.5 Manufacturability	15
2.3 Concept Overview	16
3 Wing Laminate and Actuation design	17
3.1 Review in Literature	17
3.1.1 Aeroelastic design and optimization frameworks	18
3.1.2 Structural solvers	20
3.1.3 Aerodynamic solvers	20
3.1.4 Summary of review	21
3.1.5 Selected software environments.	22
3.2 Linear Inviscid Aeroelastic Analysis	25
3.2.1 Model approach	25
3.2.2 Simplifications and assumptions.	25

3.2.3	Development of the FEM model	27
3.2.4	Development of the aerodynamic model	29
3.2.5	Fluid-structure coupling	31
3.2.6	System verification	33
3.3	Non-Linear Inviscid Aeroelastic Analysis Framework.	35
3.4	Aeroelastic Optimization Framework	36
3.4.1	NASTRAN SOL200 overview	36
3.4.2	Integration of SOL200	38
3.4.3	Design model.	39
3.4.4	Analysis model	40
3.4.5	Optimization approaches.	40
3.5	Design Results	43
3.5.1	Morphing surface laminate specification	43
3.5.2	Actuation design	46
3.5.3	Wing box and leading-edge laminate specification	46
4	Detailed Design for Manufacture	49
4.1	Design and Placement of Actuation System	49
4.2	Design of Sliding Surface Support.	51
4.3	OJF Mounting Design and Integration.	51
4.4	Sensor Cable Routing	52
5	Seamless Continuity Design and Integration	55
5.1	Functional Requirements.	55
5.2	Material Investigation.	56
5.3	Conceptual Design and Analysis	57
5.3.1	Analysis model overview	57
5.3.2	Prototype testing	62
5.3.3	Integration.	65
6	Surrogate Model Development	67
6.1	Model Requirements	67
6.2	Model Simplifications and Assumptions.	67

6.3	Surrogate Model Assembly	68
6.3.1	Influence of free-stream velocity on C_L	68
6.3.2	Influence of angle-of-attack on C_L	68
6.3.3	Influence of actuator inputs on C_L	69
6.3.4	Full model assembly	69
7	Analysis validation	71
7.1	Structural Testing with DIC.	71
7.2	Calibration of Results.	72
7.3	Results and Discussions of DIC Testing.	74
7.3.1	Assessment of repeatability	74
7.3.2	Evaluation of baseline shape	75
7.3.3	Evaluation of camber morphing	77
7.3.4	Evaluation of camber morphing with the influence of silicone	81
8	Recommendations	83
9	Conclusions	85
A	VOLZ SERVOS Performance Specifications	87
B	Technical Drawings	89
C	DIC Testing Results	103
C.1	Baseline Measurements	104
C.2	Out-of-plane Deflection Measurements	106
C.3	Chordwise Deflection Measurements	116
	Bibliography	127

1

Introduction

Air travel continues to be one of the most popular modes of transport, with traffic set to continually increase in the coming years [16]. As beneficial as it is to unlock the possibility of flight to a larger population, considerations need to be made which ensure the volume of harmful emissions being entered into the environment is sustainable. With this foresight, various targets have been set by the Advisory Council for Aeronautics Research in Europe (ACARE) to promote research of technologies targetting improved efficiencies in flight. They have set aims to reduce carbon dioxide emissions by 75% and nitrous oxide emissions by 90% by the year 2050. Achieving these targets will take more than just optimizing the classical aircraft design which now has diminishing returns [28].

When evaluating the typical flight profile of a commercial aircraft (take-off → manoeuvring → cruising → landing), each stage has different system performance requirements. For example, lift-off prioritizes high lift conditions to ensure the aircraft can soar into the sky at lower speeds and reduced runway lengths. This requirement is different to cruise, where importance is placed towards drag-minimization and supporting occasional gust loads. The classical approach to address these varying requirements is to design the base aircraft shape to be best optimized for the most prominent part of the flight profile and use morphing mechanisms such as flaps, slats and ailerons to adapt the shape of the wing as best as it can for the other operating points. At it's first introduction, control surfaces such as these opened up a new generation of aircraft offering high flight efficiencies. However, now the improvements which can be offered by them are tapering. A large part of this plateauing effect is as a result of discrete rigid mechanisms still being able only to offer a discrete number of possibilities on shaping the global wingspan. They additionally come with drag penalties which are brought about by the discontinuous assemblies allowing them to exist. The outcome is an aircraft wing which is a compromise of several sub-optimal shapes, synonymous to the saying "jack off all trades, master of none."

This realization has been present throughout history, with designers always hoping to open up the possibilities of how the shape of the wing can be changed more seamlessly, however achieving such traits was limited with the knowledge and technologies of the time. This characteristic is best understood by realizing a continuous twist morphing wing was implemented on the Wright Brother's aircraft, made possible through wing flexibility [31]. The ability to achieve such flexible wings declined with increasing aircraft speeds promoting rigid wing designs to overcome aeroelastic instabilities which started occurring. However, now with such an improved understanding of structures and aerodynamic theory, combined with advancements in aerospace materials, manufacturing technologies, hardware and control systems, increasingly flexible structures are now becoming more feasible to design, test and build.

The TU Delft Faculty of Aerospace Engineering sees the promise of enhancing what can be achieved with morphing wing implementations on aircraft and put forth an investment to develop and manufacture a morphing wing concept which can be tested at the OJF Wind Tunnel. Designated the project

name Smart-X, this interdisciplinary project was established to integrate smart sensors and smart control to build a smart morphing wing structure which develops on the current state-of-art morphing technologies. The objective of this thesis has been to develop, design and manufacture a morphing wing demonstrator which could be tested.

Rather than reinventing the wheel, an investigation into current wing designs shows that commercial airliners choose to morph airfoil shape across the span with flaps and slats. Actuating these control surfaces result in local wing camber changes, and the benefit of introducing several of these across the span allows the wing to take on an apparent twisted shape. Such levels of morphing allow the ability to modify lift profiles, alleviate gust and manoeuvre loads, increase the L/D ratio and suppress flutter. Planform shape changes such as sweep and span, on the other hand, are rarely seen, amounting to the fact that heavy mechanisms are often needed to make them achievable, which often counteracts any performance benefits offered from the aerodynamic improvements [18]. Therefore, it is not a surprise that the majority of the literature focuses on improving camber morphing capabilities of an airfoil and inducing wing twist.

Camber morphing capabilities have been achieved through conventional actuators and systems, as well as with the use of novel smart materials such as Shape Memory Alloys (SMA) and piezoelectrics. A seamless droop nose concept was investigated by Kintscher et al. [33], to overcome limitations from slat designs compromising laminar flows over an airfoil. It developed on the Dornier patent of a smart droop nose device shown in Fig. 1.1. The patent features a closed skin with no discontinuities, which in the work of Kintscher et al. [33] was constructed from glass fibre. Skin strains were kept low by maintaining the length of the leading edge.

This concept evolved with the work of Sodja et al. [46], who were able to design an improved kinematic system which increased shape control authority and provided an improved method of locking the nose into a given shape for enhanced aerodynamic load transfer to the wing box structure. In their work, the skin was constructed from aluminium. The manufactured system shown in Fig. 1.2 shows the complex kinematic system which needed to be implemented to be able to provide these morphing capabilities.

Compliant skin designs have been implemented for some concepts to reduce actuation forces. Various means have been trialled to allow the stretching of the external wing skin. Previtali et al. [45] used an opening sealed with a flexible corrugation on the bottom surface (Fig. 1.3). Molinari et al. [39] utilised a corrugated external skin which could stretch or compress with a compliant rib structure (Fig. 1.4). In their designs, the internal volume was heavily occupied compliant ribs, reducing space availabilities for other components and wirings which generally need to be integrated into wings.

FlexSys' FlexFoil™ technology has become one of the more

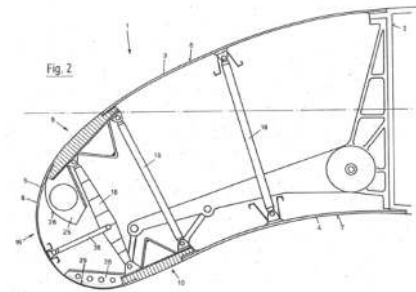


Figure 1.1: Dornier droop nose morphing concept [12] which served as the basis of the design by Kintscher et al. [33]



Figure 1.2: Droop nose morphing demonstrator used in experimental evaluation by Sodja et al. [46]

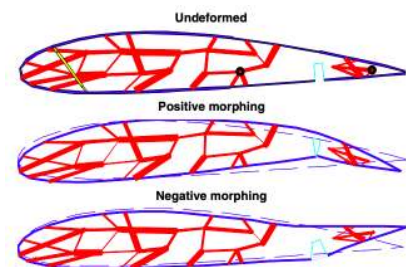


Figure 1.3: TE camber morphing concept featuring a gap sealed by a corrugation, shown in different morphed conditions [45]

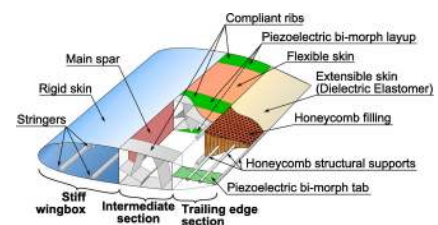


Figure 1.4: TE camber morphing concept featuring a corrugated flexible skin [39]

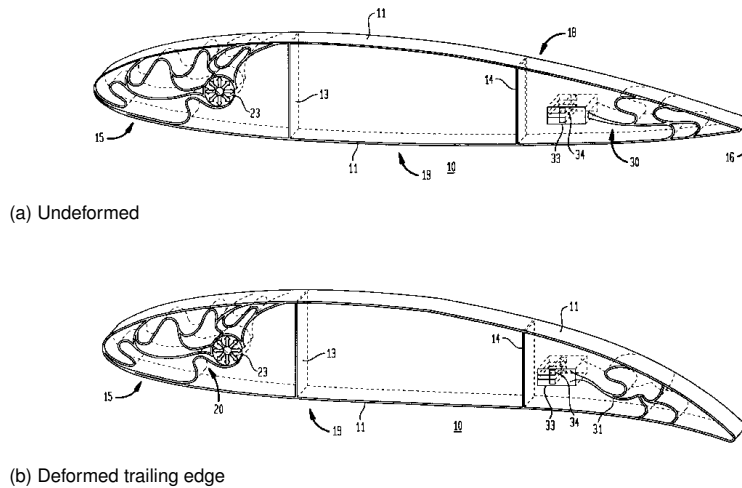


Figure 1.5: FlexSys FlexFoil™ morphing technology patent shown in the undeformed (1.5a) and deformed (1.5b) conditions at the TE

technologically advanced leading/trailing edge morphing technologies, being flight tested on the Gulfstream [34, 35]. The tested wing was built on the principles of the patented design shown in Fig. 1.5. It features a folded compliant internal rib structure which is actuated linearly (trailing edge) or rotationally (leading edge). The external skin can be constructed from aluminium, magnesium alloys or polymer matrix composites to comply with the desired morphing shapes. This design is one of the most developed, but the intricate folds in the substructure increase analysis and manufacturing difficulties.

The FishBAC concept [52–54] which took inspiration from the biological world, was designed to mimic the skeletal frame of a fish. Fig. 1.6 shows the design which enabled camber morphing to be possible with the use of a series of stringers to carry the pressure load applied on a flexible Elastomeric Matrix Composite (EMC) skin wrapped around the structure. The skin itself was pre-tensioned so that it did not buckle when it experienced compressive motion. Actuation was made possible through an antagonistic tendon drive system. Two tendons were mounted symmetric about the spine and attached rigidly to the trailing edge. These connected to the spooling pulley drive, which when actuated created bending moments at the trailing edge, effectively causing airfoil camber changes.

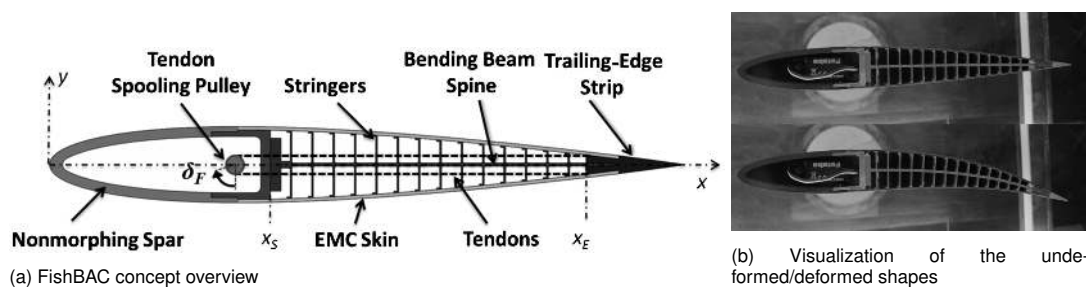


Figure 1.6: An overview and presentation of the operation of the FishBAC concept [54]

Recently, the use of ultralight, lattice based, structural adaptive modules have been investigated. With their stiffness comparable to that of an elastomer, and a mass-density typical to aerogel, their morphing capabilities are high. Cramer et al. [23] demonstrated improved aerodynamic efficiency and roll control authority with spatially programmed elastic morphing shape of a 4m wingspan in the wind tunnel (Fig. 1.7a). Jenett et al. [30] showed a digital morphing concept constructed from discrete lattice elements which utilized a spanwise twisting deformation to show increased roll efficiency (Fig. 1.7b). These concepts targeted structural efficiencies with aerodynamic efficiencies; however, the structure itself was rather complex to implement. They feature many components and occupy the majority of the internal volume, which prevents the storage of other aircraft systems.



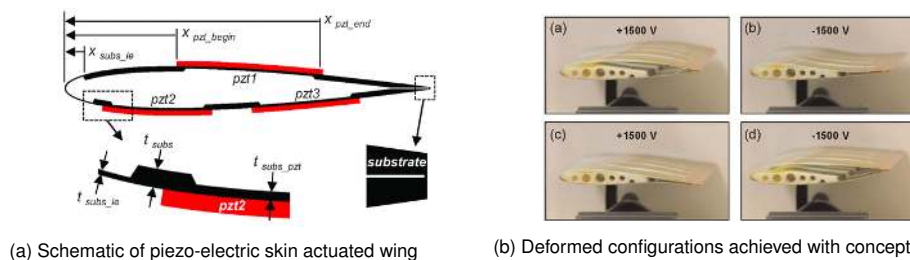
(a) MADCAT morphing wing which was built from assembly of many small building blocks [23]



(b) Digital morphing wing concept with a lattice based structure [14]

Figure 1.7: lattice based, structural adaptive module designs

Rather than using internal actuation mechanisms, some studies have been conducted using direct skin actuation by using piezo-electric [19, 21] and MFC actuators [44] for camber morphing. Fig. 1.8 shows the skin actuation using distributed piezo-electrics across the airfoil to achieve variable camber changes across the airfoils. Fig. 1.9 shows a similar concept which features MFCs on the trailing edge to induce camber morphing.



(a) Schematic of piezo-electric skin actuated wing

(b) Deformed configurations achieved with concept

Figure 1.8: Piezo-electric skin actuation concept design by Bilgen and Friswell [19]

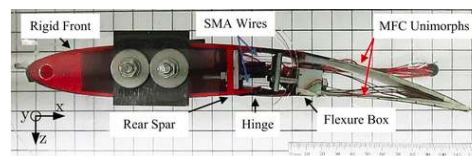


Figure 1.9: Deformed camber morphing wing employing MFC skin actuation [44]

It was evident in literature that wings integrating camber/twist morphing were complex to design, build or integrate with current aircraft systems. As such, their widespread uptake in the aviation industry is still limited. This integration is further hindered by lack of wind tunnel and flight tests on such systems to iron out all limitations of morphing designs, keeping their Technology Readiness Level (TRL) low [18].

Research to come out of TU Delft has already overcome the difficulties mentioned above of morphing technologies. The establishment of the EU FP7 CHANGE project to develop a flight-worthy Unmanned Aerial Vehicle (UAV) with multiple morphing technologies promoted the development of the TRIC concept by Werter et al. [51]. With the use of conventional actuators in paring with a wing constructed from the simple lamination of Carbon-fibre reinforced plastic (CFRP), the concept allowed for sufficient shape control of wing camber and twist to alter aerodynamic performance. The operating principle of the system was simple, straight cuts along the length of the span were introduced on the bottom skin, fore and aft of the wing box. Now free, translation of this edge induced shape changes at the leading and trailing edge through skin bending and warping. To be able to control the shape, a pair of servo actuators were placed at the root and tip of the morphing portion of the wing, at the leading and trailing edge. These actuators were connected with linkages to the now-restrained edge. Symmetric or asymmetric loading resulted in camber or twist morphing, respectively. Wind tunnel tests showed the promise of being able to integrate this concept to provide aerodynamic gains; however, it showed limited ability in providing twist across the span, restricted to a linear twist distribution. The workings of this concept are shown in Fig. 1.10.

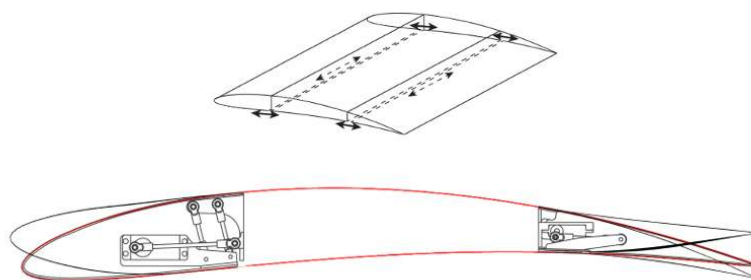


Figure 1.10: Overview of TRIC concept employed to enable camber and twist morphing on the CHANGE wing [47]

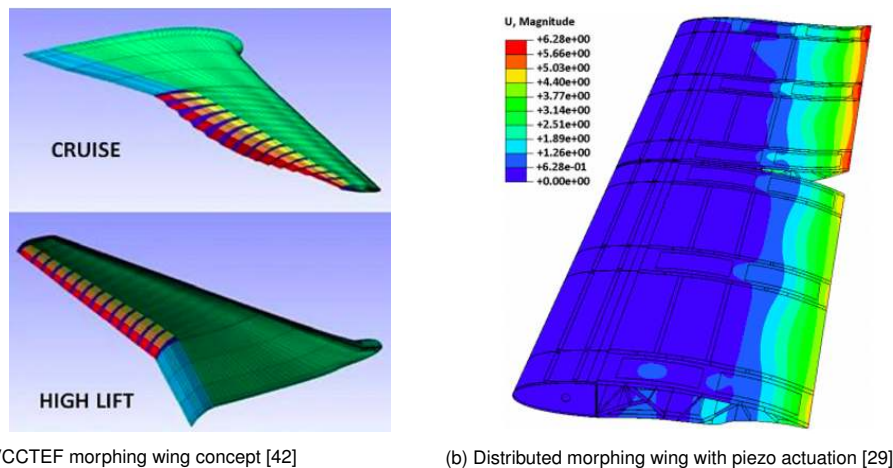
Over actuated distributed morphing concepts enabling increased authority over wing twist are rarely found in the literature. Most have shown limited morphing capacity by only being able to control the shape of the entire wingspan with a minimum set of actuators. The NASA Variable Camber Continuous Trailing Edge Flap (VCCTEF) proposed the continuous distributed morphing wing concept [42] shown in Fig. 1.11a. In wind tunnel tests, they were able to show such a system could achieve higher lift coefficients, with reduced drag as a comparison to conventional flaps. However, the design was manufactured with a complex sub-structure [37].

Building on the optimization work of [39], Henry et al. [29] optimized a distributed morphing wing to increase the rolling moment and improve flutter characteristics. Their design proposed a modulated version of the compliant skin concept shown in Fig. 1.4 to achieve distributed morphing. This concept is shown in Fig. 1.11b. The concept did not provide a means to achieve a seamless skin transition between adjacent modules resulting in a drag penalty.

FlexSys were able to integrate their FlexFoil™ technology in a distributed morphing wing, depicted in Fig. 1.12a. They were also able to introduce fairings constructed from a distributed compliant structure using a combination of rigid and flexible elements to achieve the seamless spanwise transition, as shown in Fig. 1.12b.

It was evident that on the rare occasions distributed morphing has been trialled, difficulties from the manufacturing and practicalities side are still present. Where attempts to build or test distributed morphing have been investigated, designers opted to determine ways to introduce a seamless transition between independent control surfaces to overcome the otherwise existing drag penalties. Therefore, as much as these systems offer benefits in achieving simultaneous load alleviation and drag minimization capabilities, all have been realized with elaborate designs.

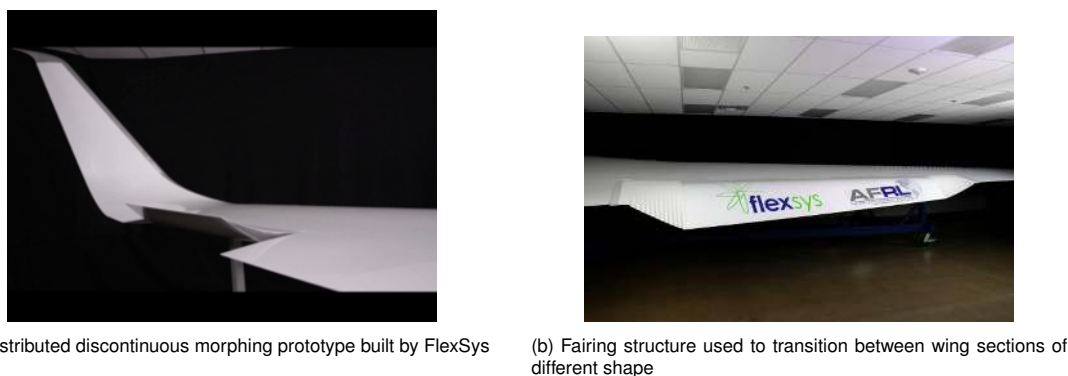
The objective of this thesis was to extend the TRIC concept in a modular fashion to produce a distributed over-actuated morphing wing that can advance the functionalities of morphing wings without



(a) VCCTEF morphing wing concept [42]

(b) Distributed morphing wing with piezo actuation [29]

Figure 1.11: Distributed morphing wing concepts found in literature



(a) Distributed discontinuous morphing prototype built by FlexSys

(b) Fairing structure used to transition between wing sections of different shape

Figure 1.12: Distributed morphing concepts built by FlexSys [2]

the use of too abstract concepts and materials. The project was established as an interdisciplinary venture that would integrate state-of-the-art smart piezo-electric and fibre optic sensors (developed by students of other departments) to feed into a smart control system. The control system would provide the autonomous functionality to optimize the wing shape to achieve simultaneous benefits in load alleviation, drag minimization and flutter suppression. Hypothesized benefits were to be validated in the OJF.

The supporting research question that was established to address this objective was:

How can the TRIC morphing concept be integrated into a manufacturable seamlessly distributed trailing edge morphing wing to achieve simultaneous load alleviation, flutter suppression and drag minimization capabilities?

The following sub-questions were formulated to direct the research appropriately:

- How are structural and actuator parameters defined to achieve desired morphing shapes in a given aerodynamic environment?
- How can the fluid-structure interaction of morphing wings be analyzed to be able to map aerodynamic performance outputs to actuator inputs?
- How can a seamless transition between individual modules be designed to achieve a seamless distributed morphing wing?

The work carried out in this thesis answers the questions listed above.

This thesis documents the design process which was carried out to be able to manufacture the wing (which came to be known as the Smart-X Alpha) and the steps that were taken to develop a surrogate model of the system to support the smart control of this wing. Within Chapter 2 the formulation of the conceptual design is discussed, which was based on several design goals, constraints and requirements. This work is followed by a presentation of the analysis framework which was built to support the design of the primary wing structure (wing skin and box) and evaluate actuation requirements in Chapter 3. Chapter 4 summarises the detailed design and analysis work carried out to be able to produce manufacturing and assembly drawings which are presented in the appendices. An extensive analysis and testing campaign was carried out to evaluate suitable elastomers which could be used to achieve wing continuity which is discussed in Chapter 5. Establishment of the surrogate model is discussed in Chapter 6. Results from several verification tests conducted are summarised in Chapter 7 to be able to make final recommendations and conclusions (Chapters 8 and 9).

2

Design Objectives and Concept Development

The Smart-X project was established to develop on the state-of-the-art morphing technologies through the design and production of a demonstrator integrating smart sensors and novel control methods to achieve simultaneous load alleviation, drag minimization and flutter suppression. To be able to realize these functionalities, the proposed design solution was to extend the TRIC concept in a modulated fashion to achieve distributed, over-actuated camber/twist morphing, with a seamless continuity between independent modules. The evolution of this initial idea into a manufacturable morphing wing concept is discussed in this chapter.

A structured design approach had to be undertaken to ensure that initial objectives could be met. With generic design goals known, the process started with establishing necessary functional requirements of the aerodynamics and structure which would allow these goals to be met. This evaluation was followed by an assessment of design constraints which needed to be considered. A concept could then be evaluated which would fit within these bounds.

2.1. Design Goals and Functional Requirements

As mentioned repeatedly, the following goals had to be achieved from the design:

- Be able to alleviate manoeuvre and gust loads
- Provide the ability to suppress flutter
- Morph the wing shape to optimize L/D

These were to be demonstrated on a wing and environment representative of a typical UAV application. As such, several design parameters were absorbed from the CHANGE project, where an aerodynamic study was completed to evaluate a suitable wing geometry and morphing range for the application. Therefore, the baseline wing shape was set as NACA 6510, with a wing chord fixed to $0.5m$, and a semi-span of $1.8m$. Distributed morphing capabilities would be provided by splitting the wing into six individual modules, which could feature some form of continuity integrated between them to overcome drag penalties. The spar placement would match that of the CHANGE project.

Generally speaking, achieving the three goals on a standard aircraft wing is resolved with variable TE deflections. Leading Edge (LE) deflections primarily benefits low-speed lift generation. In the

CHANGE project, however, LE morphing was still included to optimize the wing profile to the best available shapes. Simultaneous integration of the LE and TE morphing does result in greater freedoms in target shapes, but also increases the number of moving parts and reduces space availabilities with inclusions of many actuators. Given these limitations, preference was to focus morphing on the trailing edge for this application. Additional piezo-electric high-frequency bimorphs would be integrated on the trailing edge to provide flutter suppression capabilities. The design of these bimorphs was not in the scope of the thesis. Only their placement had to be considered.

An extensive aerodynamic assessment for target shapes was not deemed necessary for this project as it was focused towards proof-of-concept. Therefore deformation targets were adapted from the CHANGE project. For that wing, tip deflections at the trailing edge ranged from $-10mm$ to $25mm$ which were coupled with leading-edge deformations. The result was a peaking C_L of 1.52 [47]. The range of travel at the trailing edge tip for this particular wing was increased to $-20mm$ to $30mm$. Angle-of-attack limits were set from -12° to $+5^\circ$, which were considered the most adverse experienced by a typical UAV. With a rudimentary inviscid aerodynamic analysis in XFOIL, this provided a lift range (C_L) of -1.7 to $+2$, deemed more than sufficient to provide all required functionalities.

The wing structure had to sufficiently withstand loading at a maximum speed of $30m/s$ (limit at OJF), with an assumed air density of $1.225kg/m^3$, and consideration of additional gust loads.

A summary of the discussed design specifications and functional requirements to be satisfied by the structural design are clearly stated in Tab. 2.1

Table 2.1: Summary of the design parameters and functional requirements to be satisfied by the Smart-X structural design

Wing chord	$0.5m$
Wing semi-span	$1.8m$
No. of modules	6
Module span	$0.3m$
Trailing edge tip deflection range	$-20mm$ to $30mm$
Maximum wind speed	$30m/s$
Air density	$1.225kg/m^3$
Angle-of-attack range	-12° to $+5^\circ$

With the defined functional requirements, three limit states were established for design purposes. These paired maximum morphing limits on each wing module with the most adverse angles-of-attack and wind speeds to be able to account for the highest pressure loads they could experience.

The limit states were designated as design subcases, and considered peak bend up morphing, with $30mm$ translation of the trailing edge, peak bend down morphing, with $-20mm$ translation of the trailing edge, and peak twist morphing, where the trailing edge deformed diagonally with $-20mm$ deflection at one extreme, and $20mm$ deflection at the other extreme.

The aerodynamic environment for all subcases was set with a wind speed of $30m/s$ and air density of $1.225kg/m^3$. The α considered for each case varied to enforce the most adverse loadings on the structure, primarily for the bend up and down cases. When bent upwards, the airfoil camber is more positive and therefore experiences higher pressure loads with a negative α . For this reason, the peak bend up subcase was to be analyzed with an α of -12° . The contrary was correct for the bend down subcase and therefore was assigned an angle-of-attack of 5° . For twist morphing, the designated analysis α was maintained as 0° .

These design subcases are summarized in Tab. 2.2.

Table 2.2: Analysis conditions for design subcases

Subcase	TE Deflection [mm]	V_∞ [m/s]	α [°]
Bend up	30	30	-12
Bend down	-20	30	5
Twist	± 20	30	0

2.2. Design constraints

Several design constraints had to be considered in the design, which included implementing the TRIC morphing concept with a suitable actuation system whilst ensuring manufacturing feasibility. These constraints are discussed in the following subsections.

2.2.1. Integration of TRIC

A simplified representation of the TRIC concept is shown in Fig. 2.1. A longitudinal cut is introduced along the span of the wing section, adjacent to the wing box. Translation of this free edge introduces shape changes in the section through skin bending and cross-sectional warping. A pair of servo actuators which are kinematically linked to this free edge is placed at the extremities of the wing section. Camber or twist morphing is induced through symmetric or asymmetric actuation, respectively.

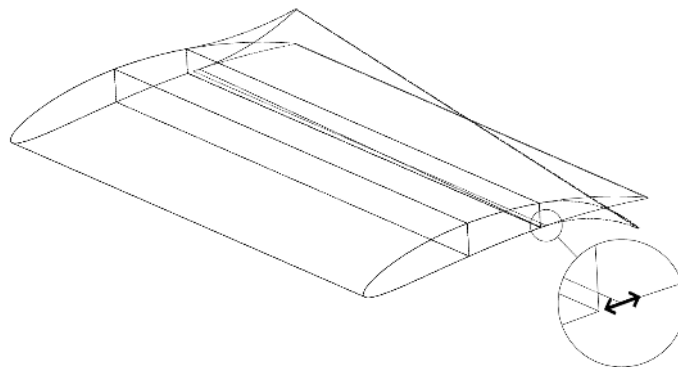


Figure 2.1: Simplified representation of the TRIC concept

Two additional elements need to be included structurally to allow this concept to function as intended. Firstly, when a cut is made, an opening to the wing structure is introduced, which produces a drag penalty. To overcome this, the free edge needs to be offset and rested on a rigid surface which overlaps the opening to close the gap. Secondly, shape changes are only introduced by the chordwise translation of the free edge; any out-of-plane deformations are not beneficial. Therefore, a supporting structure has to be placed directly above the free edge to ensure only the sliding degrees of freedoms are free. These additional details are highlighted in Fig. 2.2.



Figure 2.2: Critical features to be included in the design to achieve TRIC morphing

2.2.2. Actuation system

Several free volumes exist to envelope the actuators within the wing. In the CHANGE project, they were placed outside of the wing box, in the free volumes fore and aft of the front/rear spars, as shown in Fig. 2.3. This was a requirement for that project; however, this restricted the actuator size and necessitated the design of a complex mounting structure. For this experimental project, the capacity to use larger more powerful actuators was favourable; therefore it opted that actuators would be mounted in the wing box where more space is available, with a linkage connected to an attachment point on the free edge. Holes would be introduced in the rear spars to allow unrestricted travel of the linkages.



Figure 2.3: Actuators placed in the leading and trailing edge volume for the CHANGE project [47]

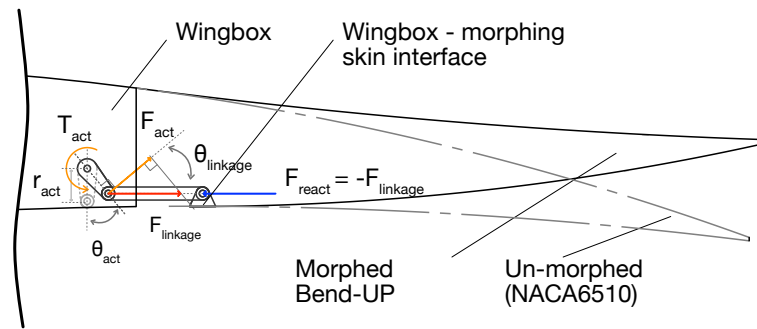


Figure 2.4: Kinematic system for actuating free edge

The resulting kinematic system would look similar to the representation shown in Fig. 2.4. The figure describes the free body forces of the actuation system in the bend up morphing case. From analyzing the system, it was realized that the immediate application of torque at the servo would result in non-linear force output in the direction of the linkage ($F_{linkage}$) with increasing actuator rotation (θ_{act}). The relationship between $F_{linkage}$ and θ_{act} is given below. The terms, F_{act} and $\theta_{linkage}$, represent the normal force output from the actuators and the angle between this normal direction and the axis of the linkage. As the linkage length will be much greater than the arm length, $\theta_{linkage}$ could be approximated as equivalent to θ_{act} .

$$F_{linkage} = \frac{F_{act}}{\cos(\theta_{linkage})} \approx \frac{F_{act}}{\cos(\theta_{act})}$$

The non-linear force output in the direction of the linkage (in relation to the actuator force) as a function of actuator position is shown in Fig. 2.5. To benefit controllability, it was beneficial to know that a linear torque output resulted in a linear force scaling, hence it was decided that the peak rotation range of the actuator shall be limited to $\pm 40^\circ$, where the ratio of $F_{linkage}$ to F_{act} is still ≈ 1 . This range would be defined by the necessary chordwise travel required at the free edge and length of the torque arm (r_{act}).

Beyond kinematic constraints, the capability to trial different servos had to be designed in the mounting system to serve future experimental purposes. Therefore, it was decided that the mounting of the servos would be done on a configurable structure which is attached to the inside of the top side of the wing. Access to the servos would be made possible with access hatches integrated on the less critical lower side of the wing.

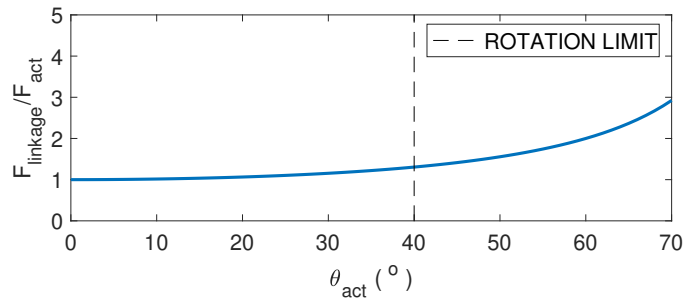


Figure 2.5: Linkage force as a function of rotation

Several different actuators could be used; however, it was a requirement that they could provide accurate position feedback to support the control of the wing. To satisfy the feedback criterion, the VOLZ SERVOS product range was investigated to find suitable actuators. Due to packaging constraints, the largest servos which could be packaged in the wingbox were the DA22 series. The DA26 series onwards were too large to fit comfortably within the wingbox, as shown in Fig. 2.6. The 10mm offset shown in the figure was included to consider a minimum thread depth required in the mounting structure to fix the servos rigidly.

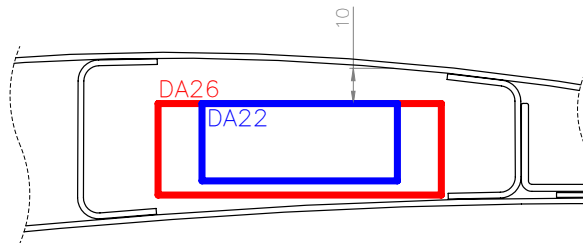


Figure 2.6: DA22 and DA26 series actuator representations shown enveloped by the wing box

Performance specifications of all servos up to the size of the DA22 series were evaluated to determine peak force outputs and response speeds. Peak forces were calculated by multiplying the peak continuous torque output achievable by the servo and the minimum torque arm offered (by the supplier) on that servo. The arm size varied from 7mm to 12.5mm depending on the size of the servo. A plot of the performance range is presented in Fig. 2.7. In it, the servos with peak response speeds and peak forces are highlighted. The peak force of 150N was offered by a DA22 series servo, whereas the much smaller DA13 servo offered a peak response speed of 520°/s. This range was beneficial in understanding upper force limits for optimization purposes and evaluating a suitable frequency for actuation. The database used to formulate the plot is presented in App. A.

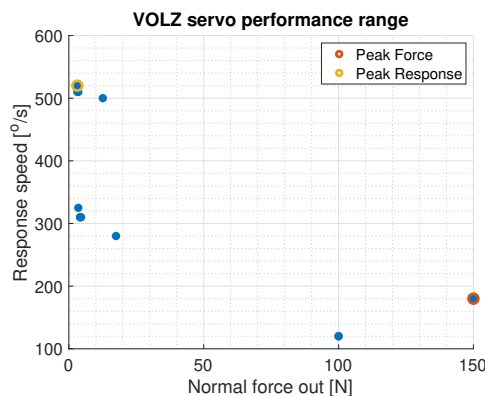


Figure 2.7: Response time vs load capacity of VOLZ servo range [11]

2.2.3. Integration of sensors and bi-morphs

This smart structure was to be controlled with inputs from state-of-the-art smart sensors evaluating the aerodynamic conditions and the shape of the wing. Placement of these sensors is shown in Fig. 2.8. Piezo-electric boundary layer transition sensors were to be placed across the top surface of the wing, exposed to the aerodynamic environment with drilled holes in the skin. Fibre-optic shape sensors were to be placed in each wing module on the upper and lower surfaces of the trailing morphing surface, with a pair of fibres aligned in the spanwise direction in central wing box, on the top and bottom sides. LED strips would be used in the vicinity of the optic shape sensors. Beyond aesthetics, these additional elements could support motion tracking of the wing for vibration analysis. The piezo-electric bimorphs would be assembled to the trailing edge of the wing to support flutter suppression. These did not span the entire trailing edge to ensure a continuous flexible surface could be integrated between modules.

No critical design constraints were imposed with the integration of these components; however, proper routing of all the cables (required to power and communicate with them) needed to be considered for manufacturing and assembly purposes.

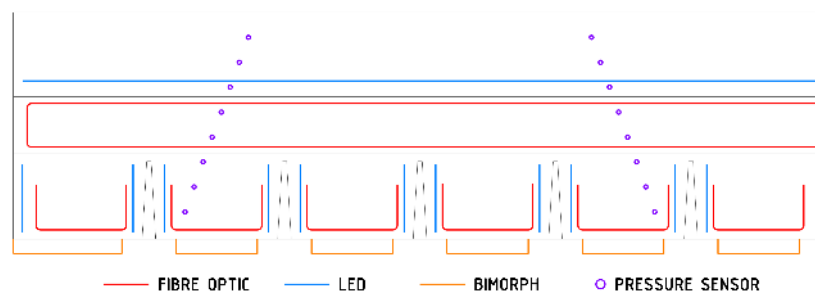


Figure 2.8: Sensor and componentry layout in Smart-X wing

2.2.4. OJF mounting

To be able to test the wing at the OJF, a mounting system had to be integrated within the design. Design inspiration was taken from another project shown in Fig. 2.9. It shows how a machined mounting boss (red) was bonded within the wing box of the test wing. This boss was clamped by a base which attached to the load cell in the wind tunnel.

Given that the clamping base was available for use, it was decided that only a new mounting boss needed to be designed and manufactured to fit within the new wing box shape. The remainder of the mounting system could be reused from the previous project.

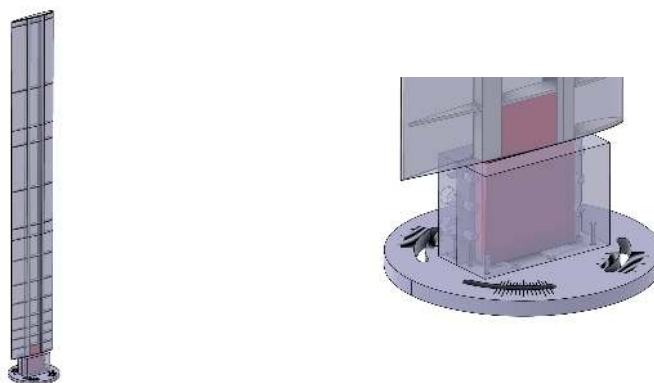


Figure 2.9: wing mounting design inspiration, with wing standing upright on the left, and a close up of the mounting boss (red) bonded to the wing shown on the right

2.2.5. Manufacturability

The manufacturing method was influential in constraining several design choices. A process of production was discussed with the lead wing manufacturer, Martin Weberschock, owner of Weberschock-Development. The considered process is presented in Fig. 2.10. It was decided that the wing would be constructed with the vacuum curing of wet-laid glass fibre. As a curing oven was not available, the use of pre-preg fibres was discarded. The wing would be constructed in two separate halves, top and bottom. Having the assembly open would allow the positioning and bonding of the internal sub-structure, sensors and other components. At completion, the wing could be closed by bonding the two halves together. Independent trailing edge morphing modules would be introduced by cutting the trailing edge surface and introducing the continuity system after the wing is released from the mould.

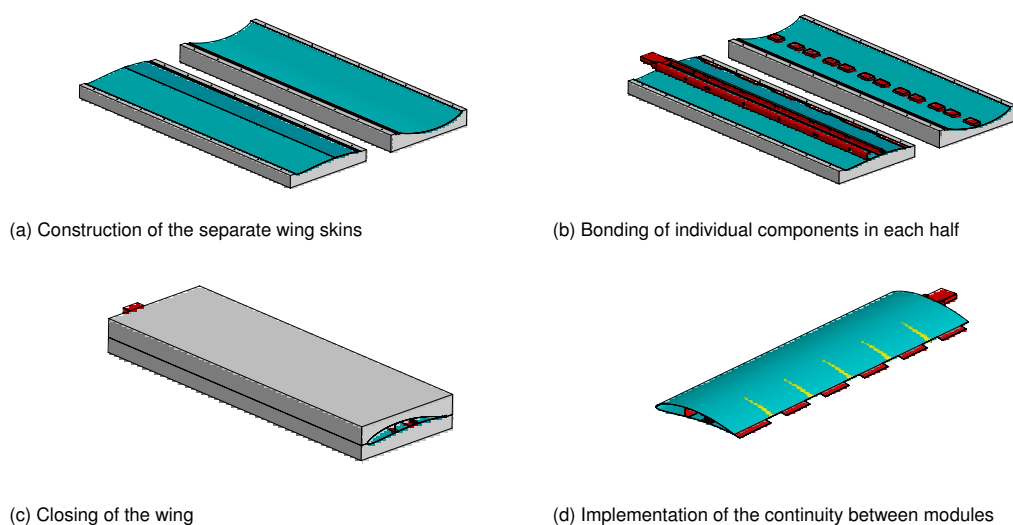


Figure 2.10: Envisioned moulding and production process of the Smart-X wing

The layup of the top half of the wing skin could be done in one curing step as the design is continuous with no breaks or terminations. This was not true of the bottom surface, where cover panels would need to be integrated, as well as the disconnected sliding interface. To ensure that the introduction of cover panels would not produce significant discontinuities in the wing surface, they would be laminated and cured first on the bottom skin mould. After this, a release coat could be applied on top to then laminate the rigid front portion of the bottom wing skin above the panels. Once cured, another release film could be applied on the overlapping region of the TRIC interface, to laminate the trailing morphing surface finally. The staggered approach to realize the sliding surface is shown in Fig. 2.11.

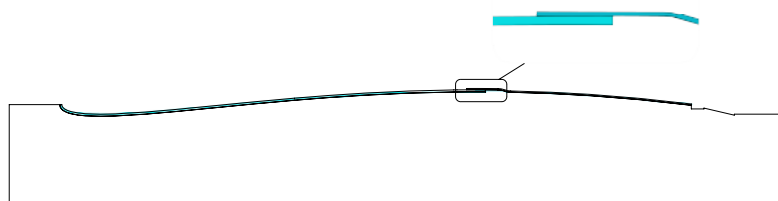


Figure 2.11: Mould design to support production of discontinuous lower wing

2.3. Concept Overview

The following concept of the Smart-X wing was developed to achieve the functional requirements within the given design constraints. In the figures, a seamlessly distributed morphing wing with six independent camber/twist morphing modules is shown. Morphing functionality was to be made possible with the TRIC concept, powered with VOLZ actuators placed in the wing box. The wing would feature a bonded mounting boss that can be clamped by a mounting structure which can be attached to the load cell in the OJF to stand upright.

The detailed design of each of the systems is discussed in the succeeding chapters, starting with developing an appropriate analysis framework to design the wing skin.

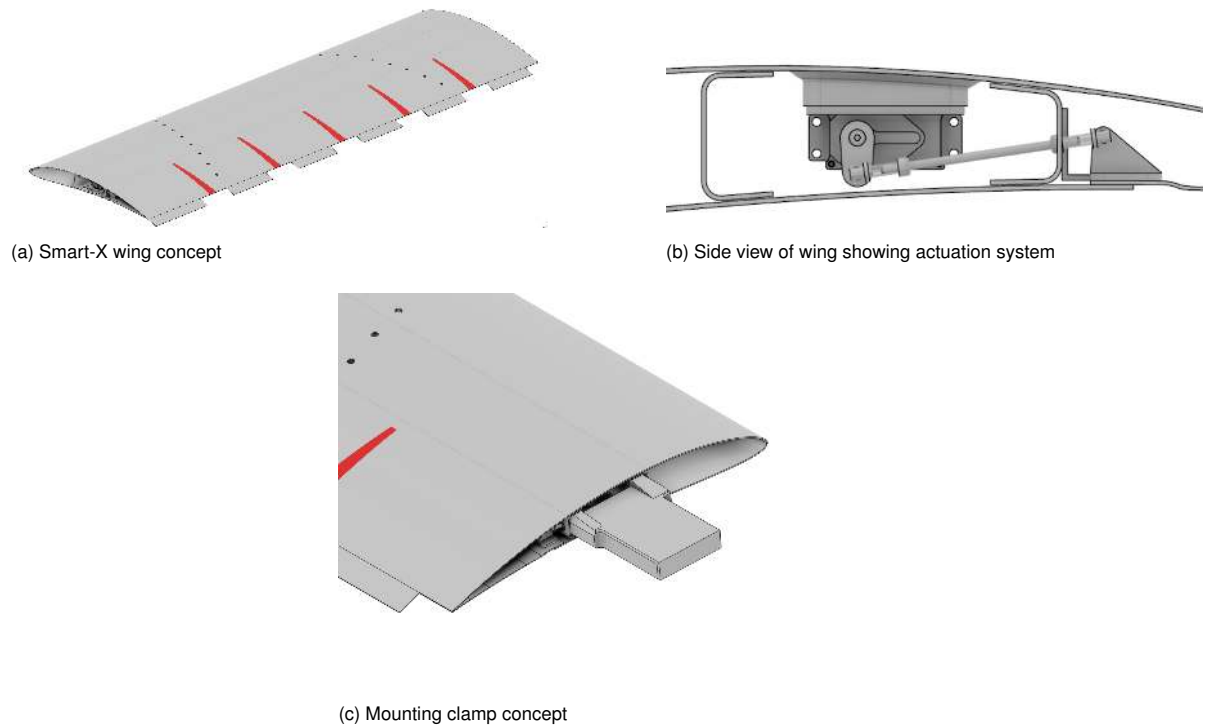


Figure 2.12: Smart-X Alpha wing concept with six independent modules trailing edge morphing modules seamlessly connected with a flexible material (red)

3

Wing Laminate and Actuation design

An effective method of design had to be established to specify the layup of the wing skin and wing box laminate as well as support the selection of actuators. The design of the continuous leading edge and wing box could be completed in a straightforward manner as it would be relatively rigid, and therefore aeroelastic interactions would not be prominent. This however would not be true for the morphing trailing surface: the deformed shape, and actuation loads, would be influenced by the layup and the surrounding airflow. Additionally, the continuous deformation could result in non-linear lift increments under actuation which would need to be considered for the control system and therefore the surrogate model.

To support the design process and develop the surrogate model, an aeroelastic analysis tool had to be built with the capacity to optimize the wing skin for reduced actuation loads and optimal aerodynamic shape. Methods of how such analyses could be carried out was sought out in literature to hone in on the most suitable method which could be implemented for this application. From this, the building and validation of the tool could be carried out to setup the basis for developing the wing skin laminate specification. This work formulates the contents of this chapter.

3.1. Review in Literature

To design the camber morphing wing on the CHANGE project, a method to optimise a skin laminate tailored to match a specific aerodynamic shape was discussed, however time did not permit the development of such an analysis tool. Instead, a quasi-isotropic CFRP skin laminate with constant thickness was selected. To size the actuator, the necessary loads to support the aerodynamic loads and structural elastic loads were evaluated separately and summed [47]. The reaction forces required to support the aerodynamic loads were evaluated from a simplified FBD representation of the system as depicted in Fig. 3.1. It shows the trailing edge morphing system represented as a rigid body supported at two points. A similar assessment was also done on the leading edge. Actuation loads to support the elastic spring back of the skin in morphed configurations was evaluated with ABAQUS [15].

The design approach undertaken in CHANGE was able to output a structurally sound skin design and actuator pair, although the system was not optimized for minimized actuation loads, and the final aerodynamic shape was not necessarily the best. Further investigation into literature revealed how aeroelastic analysis and optimization tools have been developed for the design of morphing wings.

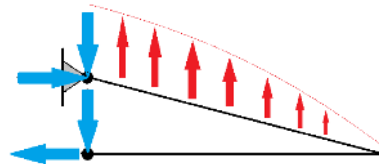


Figure 3.1: FBD representation of the aerodynamic load evaluation for the CHANGE wing [47]

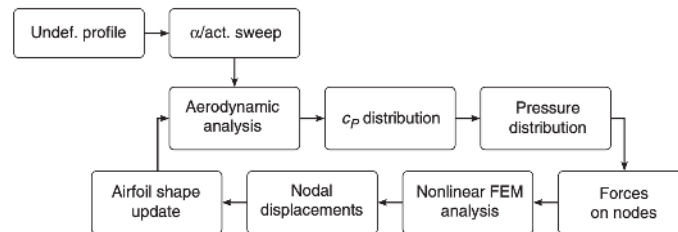


Figure 3.2: Static aeroelastic simulation iteration loop in the work of Molinari et al. [38]

3.1.1. Aeroelastic design and optimization frameworks

The aero-structural optimization developed by [38] to design a camber morphing airfoil coupled a static aeroelastic simulation tool with two different optimization methods. Static aeroelastic analysis was performed by interfacing a non-linear structural model built in MD NASTRAN [13], a FEM tool, and XFOIL [27], a 2D aerodynamic analysis tool built with panel code methods. The iterative operation of the aeroelastic analysis is presented in Fig. 3.2. It shows how the aerodynamic analysis was used to calculate pressure distributions across an airfoil to map them onto nodes in the structural model as equivalent pressure loads. From the structural analysis, nodal displacements were extracted to generate newly deformed airfoil shapes to feed into XFOIL to close the iteration loop. The simulation completed once the deformed shape converged. Interpolation routines compensated for mismatching meshes between the two software.

The two methods of optimization which were trialed in the same work included: i) A conventional method where a target shape was set and the structure was optimized to meet it, and ii) a concurrent method where simultaneous aerodynamic and structural optimization was carried out. Better solutions were realized from the second method as the optimum structure was able to deform to the optimum aerodynamic shape. The first approach on the contrary resulted in structural designs which were closely able to match the target shapes, but never accurately replicate it. The limitation of the second approach was the extensive computing resources required to optimize the aerodynamic and structural performance simultaneously.

In the work of Previtali et al. [45], the design of the camber morphing airfoil focussed on optimizing the rib structure, spar/stringer structure, skin thickness, corrugation, actuation points and neutral profile shape to maximize the rolling moment coefficient (C_L) achievable by the wing when morphed. MSC NASTRAN [3] and XFOIL were coupled to perform FSI analysis, with the MATLAB [5] Global Optimization Toolbox used to carry out the optimization work. Within Fig. 3.3, it can be seen how the optimization process was integrated with the FSI simulation. A candidate for an optimized structure was constructed for analysis in MSC NASTRAN. From this model,

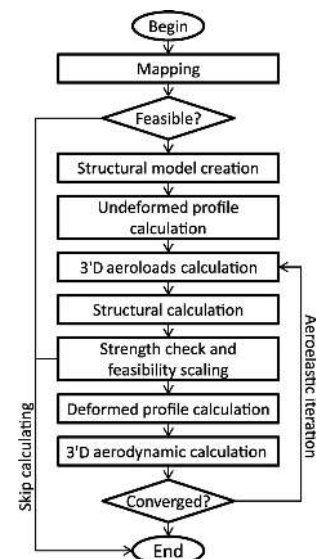


Figure 3.3: FSI evaluation algorithm employed by Previtali et al. [45]

interpolation of nodes from the FEM model could be used to build an aerodynamic profile input for XFOIL from which the pressure distribution across the airfoil could be calculated using viscous formulation (beneficial to approximate skin friction drag). The beginning of an aeroelastic iteration began with an extension of the 2D XFOIL analysis to calculate a 3D pressure distribution across the wing section by applying the Non-linear Extended Lifting Line Theory (ELLT). The calculated pressure distribution was applied to the FEM model as concentrated nodal forces to carry out the structural analysis. The results were imported into MATLAB to scale elements or reduce actuation limits if strength limits were exceeded. Several other steps were carried out to determine the C_L . Convergence was achieved through monitoring the delta in C_L for each iteration and confirming it was below an error bound.

Bilgen et al. [20] setup a static aeroelastic analysis tool to be able to optimize the skin thickness for a MFC actuated camber morphing. MATLAB was used to interface XFOIL and ANSYS [4] to complete a 2D FSI assessment. In Fig. 3.4 it is shown how each aeroelastic iteration started with an XFOIL analysis to calculate the pressure distribution, which was fed into an ANSYS structural model. From the structural analysis, a new deformed shape was calculated which fed into XFOIL to complete the iteration loop. The simulation was completed when the deformations and aerodynamic parameters such as lift converged. In this instance, an optimization algorithm was not employed, but rather the behaviour of the system was analysed by varying singular design variables at a time to see the variation in performance. An optimum design was found by analysing the trends in performance with varying design parameters.

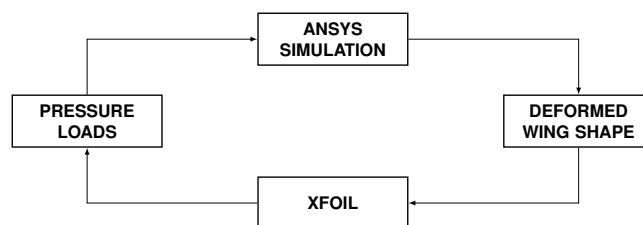


Figure 3.4: FSI analysis iteration loop utilized by Bilgen et al. [20]

Daynes and Weaver [24] presented a similar approach in the design of wind turbine blades, but with the use of ABAQUS. FEM and XFOIL simulations were completed independently, with MATLAB used to pass information between the two using interpolation functions to account for mesh mismatches. Aeroelastic equilibrium was judged by assessing the convergence of the lift coefficient of the airfoil. To tailor the stiffness of the morphing flap, it integrated this FSI loop within a linear parametric analysis where trial and error was used to design an optimum structure which could withstand given aerodynamic loads and maintain shape. Attempts to use viscous formulation were unsuccessful due to lack of convergence of the aerodynamic model in some cases, hence inviscid analysis was used. Results were verified through wind tunnel tests and more accurate non-linear analysis.

To develop an analysis process for a gapless trailing edge morphing wing, De Gaspari and Ricci [26] proposed a two level optimization approach to minimize energy required to deform morphing skins in an effort to steer away from the use of unconventional skin materials. They firstly optimized the aerodynamic shapes to find the best compromise of aerodynamic performance and deformation energy related to the airfoil skin. In the second stage they optimized the internal structure to be able to achieve desired load paths to uphold the aerodynamic morphing shape in the given flight conditions. They were able to use XFOIL with FEM algorithms to perform the FSI which supported the optimization process of the sub-structure. Generic optimization algorithms were used.

In the optimization of variable stiffness skins for morphing wings [49], an aeroelastic formulation was built to couple Euler-Bernoulli beam co-rotational element to a 2D inviscid panel code. To optimize the skin stiffness, a predefined target shape was determined. The skin thickness was kept constant, and a symmetric balanced layup was enforced with a minimum of 8 layers. The design variables were the skin axial and bending stiffness, which could be altered to meet the required target shapes through assessment of simulated and targeted curvature. A gradient based optimization procedure was used.

To develop the FishBAC concept, a coupled FSI loop was used to determine the static aeroelastic

equilibrium shape to predict lift distribution. The aerodynamic solver was once again XFOIL, although airfoil definition in this instance was determined from neutral axis deformation of the skeletal backbone [54]. Understanding the deformed shape of the back bone allowed for a valid prediction to be made on the deformed airfoil shape given so many stringers were used to maintain airfoil thickness. The aerodynamic analysis was conducted with viscous formulation to better predict skin friction drag. The structural model was based on the Euler-Bernoulli beam theory, with aerodynamic forces applied as a distributed loading across an equivalent beam. MATLAB was used to program the coupling. This analysis model was verified through finite element methods and structural tests.

It was evident from literature that the coupling of fluid and structural interactions is important in designing a morphing wing structure. These analysis frameworks are generally integrated with optimization algorithms to optimize morphing structures for defined objective functions. However, now several proprietary FEM softwares have this functionality in built to integrate well with their analyses packages. With this knowledge, a further assessment was completed on aerodynamic and structural solvers which could be used to build an analysis and optimization framework for the design of the Smart-X wing.

3.1.2. Structural solvers

The most commercially known solvers in the field of aerospace are ABAQUS, MSC NASTRAN, ANSYS and Altair's HyperWorks. All provide various optimization capabilities, however both ABAQUS and ANSYS do not allow for optimization of laminates. This functionality is however provided by MSC NASTRAN as part of the SOL200 optimization solver and Altair with the OptiStruct [8] package. Software such as HyperSizer [6] and modeFrontier [7] exist to interact with ABAQUS and ANSYS to provide laminate optimization capabilities, but the use of these is not favourable as run times would increase and separate scripts would need to be used to control the optimizer and the FE software.

Both OptiStruct and NASTRAN SOL200 utilize similar input files which can be scripted. Comparison of the two shows they are both industry leading, however the lamination parameters which can be altered with OptiStruct are very limited, for example ply orientation cannot be optimized at this stage [17]. Additionally, access to MSC NASTRAN is already available for students of the TU Delft Aerospace faculty, alongside a staff in the Structures and Materials department who have a wealth of knowledge in using it. MSC NASTRAN allows optimization of parameters such as ply orientation, ply thickness and individual ply properties [40]. Laminate styles such as symmetric or balanced can be enforced by using composite definitions and constraining equations. The optimizer also allows capabilities in enforcing ply dropping vs allowing a complete freedom in laminate properties for each mesh element. The level of freedom, and the ability to enforce design constraints with equations proves to be a highly sought out asset in the optimization of the laminate skin.

One of the associated limitations of this tool is that optimization work can only be built around a linear structural analysis. For morphing wings, this could be a critical issue given the system deformations can be large to introduce geometric non-linearities. Limitations in linear optimization could cause issues, however an assessment could be done to determine the degree of variation in behaviour between linear and non-linear models.

From evaluation of all structural solvers considered, MSC NASTRAN came out to be the best tool choice for this application for its laminate optimization capabilities.

3.1.3. Aerodynamic solvers

In coupled FSI analyses, XFOIL has been the most cited aerodynamic solver. With its 2D panel code formulation and script interface, it provides a robust and quick simulation tool to analyse flow over airfoils. The solver is commonly used in conjunction with the aerodynamic strip theory to be able to extend the 2D results to approximate flow over a wing span. The basis of this theory is that a wing is sub-divided into a set of small spanwise strips, for which the lift and pitching moment on each strips is

modeled as if the strip had an infinite span. The lift distribution for each strip can be calculated with XFOIL. A critical limitation of this theory is that interaction between strips is no longer considered, and therefore Three-dimensional (3D) flow effects are discarded. This method of analysis heavily reduces computational time in comparison to using high fidelity Computational Fluid Dynamics (CFD) tools, but limits some accuracies.

Inclusion of 3D flow distribution across the wing span has been integrated with XFOIL in some literature with the use of additional formulations such as ELLT. These methods have been validated with high fidelity analysis tools and wind tunnel tests to show promise in improving model accuracies without having to use computationally heavy simulation tools.

Viscous or inviscid flow models can be selected for analysis in XFOIL. Inviscid flow models always result in quick run times, however predictions of skin friction drag and boundary layer separation are compromised. Viscous flow models on the other hand introduce difficulties in model convergence [24] for poorly defined airfoils and airfoils approaching their apparent stall angle. A comparative assessment presented in Sec. 3.2.4 would show that at low angles of attack, results of viscous and inviscid flow models are comparable.

Higher fidelity computational tools such as ANSYS Fluent and XFLR5 do exist for CFD calculations which overcome some of the limitations of XFOIL. However these tools are difficult to interface with using scripts and their run times substantially increase to achieve higher model accuracies. The additional benefit they provide in calculating flow characteristics may be useful for analysing the flow over the structure in detail, however in the design process this level of detail is not required.

3.1.4. Summary of review

A review into literature showed how aeroelastic models are developed and integrated with optimization algorithms to design viable morphing structures suited to their applications. The analysis models are built with interfacing a structural and aerodynamic solver into an iterative analysis loop to converge on a static aeroelastic equilibrium shape. The optimization algorithms are generally run as stand alone systems integrated with the analysis framework, using formulations to propose design solutions able to minimize or maximize an objective function.

A similar approach could be taken for this design process, however rather than building a separate optimization algorithm to integrate with the analyses softwares, softwares with this functionality built in were sought out.

Investigations into structural solvers showed that MSC NASTRAN provides functionalities to be able to optimize composite laminates which would be highly beneficial for this design application. Additionally, all input files for NASTRAN can be scripted, hence interfacing with the solver is relatively simple.

A review of aerodynamic solvers presented the use of XFOIL in conjunction with strip theory assumptions to be best method of approximating flow over a wing span with sufficient accuracy, minimal computation time and script interface. The solver could be integrated with ELLT to better approximate 3D flow distribution across the wing span if necessary.

3.1.5. Selected software environments

With the softwares selected to build the aeroelastic optimization framework, an extensive review into the workings of these individual tools had to be carried out to understand how to interface with them.

NASTRAN

NASTRAN simulations are all carried out by running an input BDF which feature an organized input of simulation type, nodal and mesh specification, material selections, element types, boundary conditions, load specification, etc. A typical BDF to analyse a cantilevered I Beam, loaded with 100N (as depicted in Fig. 3.5) is shown in Fig. 3.6. This bulk data can be generated by typing the whole structural model out in the format required, or with the use of other proprietary software such as MSC PATRAN, which has a Graphical User Interface (GUI) to assist with model setup. Each bulk data entry, known as a bulk data card, has a specific style of input (specified in their reference guide [41]) which needs to be followed to ensure that the solver can read the data correctly to perform the analysis. Multiple sub cases can be run in a single analysis as well which proves to be especially beneficial for optimizing all bend/twist subcases simultaneously for this application.

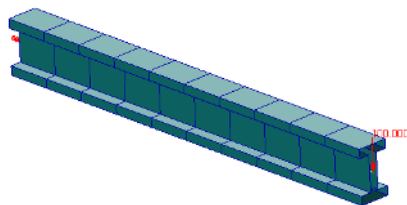


Figure 3.5: Cantilever beam analysis model built in PATRAN

Solver specification	→	SOL 181 CBAR
Case specification	→	TITLE = MSC.Nastran job created on 21-Oct-20 at 16:41:38 ECHO = NONE SUBCASE 1 \$ Subcase name : Default SUBTITLE=Default SPC = 2 LOAD = 2 DISPLACEMENT(SORT1,REAL)=ALL SPCFORCES(SORT1,REAL)=ALL STRESS(SORT1,REAL,VMOMISES,RIEIN)=ALL BEGIN BULK
Result request specification	→	\$ Direct Text Input for Bulk Data PARAM PDST 0 PARAM PRTMAXR YES
Mesh element specification	→	\$ Elements and Element Properties for region : beam PBARL 1 1 11 5. 2. 8. 12. \$ Pset: "beam" will be imported as: "pbarl.1" CBAR 1 1 1 1 2 0. 1. 0. CBAR 2 1 2 3 0. 1. 0. CBAR 3 1 3 4 0. 1. 0. CBAR 4 1 4 5 0. 1. 0. CBAR 5 1 5 6 0. 1. 0. CBAR 6 1 6 7 0. 1. 0. CBAR 7 1 7 8 0. 1. 0. CBAR 8 1 8 9 0. 1. 0. CBAR 9 1 9 10 0. 1. 0. CBAR 10 1 10 11 0. 1. 0.
Material specification	→	\$ Referenced Material Records MAT1 1 70000. 2
Node data specification	→	\$ Nodes of the Entire Model GRID 1 0. 0. 0. GRID 2 20. 0. 0. GRID 3 20. 0. 0. GRID 4 20. 0. 0. GRID= 5 30.99999961853027 0. * 8. GRID= 6 49.99999961853027 0. * 8. GRID 7 00. 0. 0. GRID 8 70. 0. 0. GRID 9 00. 0. 0. GRID 10 00. 0. 0. GRID 11 100. 0. 0.
Load and boundary condition specification	→	\$ Loads for Load Case : Default SPCADD 2 1 LOAD 2 1. 1. 1 \$ Displacement Constraints of Load Set : fixed SPC1 1 123456 1 \$ Nodal Forces of Load Set : force FORCE 1 11 0 100. 0. -1. 0. ENDATA

Figure 3.6: An example BDF of a cantilevered beam

Geometric inputs in PATRAN are completed by importing parasolid, iges, step or similar file types into the system, on which all boundary conditions, mesh specifications, loads, etc. can be applied.

All NASTRAN files can be executed from 'Command Prompt' or 'Terminal', without the need to push a 'run' button in a GUI. Results are output to another file type, *.f06. These files present a wide array of data which is requested in the BDF and includes content such as nodal deformations, stresses and strains. The data is structured and easy to read by MATLAB to record all necessary results for analysis. An extract of a typical *.f06 file which was produced from simulating the cantilevered beam is shown in Fig. 3.7.

Several additional data cards are defined in the BDF when an optimization analysis is to be run. Beyond general solver parameters, an objective function with design variables and design constraints have to be specified to aid the solver in finding solutions within appropriate bounds. The specifics of setting up an optimization analysis is discussed in Sec. 3.4.1.

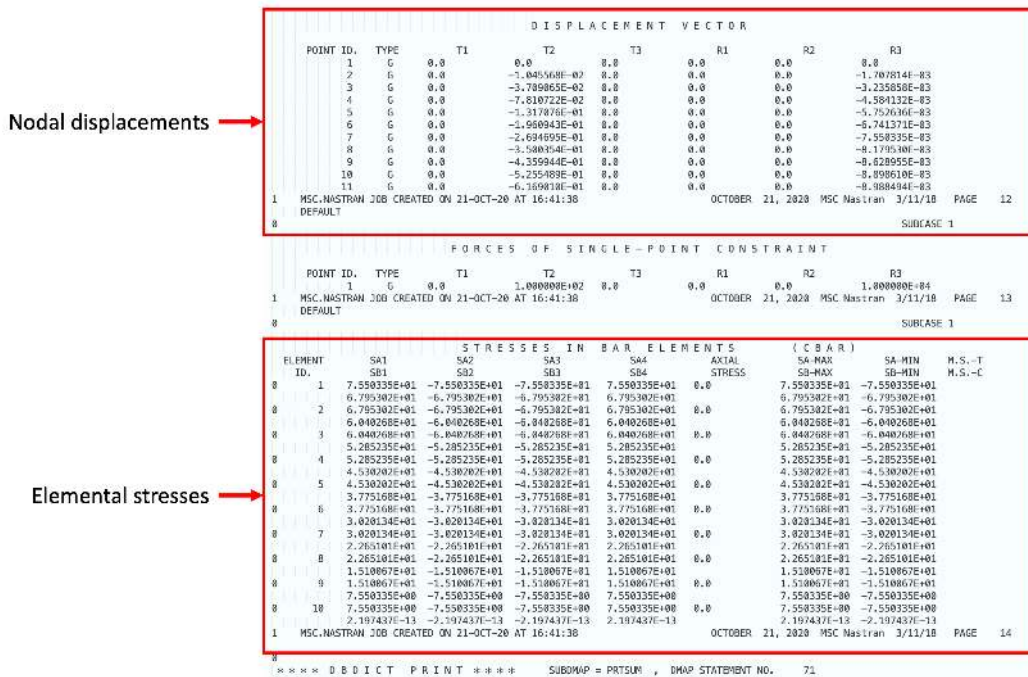


Figure 3.7: An example of a results file showing nodal deformations and elemental stresses for a cantilevered beam

XFOIL

XFOIL analyses are run directly from 'Terminal' or 'CommandPrompt'. Simple text inputs are used to setup and navigate the analysis. The most basic analysis method is carried out by first specifying the airfoil through either a NACA specification or user input of a text file with airfoil coordinates, followed by a specification of the angle-of-attack (α). This returns an inviscid pressure distribution with polars calculated. All this data can be exported to text files which can be read by MATLAB. The interface is shown in Fig. 3.8 on the left, with the results of the analysis shown on the right.

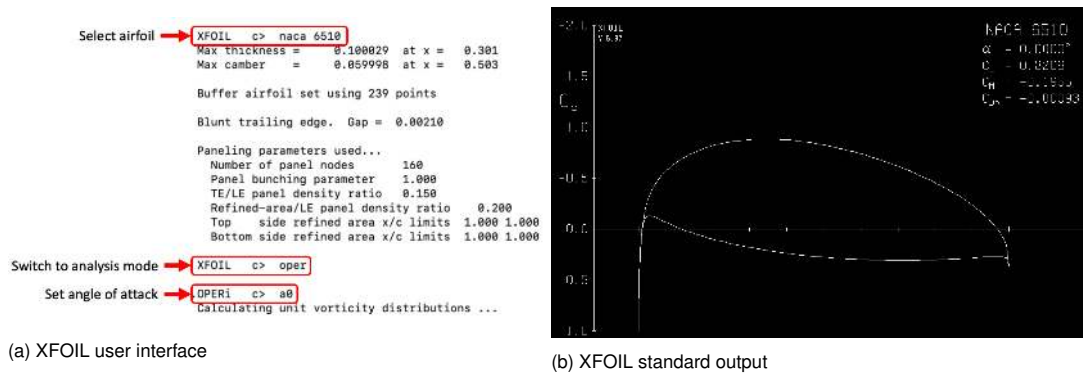


Figure 3.8: XFOIL user interface to evaluate pressure distributions across an airfoil

User input of the airfoil is done in a text file with sorted x, y coordinates, with the first point starting at the trailing edge, then accumulating all the points along the top surface to the leading edge, and then returning back to the trailing edge along the bottom surface.

Several alterations can be made to the panelling of the selected airfoil, such as number of panel nodes, distribution and density of nodes at the LE/TE, etc. Specification of these are essentially means to define the 2D aerodynamic mesh.

MATLAB

The MATLAB environment is well known by most, but several important functions are presented here which were critical to interface and execute these two simulation tools. Firstly, all inputs to 'Command-Prompt' or 'Terminal' could be made with the MATLAB 'system()' function, which is able to take in the exact input specified in MATLAB and execute it. Text file reading functionalities were offered by functions such as 'fscanf()', and writing abilities were offered by 'fprintf()'. Interpolation of data between mismatching meshes could be carried out in 3D with, 'griddata()'.

3.2. Linear Inviscid Aeroelastic Analysis

3.2.1. Model approach

A simplified representation of the method envisioned to carry out the static aeroelastic analysis is presented in Fig. 3.9. The baseline wing geometry would be imported into PATRAN to be able build the FEM model in which boundary conditions capturing the behaviour of the TRIC interface and actuation inputs could be included. A NASTRAN BDF could be generated with this information which is run to extract a deformed wing shape that can be used to generate an aerodynamic analysis model. Pressure distributions would be calculated on airfoils extracted at discrete spanwise positions with XFOIL to be able to build an aerodynamic strip model approximating the pressure distribution across the wing. These aerodynamic pressure loads would then be appropriately encoded in the NASTRAN simulation file, to complete a single aeroelastic iteration. Convergence of deformed wing shape, and hence aerodynamic lift and actuation loads exits the aeroelastic analysis loop.

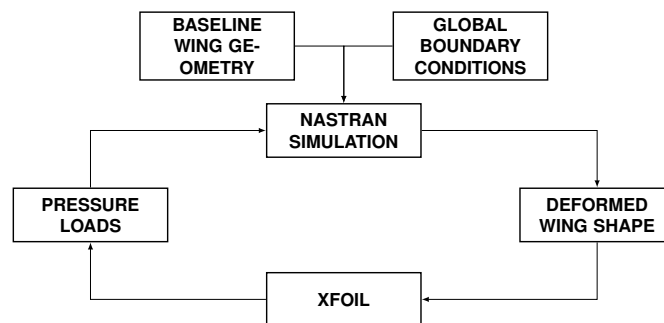


Figure 3.9: Aeroelastic analysis method overview

Model development began with setting up a linear inviscid analysis model to prepare the structural/aerodynamic analysis interfacing script in MATLAB. This was followed by extending the analysis to perform non-linear inviscid analysis which would take into consideration the geometric non-linearities caused by the large deformations of the trailing edge morphing surface. The non-linear analysis results would be compared against linear simulations to verify if the native linear solver in the NASTRAN optimization package would be sufficient in modelling the structural behaviour of the system. The integration of the optimization assessment within the aeroelastic analysis framework would conclude the design model development to be able to use it to design the wing skin laminate.

3.2.2. Simplifications and assumptions

With the goal of designing a wing skin laminate and building a surrogate model, the aeroelastic simulation tool had to accurately approximate the FSI interaction of the Smart-X wing with the surrounding airflow. Several levels of complexity could be built into it, however each added element would increase development and/or computation time. To still extract the most out of the analysis model, but within a reasonable timeframe, several model simplifications and assumptions were made, which are listed below. Some of these choices were made valid by introducing certain design choices, whereas the limitations of others were evaluated through other means. The model accuracies needed for the design process and the surrogate model varied, hence model assumptions could be varied accordingly. Within this section, the assumptions relevant for the design process are listed:

- A strip model approximation would be used to model flow over the wing, without consideration of 3D flow effects to minimize computation time. This would have several implications:

A rectangular lift distribution would be assumed along the span, which would over estimate lift load near the wing tip, in comparison to the root. This would mean that a more conservative design would be evaluated near the wing tip which was considered allowable.

Influence of wing tip vortices would be discarded without consideration of 3D flow effect,

hence drag predictions would be compromised. However, given the minimal frontal area of the wing, these drag effects were not considered substantial enough in altering the structural design.

- Inviscid flow conditions would be used to calculate the flow distribution across the wing. With its reduced computation time, this method of analysis still predicted a very similar pressure distribution across the wing in comparison to viscous formulation at low angles of attack, with a slight overestimation on the lift coefficient. The comparative assessment carried out to check the influence of flow viscosity is discussed in Sec. 3.2.4. Further implications of this assumption included:

Estimation of skin friction drag was compromised, however this would not play a significant role in design as majority of the design would be influenced by the pressure distribution on the trailing edge.

Prediction of boundary layer separation was compromised, however this would only produce more conservative designs. The risk of long run times and unconvverging solutions trying to predict this phenomena was less beneficial than outputting conservative but usable designs.

- With an assumed rectangular flow distribution across the wing, it was opted that a single representative module could be analysed, i.e. a wing section spanning only $300mm$. This simplification was made to be able to improve the computational efficiency by reducing the size of the structure analysed. This choice would mean that the influence of spanwise bending and torsion on the local angle-of-attack for each wing module would be discarded. To overcome this assumption, it was decided that the wing box would be designed rigid enough to minimize the local change in angle-of-attack per module in the most adverse design conditions.
- Forward of the rear spar, the wing section could be modelled structurally rigid in the analysis model as morphing was to only be considered on the trailing edge. The final laminate forward of the rear spar would also be designed relatively rigid to ensure this assumption would hold true.
- Actuation would be carried out with nodal displacements at the two span extremities of the module, rather than using a distributed load patch. This simplified setting model inputs, and the ability to alter mesh resolutions very quickly.

3.2.3. Development of the FEM model

With PATRAN, the initial linear NASTRAN analysis model (designated the code SOL101) was setup. The geometric definition of the wing section was carried out in CATIA, by modelling a NACA 6510 airfoil section with two spars, forming dimensions of 500mm chord x 300mm span. Only the web of the spars was modelled as the system would be assumed rigid forward of the rear spar in analysis. A 10mm wide cut was introduced aft of the rear spar on the bottom skin to be able to capture the workings of the TRIC concept. The intended lip offset was not originally modelled in the tool development process however its influence was assessed later in the design process and is discussed in Sec. 3.5.

The boundary conditions that were applied in the structural model are presented in Fig. 3.10. As spanwise bending effects did not need to be considered, the wing box was rigidly fixed on both sides of the wing section. To capture the TRIC concept, the cut in the skin was bridged by an actuator pair at each end of the module. The actuation was controlled by displacing the designated actuation nodes in the chordwise direction (the reaction loads at these nodes would represent the actuation forces required to achieve the morphing deformation). Finally, the sliding edge was restrained to only be able to slide in the chordwise and transverse directions, with out-of-plane deformations hindered.

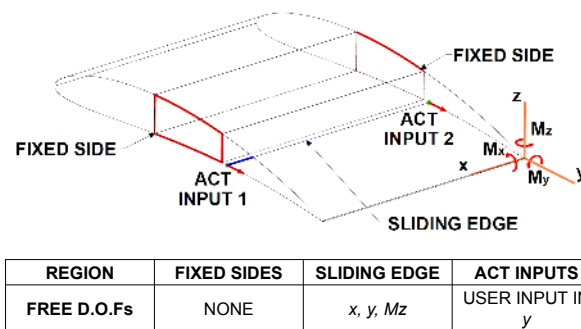


Figure 3.10: Visualization of the boundary conditions applied in the structural analysis model

The wing skin and box was originally modelled as Aluminium, with two different thicknesses used for the rigid and morphing regions. This choice was made to be able to focus first on building a coupling interface between the two software, after which complexities of composite laminate modelling could be introduced. The material properties used are presented in Tab. 3.1, and designated thicknesses are presented in Tab. 3.2. CQUAD4 shell elements with a sufficiently high resolution were used across the wing section. A mesh resolution study was completed to define the suitable mesh density which is discussed in Sec. 3.2.6. The 3D structural mesh used for all analyses is shown in Fig. 3.14a, with a 2D node distribution shown in Fig. 3.14b.

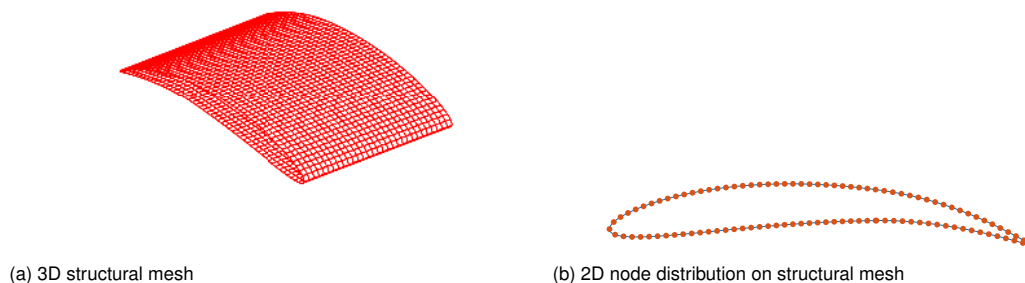


Figure 3.11: Resolution of structural mesh employed for aeroelastic analysis

All of the information modelled in PATRAN could now be exported to a BDF, capable of running with the NASTRAN solver. The initial runnings of the FEM model provided the deformations of all nodes and actuation loads which could be read and stored in the MATLAB environment to continue with the next

Table 3.1: Material properties

Property	Value
Elastic modulus, E	$70GPa$
Poisson's ratio, ν	0.3

Table 3.2: Thickness specification

Region	Shell thickness
Wingbox and leading edge	$5mm$
Trailing edge	$1mm$

stage of analysis. Several outputs were read into MATLAB including stresses, strains and actuation loads for post-processing.

In the first iteration, no pressure loads existed in the model, however they were introduced after the first aerodynamic analysis was completed. Pressure loads were introduced directly into the BDF with MATLAB's file writing functionalities to ensure the GUI did not need to be used.

3.2.4. Development of the aerodynamic model

To be able to implement the strip theory, deformed airfoil shapes were extracted along the span and parsed through XFOIL to calculate pressure distributions. The extraction process was carried out by effectively slicing the deformed structural model along the span to extract the chord and thickness position of the deformed nodes lying on the slice plane. These positions were used to generate the x , y airfoil definition coordinates to be imported into XFOIL. Sorting routines were created in MATLAB to order the coordinates as per XFOIL requirements: ordering points from the trailing edge to the leading edge along the top side, and then returning from the leading edge to the trailing edge along the bottom side.

The placement of these slice planes along the span coincided with the grid point locations along the span. This simplified the airfoil extraction process as a shape did not need to be interpolated. Hence, the slice planes represented the centre plane of each aerodynamic strip.

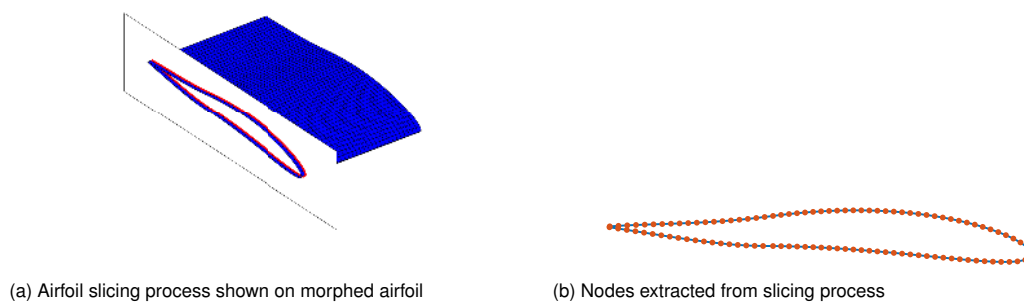


Figure 3.12: Airfoil extraction process carried out with slicing of structural mesh

It was found that when the airfoil was sliced directly from the structural mesh and taken into XFOIL, the number of points extracted from the structural model near the leading edge was insufficient in modelling the leading edge curvature in XFOIL. This resulted in problematic pressure distributions being evaluated near the leading edge which is shown in Fig. 3.13a. In the figure, pressure distributions calculated on an airfoil defined from the structural model nodes is overlaid on a pressure distribution calculated on a well defined NACA 6510 airfoil included in the XFOIL analysis library to visualize the deviation.

To overcome this issue, two approaches could be taken, either increase the mesh resolution near the leading edge in the structural model, or use the x , y airfoil definition of the NACA 6510 already available in XFOIL and use it to define the airfoil shape at the leading edge for all deformed airfoils extracted from the structural model. The latter approach was taken as increasing structural mesh resolution would only increase computation time. This simplification was valid as the leading edge was not expected to deform during morphing.

To script this, a coordinate source file was extracted from XFOIL (which defined the ideal NACA 6510 airfoil shape) and was imported into the MATLAB environment. Each time an airfoil was sliced from the deformed structural model, coordinates forward of the wing box were replaced with coordinates from this source file to provide XFOIL with a suitable resolution of points near the leading edge. The success of this approach was verified by reperforming the comparative analysis from Fig. 3.13a, with this new airfoil definition method. The results in Fig. 3.13b show how the distributions matched with this approach.

Once an airfoil is loaded into XFOIL, the program generates a 2D panel distribution, which represents the 2D aerodynamic mesh. The initial panel distribution is created with default panelling parameters, however each of these can be varied as required to improve modelling accuracies. Panelling parameters include the number of panels, panel densities, ratio of panels at leading edge vs trailing edge, etc. To be able to define the ideal panel distribution for converging results in this application, an extensive

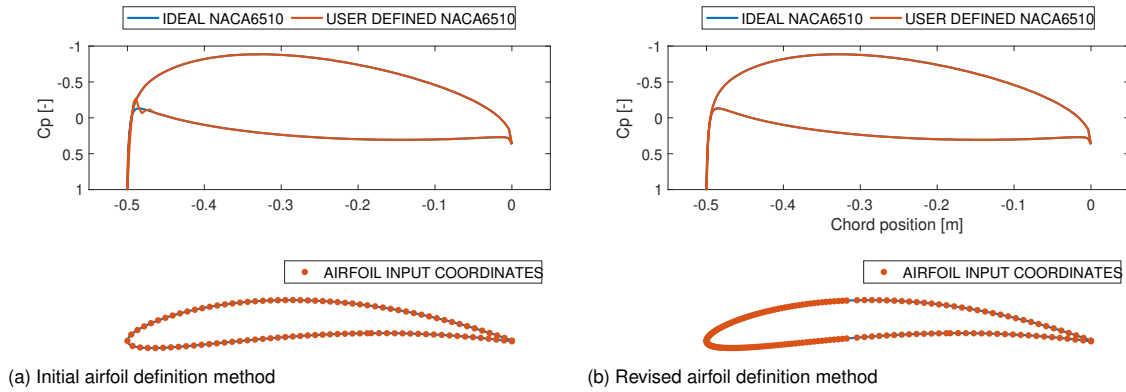


Figure 3.13: Influence of airfoil definition coordinate resolution on aerodynamic analysis

mesh convergence study was carried out, which is discussed in detail in Sec. 3.2.6. The resulting paneling distribution and hence panel node distribution that was selected for use from this study is shown in Fig. 3.14. In comparison to the node distribution on the structural mesh, within the aerodynamic model the node density near the leading edge is much higher to model the flow in this critical area properly.

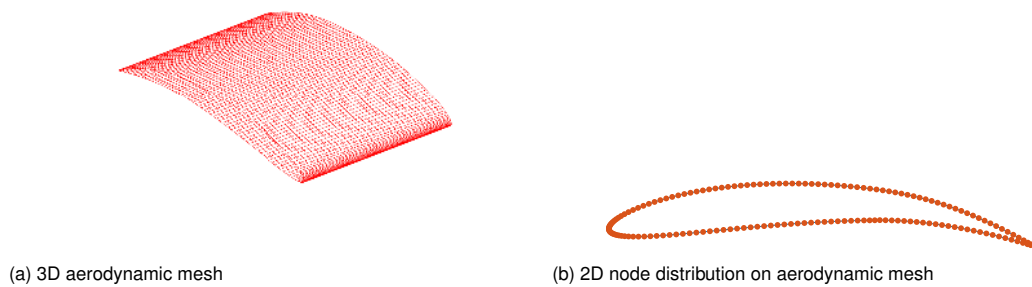


Figure 3.14: Resolution of aerodynamic mesh employed in aeroelastic analysis

With a panel distribution set, an analysis could be completed on the airfoil. For improved speeds of analysis, inviscid flow assumptions were preferred, however a comparative assessment on C_L calculations between the two types of analyses was conducted on the baseline airfoil shape for α ranging from -12° to 5° , in increments of 0.2° to understand the implications of this choice. In Fig. 3.15, the calculated lift coefficients for the two different models are shown. Viscous calculations were calculated with a Reynold's number of 1,000,000. The inviscid model shows a perfectly linear trend between α and C_L . The viscous model also shows a similar trend at low angles of attack, however when approaching higher negative angles of attack, results are unable to converge hence the discontinuous dataset observed. What this assessment confirmed is that stall would not be captured by the inviscid model, but simulation convergence was always guaranteed. It was also observed that the inviscid model also slightly overestimated the C_L amounting partly from the lack of boundary layer separation considered in this flow model. Moving forward with inviscid analysis would output more conservative designs but simulation would be quicker, and unlikely to fail due to lack of convergence which was a suitable compromise.

To perform the inviscid analysis on the imported airfoil, only an α had to be prescribed which was a user input. The final results including the polars and pressure distributions could be exported into text files which could be read by MATLAB.

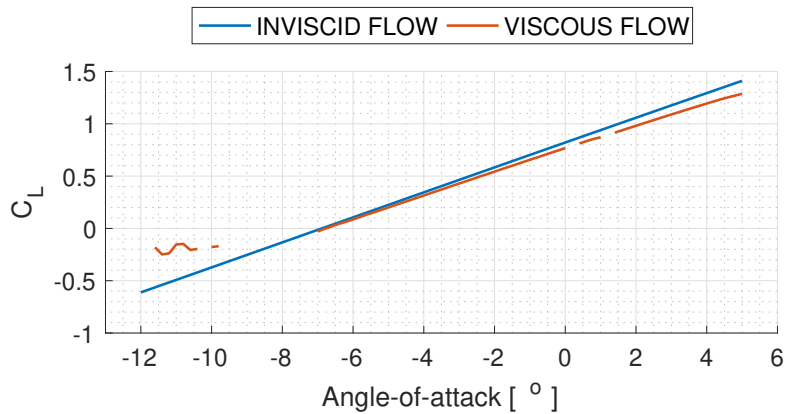


Figure 3.15: C_L evaluated on a baseline airfoil with viscous and inviscid flow models for varying α

3.2.5. Fluid-structure coupling

All pressure distributions were evaluated on 2D deformed airfoil shapes that were extracted along the span of the structural model, coinciding with the position of the grid points. This was used to build the strip model which is visualized in Fig. 3.16, overlaid on top of an example structural mesh for reference.

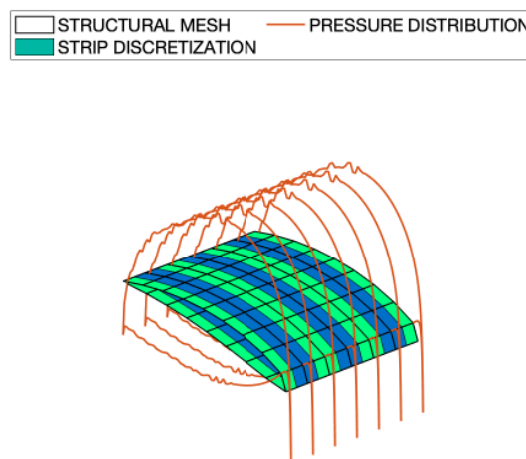


Figure 3.16: Simplified visualization of strip modelling method employed

Application of loads in NASTRAN required the specification of a pressure load that could be applied at the centroid of each element. To be able to do so, firstly a pressure distribution coinciding with the spanwise position of each element centroid had to be interpolated, from which a coefficient of pressure could be extracted at the equivalent chordwise position of the element centroid. This process is highlighted in Fig. 3.17 and it was carried out with the 'griddata()' function in MATLAB. The interpolation function in MATLAB implements a gridded linear interpolation based on Delaunay triangulation of 2D grid data [50]. As the interpolation is performed in 2D, the upper and lower pressure distributions of the airfoil have to be sampled from the aerodynamic mesh separately and projected independently on the projection of the FEM mesh. The function takes as input, the aerodynamic node positions in the chordwise/spanwise axis and the respective pressure coefficients calculated at those nodes from XFOIL, and the desired positions at which the pressure coefficients are to be interpolated, which for this case is the locations of the elemental centroids in the chordwise/spanwise axes. The function is called twice to perform upper and lower interpolations separately.

The evaluated pressure coefficient had to be scaled with air density and free-stream velocity to calcu-

late the equivalent pressure load that could be applied in NASTRAN model, as given by the following formula:

$$PLOAD = -1/2c_{p,fem}\rho V_{\infty}^2$$

The PLOAD2 card was used to define pressure loads at the centroid of all elements, and they were written into a new BDF to be run by NASTRAN to start the next aeroelastic iteration.

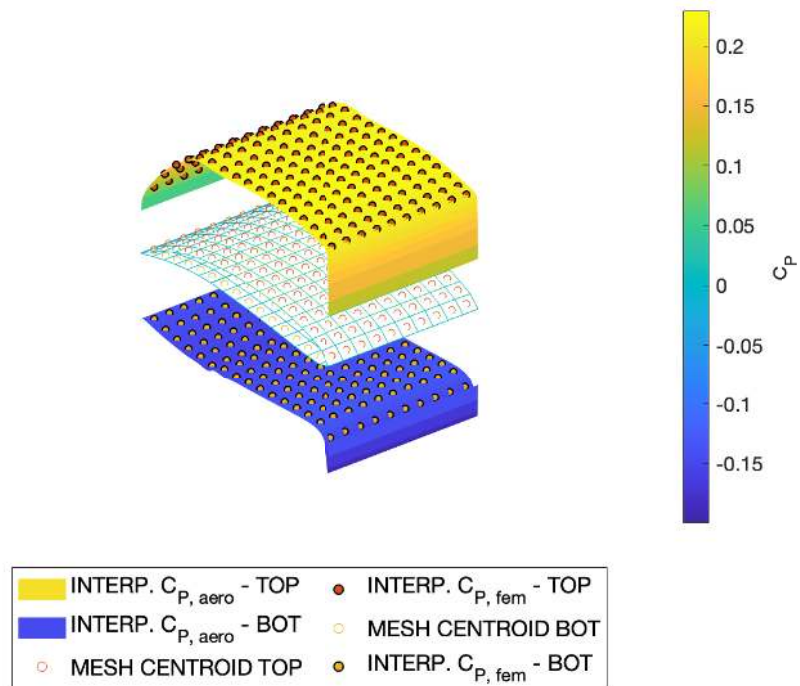


Figure 3.17: Interpolation method to sample $c_{p \text{ fem}}$

3.2.6. System verification

Several parameters had to be defined to ensure valid results were being output from the simulation tool, including the mesh resolutions of the aerodynamic and structural models to eliminate discretization effects, and convergence criteria to exit the simulation loop.

Simulation convergence

Of importance to the design process was the convergence of lift distribution and actuation loads which would result from the convergence of the deformed shape. To find a suitable convergence bound for the simulation tool, two bend down simulations were carried out to a high iteration count to be able to monitor the evolution of deformed shape, and therefore C_L and actuator loads. The simulation was carried out with 5° angle-of-attack, at $30m/s$. Default panelling parameters were used for the aerodynamic model, and a fine structural mesh with a seed size of $10mm$ was used for the structural model.

Given skin flexibility could influence how quickly a simulation would converge, for the two analysis models considered, one model was defined with a skin thickness of $1mm$ for the trailing edge morphing surface, and the second model was defined with a skin thickness of $0.5mm$. The evolution of the monitored parameters with increasing iterations is presented in Fig. 3.18 for both analyses.

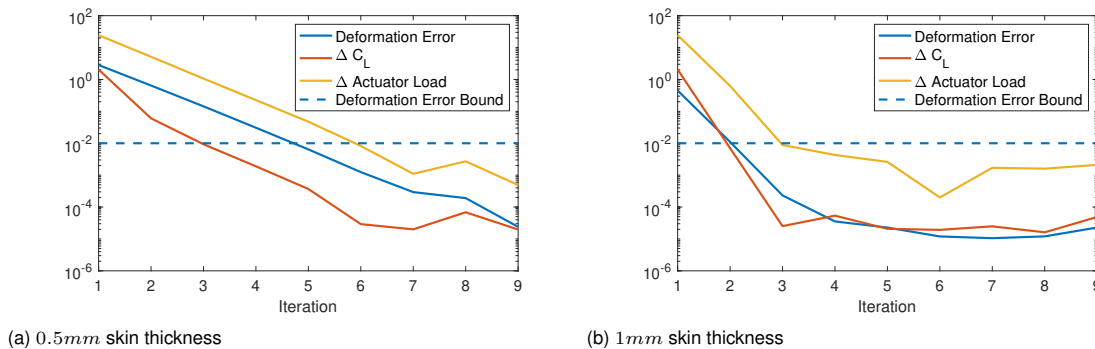


Figure 3.18: Aeroelastic analysis convergence assessment for models with varying levels of flexibility

A measure of the change in deformations was evaluated by calculating the change in deformation magnitudes at each node and then summing this difference. This equated to the deformation error, which is presented in the figures. For the stiffer model presented on the right, the change in actuation loads by the second iteration was in the order of $0.5N$, and the change in C_L in the order of 0.001 . These were very negligible changes in the critical performance parameters of the wing. The respective deformation error at the iteration count of 2 was 0.011 . For the more flexible system, at the second iteration, the change in actuation loads was still in the order of $5N$, which can represent a substantial portion of the load capacity of some actuators. By the fourth iteration, this change in actuation load was of a much lower order, as is the change in C_L . The total deformation error at the fourth iteration for the more flexible system was 0.03 . With this information, a convergence bound of 0.01 was considered robust in capturing the required information to a suitable level of accuracy. Therefore, simulation convergence was confirmed when the total deformation error of the system was ≤ 0.01 .

Mesh convergence study

The meshes from two different domains shared implicit dependency due to the data transfer taking place. The structural mesh resolution defined the accuracy in the deformed structure and actuation loads, whereas the resolution of the aerodynamic mesh defined the accuracy of the pressure distribution. To determine a suitable combination of both, a mesh convergence study was completed. Each mesh was refined separately in this study: Initially, a resolution of the aerodynamic mesh was evaluated, which was then fixed to continue with modifying the structural mesh.

Several panelling parameters could be modified in XFOIL, including node count, panel bunching and TE/LE panel density ratio. To select appropriate panelling settings, the change in C_L was monitored for three airfoil shapes while varying a single panel parameter at a time. The airfoil shapes analyzed were representative of the baseline, bend up morphing and bend down morphing shapes. The results of this assessment are presented in Fig. 3.19. For all parameters tested, the evolution of C_L was very minute, in the order of 10^{-3} or less. For a wing module of $300mm$ span, operating with a wind speed of $30m/s$, the resulting change in lift load is $0.55N$, which is negligible. With this finding, it was decided that the default XFOIL panelling parameters would be used, which would set the panel node count to 160 nodes, with a bunching parameter of 1.0 and density ratio of 0.15.

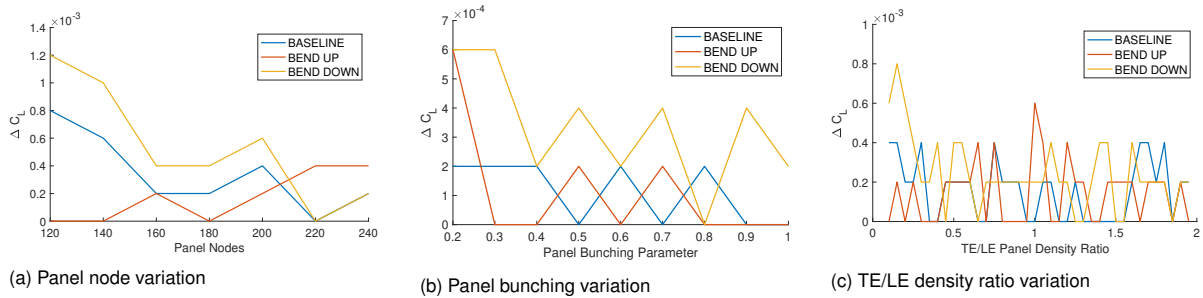


Figure 3.19: Variation in C_L from changing panelling parameters in XFOIL

To hone in on a suitable resolution of the structural mesh density, the three design subcases were simulated for varying mesh seed sizes, ranging from $30mm$ (coarse) to $10mm$ (fine), with the change in actuator loads monitored. The result is shown in Fig. 3.20. For this study, the convergence criteria discussed at the start of this section was employed to exit the analyses, which is why the resulting change in actuation loads presented in the plot are of such low order. What this showed was that structural mesh resolution did not substantially alter the results of the aeroelastic assessment, given that sufficient iterations were carried out to converge on a suitable solution.

For the simulated cases, increases in mesh resolution generally resulted in increases in run times; however, they were still completed within 2 minutes for the finest resolutions tested. It was beneficial to carry out the optimization work with a finer mesh resolution at the trailing edge morphing surface to have greater freedoms in optimizing the structure. Therefore it opted that the structural mesh resolution seed size would be set as $10mm$.

To keep the interface between the two software simple, varying the mesh densities in the structural model along different regions was not considered as the run times were quick. This functionality could be built in if necessary.

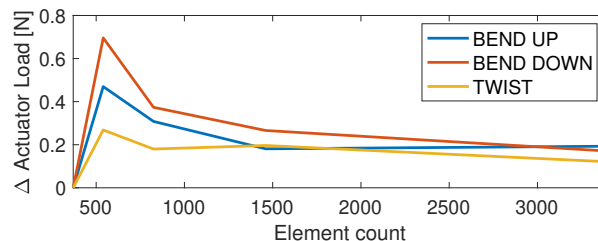


Figure 3.20: Structural mesh convergence study

3.3. Non-Linear Inviscid Aeroelastic Analysis Framework

To verify linear structural assumptions were valid for assessment, a non-linear FSI model was also built. The only variation with this system was that the non-linear static solver, SOL106, had to be used instead of SOL101. The most adverse morphing cases were analyzed to be able to compare behaviour between the linear and non-linear models. Peak bend up/down and twist cases were evaluated at 0° α and wind speed of 30m/s . Mesh densities were kept per the outcomes of the mesh convergence study.

Comparison of lift coefficients is presented in Tab. 3.3 for the two cases. The slight difference in C_L was caused by minute variations in structural deformations as presented in Fig. 3.21. Given that system behaviour did not substantially alter between the two models, the linear assumption was considered valid to conduct further optimization work.

It was later realized that with the integration of the offset lip in the structural model, the system deformation drastically changed with non-linear analysis. The outcomes and overcomings of this realization are discussed in Sec: 3.5.

Table 3.3: Comparison in lift with linear and non-linear structural models

Subcase	$C_{L,lin}[-]$	$C_{L,nl}[-]$	$ \Delta C_L $
Bend up	-0.277	-0.296	0.019
Bend down	1.464	1.423	0.041
Twist	0.823	0.847	0.024

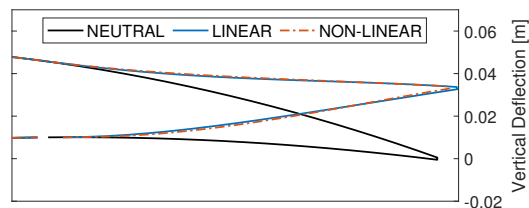


Figure 3.21: Linear and non-linear analysis comparison

3.4. Aeroelastic Optimization Framework

3.4.1. NASTRAN SOL200 overview

The NASTRAN SOL200 optimization solver is used to find the most optimum solution for a given design problem. For an efficient approach in finding the optimum, it utilizes a sensitivity analysis that can compute the rates of change in structural responses with changes in design parameters. With known sensitivities, the optimizer can better focus on which parameters to vary to find a design optimum.

To carry out an optimization, the system integrates an analysis and design model. The analysis model is representative of a typical FEM model which is the mathematical idealization of a physical system from which responses can be approximated, the accuracy of which is defined by the quality of input. Model inputs include mesh allocation, property designation and loads and boundary conditions specification.

In contrast, the design model considers changes which can be made to the structure to improve its design response. The desired improvement is defined by an objective statement (such as maximize stiffness or minimize weight). A bounding box for the design is defined by constraints on responses which are not exceeded, such as peak stresses, whereas the freedom in design choices are specified with design variables. The design space represents the collective mathematical region defined by setting design variables, constraints and objectives.

A comparison of the two distinct models can be visualized in Fig. 3.22. In the design model, there is only a design variable set which is the hole radius that is to be optimized to minimize weight. To ensure system is not without material to serve this objective, constraints on maximum allowable stresses are imposed.

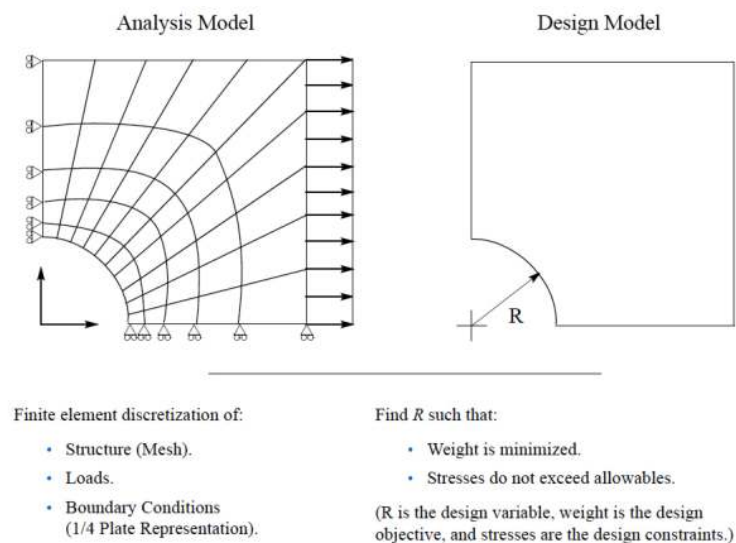


Figure 3.22: Representation of the distinction between analysis and design models [40]

Similar to an analysis model where a poor model definition leads to unusable results, a poorly defined optimization task will result in inaccurate, misleading or unusable solutions. It becomes critical that an appropriate design space is set to integrate with a well-defined analysis model as the optimizer is known to exploit inaccuracies in the analysis model to help perform the design task.

The interaction between the two is not a direct coupling, but rather a system approximation is built from the analysis model, where quick analyses can be run to approximate design responses to variable changes. With this information, an optimum design can be suggested, which is then analyzed in detail using FEM to verify if it satisfies design constraints and works towards achieving the objective. This process can be visualized in the flow chart shown in Fig. 3.23; however, a more extensive overview of

its workings is presented in Fig. 3.24.

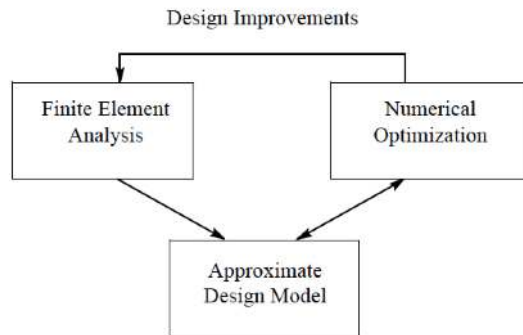


Figure 3.23: Simplified interaction between numerical optimizer working with the design model and the FEM model [40]

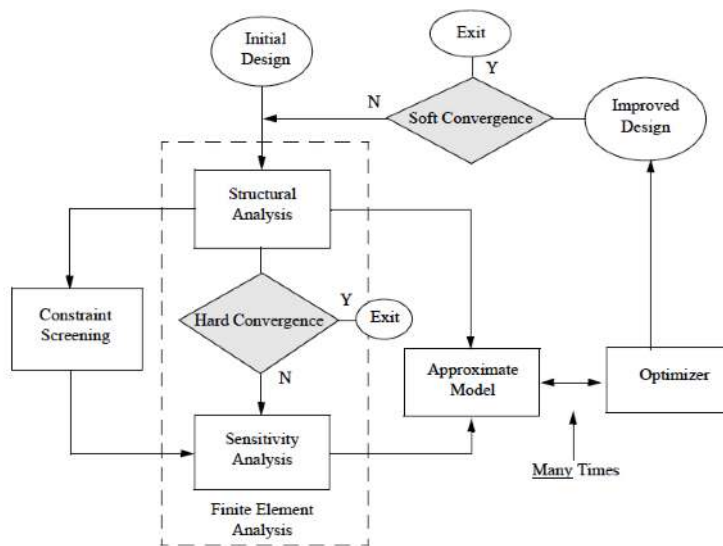


Figure 3.24: Detailed interaction between numerical optimizer working with the design model and the FEM model [40]

The typical optimization process takes an initial starting point for the design to run a structural analysis. The internal workings screen the constraints that will influence the redesign process and build a sensitivity analysis which feeds into the approximate model. The approximate model works with the numerical optimizer to suggest an improved design which is analyzed in detail. Each time an improved design is proposed, a design iteration is completed.

Two types of convergence are employed to exit an optimization analysis, hard and soft. Soft convergence considers the evolution of design variables from each design iteration. If variables don't significantly change, further structural analysis may not be warranted. A check is always done, however, the system is not on default programmed to exit at soft convergence. Hard convergence, on the other hand evaluates the changes in results from structural analysis through each iteration to be comfortable that a detailed assessment of the design has converged.

Results of a typical optimization simulation provide structural results from the initial analysis and last completed structural analysis with converged or unconverged design solutions. They additionally present the evolution of design variables for all design iterations.

3.4.2. Integration of SOL200

The previously run aeroelastic simulations only interacted with an analysis model. For each aeroelastic iteration, pressure loads were applied on an undeformed structural model with actuation inputs.

To be able to now optimize the skin design, a valid method of including the pressure loads into the analysis model would need to be implemented. The approach taken was to replace the SOL101 system with a SOL200 system in the original FSI loop, as shown in Fig. 3.25. This would mean that within each aeroelastic iteration, an optimum solution for the given design space and analysis environment would be found. This solution would be used, with its deformed shape, to recalculate the pressure distribution mapping through the slicing process. In effect, a new set of pressure loads would be evaluated, which would alter the solution of the optimum design for the next iteration. This risked further changes in pressure distribution, to essentially never be able to converge on a viable design. This stood as a prominent point of consideration on whether or not this approach would be viable, but it was trialled to determine what occurs.

A method of successfully using the SOL200 system with this approach was found, and its development method is discussed in the following sections. For successful convergence of the optimization problem, the convergence criteria on the deformation error had to be relaxed from 0.01 to 0.1. This was a requirement as slight changes in the optimum solution for each aeroelastic iteration meant following iterations had slightly different deformations. Given influential criteria on the lift distribution were being constrained in the optimization model, such as tip deflection, this relaxation was allowable as actuation loads were still converging to a suitable order of magnitude.

The required output of the simulation was a laminate design optimized to minimize actuation loads for all three sub-cases: i) bend up, ii) bend down, and iii) twist. The design space and analysis model had to be developed and modified respectively to achieve this.

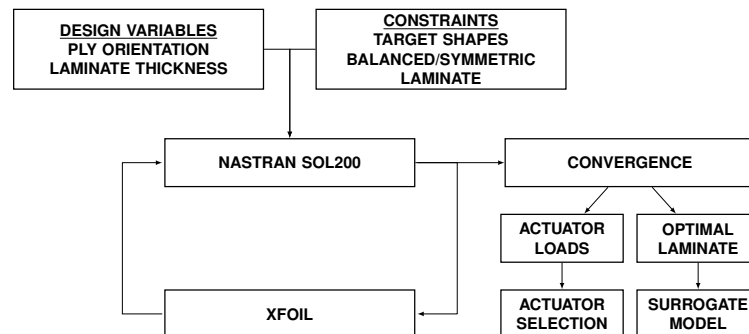


Figure 3.25: Aeroelastic optimization framework

3.4.3. Design model

The objective of the design was to minimize actuation loads for all subcases and be able to use the smallest actuators in this design. From all three, bend down morphing always required the highest actuation loads due to the significant camber induced combined with high angles of attack which maximized the pressure loads across the wing module. Therefore, the objective function set out to minimize the actuation loads for the bend down subcase, which would trickle down to minimized loads for the bend up and twist cases.

The necessity to simultaneously run the optimization task with all three subcases came down to verifying the design could achieve all three configurations by imposing design constraints on the tip deflection as shown in Fig. 3.26. m and n equated to the values presented in Tab. 3.4.

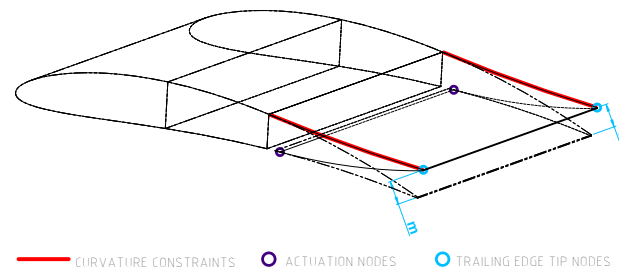


Figure 3.26: Design constraints employed in the optimization model

Table 3.4: Tip deflection constraints for various subcases

Subcase	m [m]	n [m]
Bend up	0.03	0.03
Bend down	-0.02	-0.02
Twist	-0.02	0.02

The design variables played with two laminate properties, fibre orientation and laminate thickness. Orienting fibres in specific directions alter the stiffness of the laminate. For example, fibres oriented in the spanwise direction would result in the lowest chordwise bending stiffness, which benefits reduced actuation loads. Similarly, reducing thickness also reduces bending stiffness of the skin, benefiting reduced actuation loads.

Therefore, the design variables for the composite laminate, which could be considered included ply angle and laminate thickness distribution across the morphing trailing edge surface. This could be done on a per-element level, across the entire morphing surface, or region by region. The freedom in setting design variables meant several different approaches could be taken to optimize the laminate. Therefore, a trial and error approach was used to try different methods till desirable results were achieved. It took three different approaches to acquire the desired results:

- Trial 1: Optimization of ply angle and laminate thickness for a variable thickness morphing surface
- Trial 2: Optimization of ply angle and laminate thickness for a constant thickness morphing surface
- Trial 3: Optimization of a variable thickness morphing surface with constant ply angle

The method of implementing each attempt and lessons learnt are discussed in the relevant sections below.

3.4.4. Analysis model

Given simultaneous optimization of all three different types of morphing shapes had to be carried out, each subcase had to be now included in the single analysis model with 'SUBCASE' definitions.

Boundary conditions and assumptions from the previously developed analysis models could remain the same; however, actuation nodes were now to be loaded with nodal forces, rather than prescribing actuation displacements. This was a necessary change to be able to have actuation forces as design variables which can be minimized.

Mesh definitions could remain the same; however, material property designations would now need to evolve from the previously used Aluminium designations. At the leading edge and wing box sections, a rigid laminate structure could be enforced. For the trailing morphing region, several approaches were taken based on what design variables were considered. A laminate stack up of uni-directional fibre-glass plies (with properties also presented in Tab.3.5) was first used when simultaneous optimization of ply angle and laminate thickness was considered. When the optimization evolved to only altering laminate thickness with a fixed orientation, material designations were done with specified equivalent in-plane properties with variable material thickness.

Table 3.5: Material properties used for optimization analyses

Material	E_1	E_2	ν_{12}	G_{12}	Thickness, t
UD Fibre-Glass	38.6GPa	8.27GPa	0.26	4.14GPa	0.15mm (per ply)
Woven Fibre-Glass, ± 45	19.4GPa	19.4GPa	0.2137	10GPa	0.15mm (per ply)

3.4.5. Optimization approaches



(a) Optimization trials 1 and 3

(b) Optimization trial 2

Figure 3.27: Discrete design regions enforced in optimization analyses

Trial 1

The first approach created the most freedoms in the design space. The initial idea was to provide all possible freedoms to achieve the most optimized solution. In this, the design model enabled a variable thickness distribution on the trailing edge morphing surface with plies in the laminate able to take any orientation, given the laminate was balanced-symmetric overall.

A variable thickness distribution was made possible by discretizing the morphing surface into 10mm wide strips as shown in Fig. 3.27a. Each segment had a PCOMP symmetric laminate designation. 6 layers were defined; however, the symmetric designation meant the laminate would be analyzed with 12 layers. Each layer could take on two thickness values, 0.15mm to 0.001mm (equivalent to the ply not existing). Layers 1, 3 and 5 could be oriented from -90° to 90° . Layers 2, 4 and 6 were

parametrically linked to ensure they were the negative designation of layers 1, 3 and respectively, to ensure the laminate would be balanced.

Whilst building this system, it was realized somehow ply continuity would need to be constrained such that a ply doesn't change orientation as transversing along the chord. Additionally, once a ply is terminated in a certain region, aft of this region, the ply should not somehow be reintroduced. These constraints were challenging to enforce. Initial simulations without these constraints already presented a lack of converging results when run standalone (outside of the FSI loop) as there were many too many design variables. For this reason, this approach was discarded.

Trial 2

In a second approach, a degree of freedom was removed by constraining the thickness across the morphing surface to be constant. Two PCOMP entries could be used to model the composite on the top side and bottom side of the morphing surface, respectively. The two designated regions can be seen in Fig. 3.27b.

A 12-layer laminate definition identical to the setup of trial one was used, however now only in two design regions. Initially, a standalone system was analyzed to verify the workings of the solution system. The minimum actuation loads allowed were $0N$, with an upper limit of $90N$.

With a $0N$ minimum allowable actuation force, the optimization tended to recommend design solutions where all fibres were oriented in the spanwise direction. This threatened spanwise bending strength. Even with maximum strain constraints, preventing this impractical solution was unsuccessful. The alternative was to increase the minimum allowable actuation force for the bend down condition to promote off-axis fibres. This method worked, however, careful evaluation of the curvature of the top surface in the bend up configuration showed a non-ideal shape, with a near-flat surface from rear spar to the tip of the trailing edge as shown in Fig. 3.28. A more gradual change in curvature was desired.

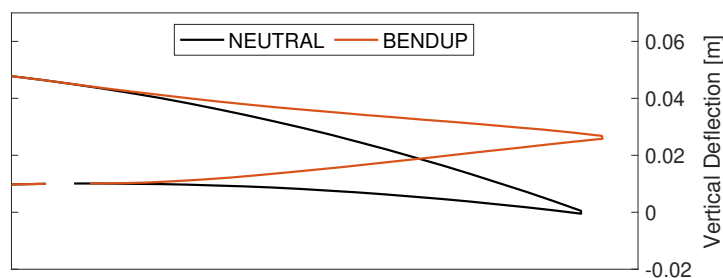


Figure 3.28: 2D representation of deformed wing shape for bend up configuration from stand alone analysis of trial 2

This could not be achieved with a constant thickness on the top and bottom surfaces. A variable thickness geometry would be necessary. Given the first attempt to complete this was unsuccessful due to the sheer number of design variables, it opted that the orientation of the fibres would be constrained to remove some of the design freedoms to promote convergence.

Trial 3

A ply dropping system with a constant fibre-orientation was envisioned for the trailing edge morphing surface.

Given a balance between chordwise strength and minimal actuation force could be driven by fibre-orientation, it was realized that the fibres could be oriented in the $\pm 45^\circ$ direction, to capitalize on strength and minimal actuation loads. Selection of this orientation also provided additional benefits:

- Woven $0^\circ/90^\circ$ plies can be acquired and easily oriented to $\pm 45^\circ$ plies, which means with each ply drop, the laminate remains symmetric balanced.

- Lamination time was reduced as fewer layers would need to be used.
- Fibres did not need to be oriented differently layer-by-layer.

The trailing edge morphing surface was once again discretized in 10mm wide strips as shown in Fig. 3.27a. Each segment was designated a shell property designation with variable shell thickness. For all, the material was defined as $\pm 45^\circ$ woven fibre-glass with the equivalent in-plane properties highlighted in Tab. 3.5. The shell thickness could vary from 1.65mm (11 layers) to 0.15mm (1 layer).

At first attempt with this setup, the optimizer evaluated designs which had minimized actuation forces, however with kinked morphed surfaces in the bend up configurations as shown in Fig. 3.29. Additionally, ply dropping was not naturally enforced; it was found that plies could be reintroduced mid-chord. This is where it was realized that the solver was exploiting these unconstrained freedoms to minimize the objective function.

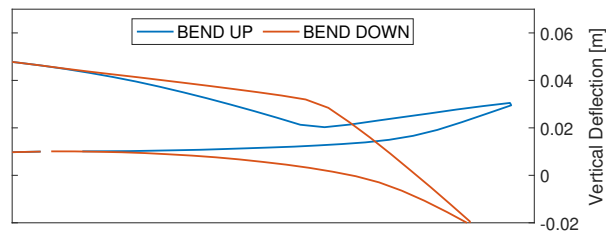


Figure 3.29: 2D representation of deformed wing for bend up/down configuration with no curvature constraints

This promoted the introduction of two design constraints, enforcing ply dropping by not allowing the thickness of the regions to increase in the chordwise direction, and preventing kinked surfaces by prescribing a vertical displacement range for several nodes on the top surface. This 'target shape' was enforced by prescribing displacements of every 3rd node to be within the predefined tolerances as shown in Fig. 3.30 for the bend up subcase. Similar was done for the bend down subcase, by also defining a prescribed range of vertical displacements on several nodes on the top surface. A target shape was not prescribed for twist beyond TE tip deflections as this would overconstrain the optimizer.

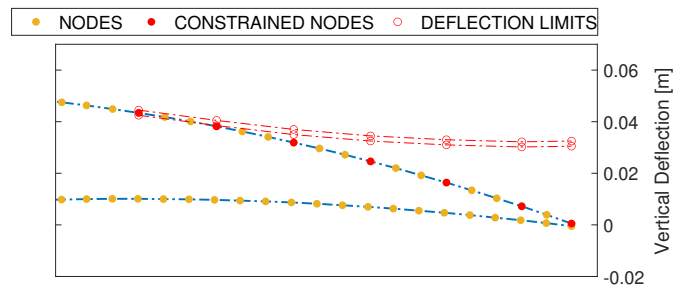


Figure 3.30: Method to enforce target shape on wing surface shown for the bend up subcase

With these constraints, more realistic solutions were being evaluated in the aeroelastic environment. Within the FSI loop, the designs were initially unable to converge. This resorted to the fact that if the minimum allowable for the actuation load was too low, the optimizer could not find a solution. For this reason, to minimize actuation loads with a converging design, minimum allowable loads were increased in increments of 10N until an aeroelastic equilibrium was reached with an optimum design. The potential cause of this was that the design space of the optimizer was too wide when the prescribed minimum actuation load was too low. By increasing the minimum load, the optimizer was able to find solutions with reduced ranges of freedoms.

The resulting system converged with a minimum bend down actuation load of 60N at each node. In the following section, the results of the analysis are discussed, with further implications to the actuation kinematic design.

3.5. Design Results

3.5.1. Morphing surface laminate specification

The final optimization approach with constant ply orientation and variable thickness distribution presented the most usable results for further detailed design. With a minimum applied load of $60N$ at each actuation node for the bend down subcase, the aeroelastic optimization simulation converged.

The resulting laminate specification is presented in Fig. 3.31. It shows the ply dropping sequence, starting with 11 layers at the rear spar, dropping to 4 plies at the trailing edge tip. On the bottom surface, it starts at 8 layers dropping to 2 layers. The converged deformed shapes are presented in Fig. 3.32. The respective actuation loads and chordwise lip travel for all sub-cases are summarized in Tab. 3.6.

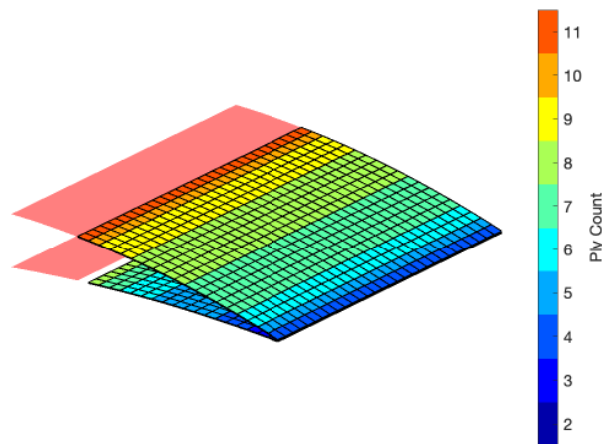


Figure 3.31: Laminate ply distribution on morphing trailing surface

Table 3.6: Actuation forces and nodal translations for each subcases

Subcase	Act1 Force [N]	Act2 Force [N]	Act1 Disp. [mm]	Act2 Disp. [mm]	C_L
Bend up	61	61	6.5	6.5	-1.7
Bend down	-60	-60	-4.5	-4.5	2.2
Twist	-50	23	4.5	-4.5	0.85

Given the optimizer was run with more relaxed convergence criteria, a high fidelity assessment was done by enforcing the laminate design in the SOL101 and SOL106 systems; however, now with the lip as well. Given the lip offsets the remainder of the bottom surface, there was a risk that the system would deform unexpectedly due to the additional moment created. This expectation was confirmed with a non-linear analysis of the system.

A revised geometric model was built with the lip offset and brought into the analysis environment. The sliding edge was raised by $1.65mm$ to sit on top of the lower rigid skin portion. The material specification was per ply distribution specified by the optimization results. A non-linear analysis of the bend up subcase showed a bulging shape came into effect as shown in Fig. 3.33. This was considered an unacceptable design limitation which had to be overcome.

Rather than reperforming the optimization, it opted that the thickness of laminate on the bottom surface would be increased one layer at a time until the morphing deformations took on an acceptable shape.

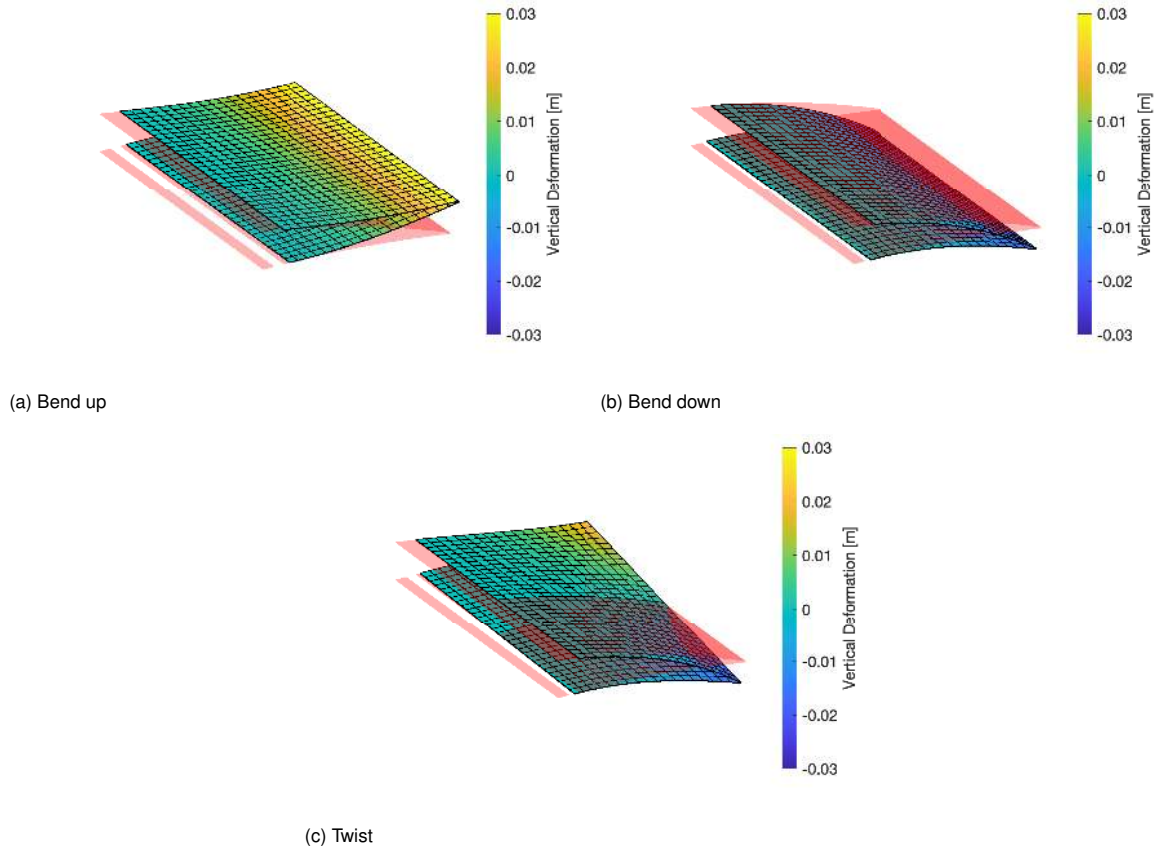


Figure 3.32: Morphing deformations for all subcases

It was realized that with two additional layers, the deformation from the non-linear system closely matched that of the linear system, as shown in Fig. 3.34.

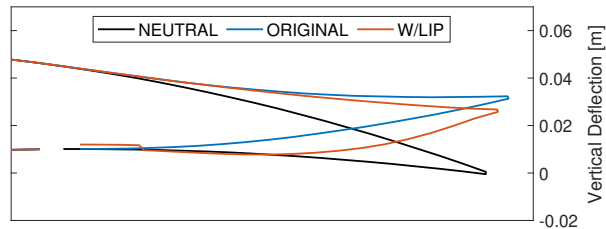


Figure 3.33: Simulation results with lip integrated into model

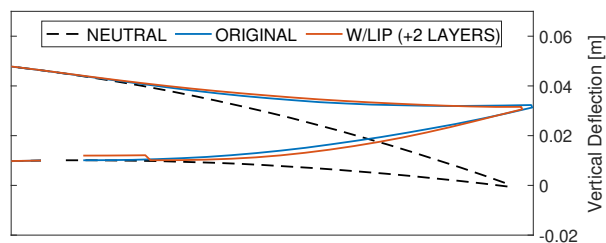


Figure 3.34: Simulation results with lip integrated into model and added thickness

The revised laminate thickness specification is shown in Fig. 3.35. Plies would be dropped from 9 to 4 plies on the bottom surface. It opted that the lip would have a constant thickness distribution to maintain stiffness. The resulting morphed shapes for each subcase are presented in Fig. 3.36, with actuation

loads and nodal translations remaining similar to the limits stated in Tab. 3.6. This represented the final morphing skin design.

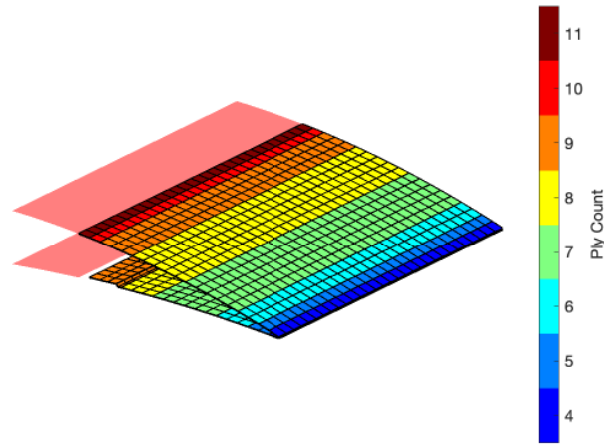
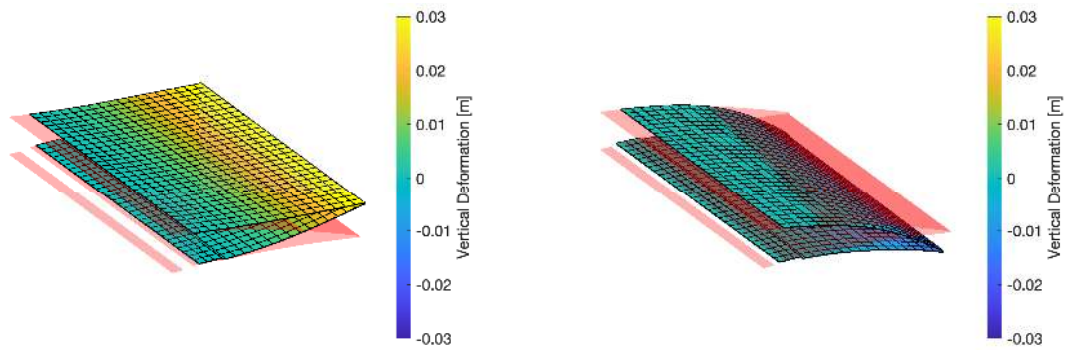
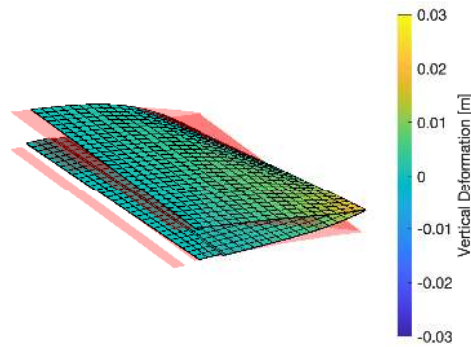


Figure 3.35: Laminate ply distribution on morphing trailing surface with offset lip



(a) Bend up

(b) Bend down



(c) Twist

Figure 3.36: Morphing deformations for all subcases with lip integrated

3.5.2. Actuation design

With the lamination design set, it was found that to achieve trailing edge tip deflections ranging from -20mm to 30mm required the chordwise translation at the free edge from -4.5mm to 6.5mm as shown in Fig. 3.37. The actuation force limits ranged from -60N to 60N .

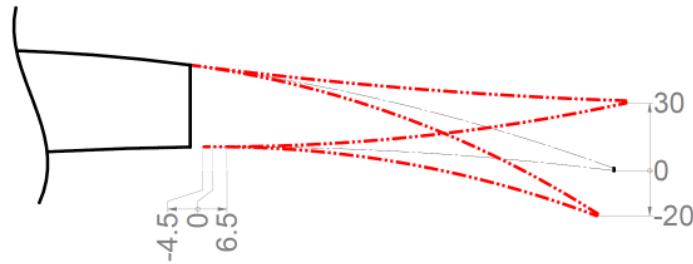


Figure 3.37: Translation required at the free edge to achieve full morphing range

With travel and load requirements set, the kinematic system could be finalized to actuate the sliding edge. The design work was based on the approximated system shown in Fig. 2.4.

To be able to use the smallest possible actuator, the approach to design was to minimize the torque arm to maximize force output from the actuator. The unwanted effect of shortening the arm was the increase to range of rotation needed to translate the sliding edge to the full range (θ_{act}). As discussed in Sec. 2.2.2, this range had to be kept within $\pm 40^\circ$. Therefore to achieve the desired chordwise travel at the sliding edge, the minimum torque arm had to be 10mm .

The minimum force of 60N was only achievable by three actuators in the considered VOLZ product range. These were the DA20-12-2515, DA22-12-2615, both offering forces up to 100N , and the DA22-12-4112 offering forces up to 150N . These servos are highlighted in the following plot, from which it can be seen that DA22-12-4112 provides faster responses than the other two. Given that the minimum arm considered in their peak force output was 12.5mm ($> 10\text{mm}$), it was decided that these servos be selected for actuation.

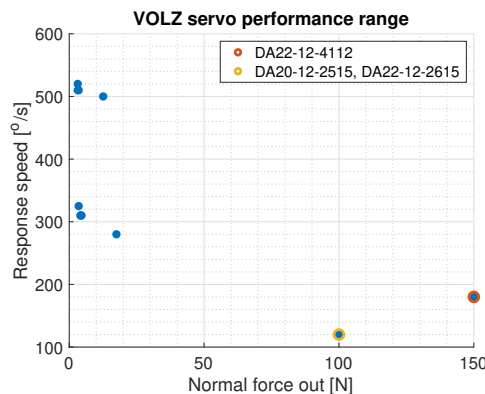


Figure 3.38: VOLZ servo product range, usable servos

3.5.3. Wing box and leading-edge laminate specification

The design of the leading edge and wing box did not require an aeroelastic analysis. A structural analysis with ABAQUS was deemed sufficient in evaluating a sufficiently stiff design. To benefit a smooth ply dropping sequence on the top surface, and prevent manufacturing errors, it was decided that the $\pm 45^\circ$ plies would also be used to construct the wingbox and leading edge section.

To design the structure, a highly conservative analysis approach was used: the wing was rigidly sup-

ported on one end, with the most adverse aerodynamic load applied on the other end, on the wingtip. The system was identical to a cantilevered beam loaded at the tip. All holes and cover panel segments were included in the structural model to evaluate the weakest possible structure. A graphical representation of this analysis model is shown in Fig. 3.39.



Figure 3.39: Wingbox and leading edge analysis

For the wing morphed in the bend down configuration, the C_L was evaluated to 2.2. At $30m/s$, with an air density, the total lift load generated on the wing would be $\sim 1000N$.

No specific optimization approach was used to select a suitable thickness, but rather a trial and approach method of altering thicknesses on the skin and spars was carried out. The laminate was defined using equivalent in-plane properties (Tab. 3.5) to be able to change the thicknesses of different regions quickly. The final selected design featured $1.65mm$ thicknesses all round (11 layers of fibre-glass). With this thickness, the wing tip deformed to $200mm$ as shown in Fig. 3.40. This was equivalent to $\approx 10\%$ of the span, considered sufficiently rigid. Peak strains were within material allowables as the wingbox was so rigid.

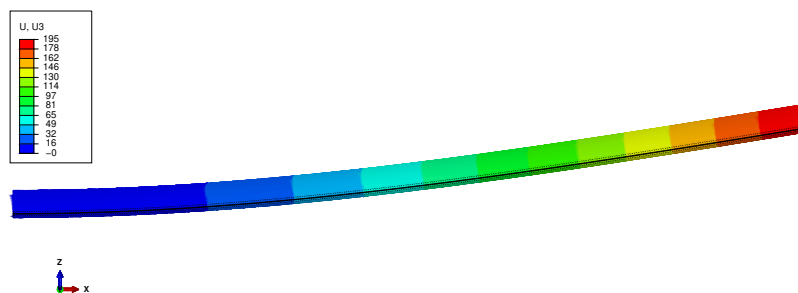


Figure 3.40: Wingbox and leading edge analysis results

4

Detailed Design for Manufacture

The work of the previous chapter presented a laminate structure which could be used and actuated with the selected VOLZ DA22 servo to meet the set functional requirements theoretically. The next stage in development was to provide a manufacturable system which can carry out these functions in the real world.

This included the detailed design of:

- the placement and componentry of the actuation system,
- the sliding surface support,
- the wing mounting boss allowing the wing to stand upright in the wind tunnel, and
- the provisions needed in the structure to route all sensor cables.

The design work carried out to produce the manufacturable Smart-X wing concept is presented in this chapter. Detailed drawings of the components designed here are presented in App. B.

4.1. Design and Placement of Actuation System

Firstly, all actuation components were positioned in the 2D airfoil plane, as shown in Fig. 4.1. The servo motor was located in the centre of the wing box, offset $10mm$ from the top wing surface to be able to design a mounting structure. The servos could be oriented in two directions which would change the chordwise placement of the servo arm. It was beneficial to place the arm further away from the sliding edge to increase the linkage arm length. This choice reduced the out of plane loadings, by minimizing the angle the linkage made with the chordwise axis. A configurable mounting structure was designed for the servo motors to have the capabilities to test the wing with different servos. This was made possible by integrating an adapter plate into the assembly which featured threaded mounting holes for the servos and additional fastening holes to mount the plate to a fixed mounting boss in the wing. This boss would be bonded to the wing surface. A 3D printable mounting boss was designed to reduce production expense. Threaded inserts could be potted in the printed mounting boss to provide rigid fastening points for the adapter plate.

To finalize the actuation kinematics, the location of the sliding surface pickup point (to which the linkage would connect to) had to be decided. The offset of this point from the plane of the sliding surface had to be minimized to reduce loading moments about the spanwise axis which promoted out of plane

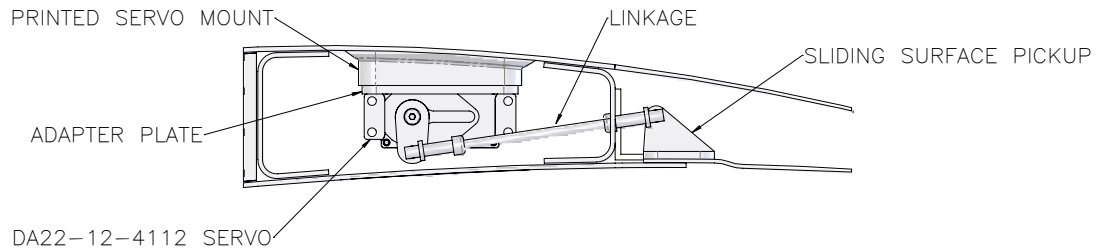


Figure 4.1: Chordwise arrangement of all mounting components for the actuation system

deformations of the bottom wing surface. Packaging limits constrained this as the linkage had to pass through holes in the spar and mounting fork. The offset had to be high enough that the linkage would not interfere with the surrounding structure in its travel range. To achieve this, the pickup point would have to be placed at the same height as the actuation rotation axis. 14mm diameter holes could be introduced in the rear spar, at the locations of the pickup points, to allow the linkage to be connected from the wing box to trailing edge.

The respective relationship between the actuator position and the chordwise translation of the sliding edge for the kinematic arrangement of all components is presented in Fig. 4.2. It shows a near linear relationship between angular position and chordwise translation.

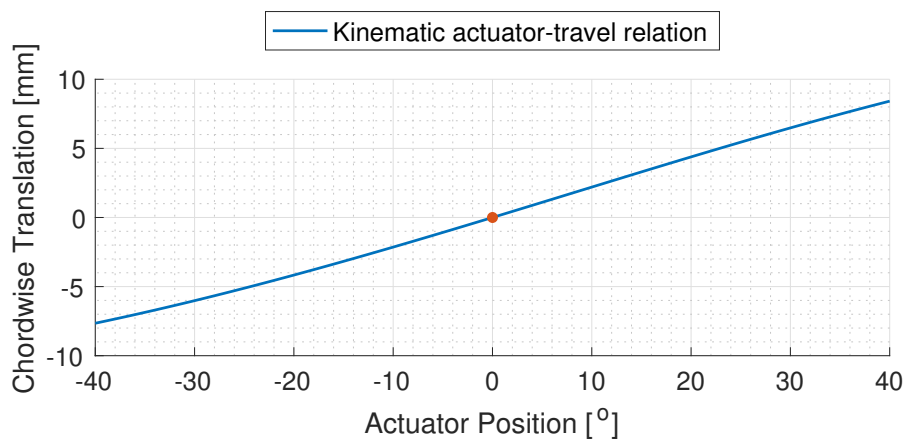


Figure 4.2: Kinematic relationship between actuator position and chordwise translation of sliding surface

An aluminium body (constructed from 7075-T6) was designed to be able to fasten a linkage pickup point at the prescribed location. The initial design intended that the structure would be bonded to the sliding surface; however, post-production testing on the Smart-X wing showed that this method of joining was prone to failure. It was later modified to be fastened to the sliding surface.

For ease of maintenance and assembly, the linkages were constructed with spring-loaded locking sleeves which could clip onto ball joints that are mounted on the servo arm and pickup point. The Sullivan 3mm Aluminium Ball Connectors that are shown in Fig. 4.3 were selected for this application. They were fastened onto 3mm threaded rods, cut to an appropriate size. A 3D printed jig was made to assemble all linkages to the designed model length.

Up to this point, the chordwise positioning of all components was set; the next stage was to distribute the actuation system across the span. The spanwise placement of actuators had to reflect the location



Figure 4.3: Sullivan 3mm aluminium ball connectors

of the actuation nodes in the analytical model, which was, in fact, at the two extremes of each module. This exact placement could not be carried out in production for two reasons: i) adjacent actuation points between modules would coincide which is not manufacturable, and ii) a shear area had to be provided between adjacent actuation points to integrate a flexible skin material.

At the time, the design of the elastomer system was not set. Therefore a conservative space was provided between adjacent actuation points of $30mm$. This space resulted in a $15mm$ gap that was measured between the bases of the sliding surface pickups.

This concluded the detailed design and placement of all actuation componentry.

4.2. Design of Sliding Surface Support

In the design of the sliding support, a key consideration on the tolerance between the surface and support had to be made. For the TRIC interface to operate efficiently, it was critical that sliding surface only translated in the chordwise direction. Therefore, a very tight tolerance was needed between the support and the surface; however, if the tolerance was too tight, the sliding friction may have been too high to cause stiction in the interface. It was decided that the standard manufacturing tolerance would be sufficient in restricting the motion to the chordwise direction. This would be enforced by placing the support directly over the sliding surface and bonding it in place at the rear spar. Any stiction could be overcome with a generous application of a lubrication compound.

To simplify the production process, an off the shelf aluminium equal angle channel of dimensions $25mm \times 25mm \times 2mm$ was selected to be used as the support. The support was placed in between the actuators for each module. The sliding surface was unsupported along the short span between adjacent actuation points as it was expected that the skin had sufficient bending stiffness that out of plane deflections would not occur. It was realized post-production that this was not the case, out-of-plane deflections of a significant order were present affecting the shapes of the morphing wing. This is further discussed in Sec. 7.

4.3. OJF Mounting Design and Integration

To be able to mount the wing in the OJF, a new mounting boss that could be bonded within the wing box had to be designed. A fork style design was conceptualized to package around the actuation componentry of the first wing module. The forks themselves would fit within the spars and be bonded to the surrounding laminate. On one of the forks, a cavity would need to be included to allow the linkage connected to the actuator closest to the wing root to pass through.

A conservative load case was established to be able to design a strong structure which would not fail during testing. It was designed to support a wing lift loading of $1000N$ (calculated previously), with a safety factor of 1.5. Within ABAQUS a FEM model was built. Two loads were applied at the tips of

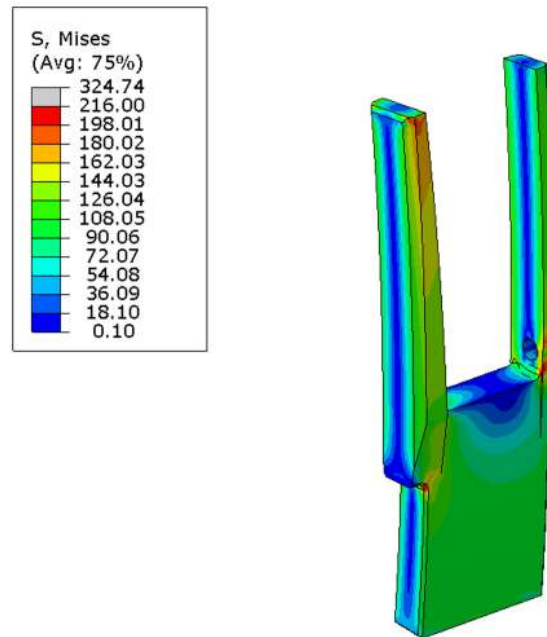


Figure 4.4: Analysis results from fork simulation, presented at 5x deformation

the fork, a $1000N$ shear load applied in the lift direction of the wing, and a moment, equivalent to the root bending moment of the wing structure, equated to 900 N.m by assuming the net lift is applied at the centre of the wingspan. A fixed boundary condition was applied at the base of the mounting boss. This model was a highly conservative approximation of how the system would be loaded; however, it was carried out this way to ensure any manufacturing errors affecting the bonding of forks to the spar would not influence the performance of the fork.

Peak stresses of 200MPa were witnessed on the analysis model. The final design was constructed from 7075-T6 aluminium, which had a yield stress of 430MPa resulting in a design safety factor greater than 2. It featured a tapered fork design for a gradual change in stiffness from tip to root to improve stress distribution near the root of the wing. The simulated results are shown in Fig. 4.4. The most critical design area proved to be at the cavity created for the linkage to pass through. To provide enough material near that region is what forced the offset of the pickup from the sliding plane to be increased.

4.4. Sensor Cable Routing

All cables required to power/communicate with the componentry had to be routed from their respective positions to the wing root. Cables could not transverse through the trailing edge as there was a risk that they would be cut when cutting the wing skin on the trailing edge. They could also not be routed through the wing box to ensure they did not obstruct any actuator motion. Therefore all sensors and component cables lying in the wing box/trailing edge had to be routed first through to the leading edge, and then to the root of the wing.

Each servo was powered with a cable of diameter 5mm and connection head of diameter 8mm . To route them to the leading edge, 16.5mm diameter holes were provided in the front spar, located at the centre of each module. Two cables could be passed through each of these holes, powering the servos of the respective modules.

The piezoelectric boundary layer transition sensors each had a 5mm diameter cable connected. In modules 2 and 5, where the sensors were located, $2 \times 16\text{mm}$ diameter holes were provided in the rear

spar and front spar to be able to route the sensor connection cables from trailing edge to the leading edge.

The fibre-optics occupied minimal space in the wing, given the size of each fibre. They had to be secured with cyanoacrylate in place, with a communication/power connector routed out to the base of the wing. They were routed along the top of the rear spar to reduce handling complications by trying to pass the connectors through holes. Given the fragility of the optics, a mounting attachment for the connectors at the root of the wing was designed and printed.

The piezoelectric bimorphs each came with a malleable *2mm* diameter cable bundle. Three of these bundles existed per module, except for the wing tip where four bundles existed. To be able to route these, *6mm* holes were provided in the rear spar to get the cables into the wing box. They could be routed to the leading edge through some of the other holes that were already available in the front spar for cable routing.

The LEDs strips were connected in series across the wing, and therefore the cables terminated directly at the leading edge. They did not need to cross between different regions of the wing.

5

Seamless Continuity Design and Integration

An extensive design and testing process had to be undertaken to be able to introduce a seamless continuity on the wing surface between adjacent, independent morphing surfaces. A structured design approach was once again taken, similar to that of the entire wing, by first establishing system functional requirements to meet. This led to an investigation to materials that could be used to achieve continuity, followed by conceptual design, analysis and testing to hone in on a viable design that could be integrated into the Smart-X wing.

5.1. Functional Requirements

To achieve independent distributed morphing, the following requirements had to be met by the continuity system. They captured performance and manufacturing requirements.

- All independent morphing modules had to be able to travel to the full desired morphing range, irrespective of the position of the neighbouring modules.
- The flexible continuity system had to be able to withstand applied pressure loadings.
- Conventional materials were to be used to implement this system.
- The system could be integrated onto the wing after the two halves of the wing were joined.

The above requirements promoted finding materials with the following properties, some of which are absorbed from the investigation by Kikuta [32] who determined desirable material properties generic to all morphing skins:

- Elastic and flexible to allow low force actuation,
- Tough,
- Can sustain pressure loads,
- High strain capability with high strain recovery rate,
- Environmental longevity and fatigue resistance,

- Abrasion and chemical resistant,
- Resistant to different weather conditions,
- Can be processed at room temperature.

5.2. Material Investigation

To determine which materials could be used for this application, the investigation started with seeking out which materials have been successfully used to build flexible morphing skins.

Thill et al. [48] completed an extensive review of current designs which have been trialed and conceptualized for morphing skins. They discuss the use of several different materials, including elastomers and auxetic materials, as well as various configurations of materials such as folding or corrugated skins. Alternatively, stiffness tailoring and multi-layered skins can also be implemented. Shape memory alloys and polymers are gaining traction as well, changing shape from temperature, although actuation and design of such mechanisms are complex. From their assessment, elastomers posed the best compromise for strength, manufacturability and low actuation forces.

Use of commercially available elastomers as morphing skins was investigated by Molinari et al. [38]. The author performed uni-axial, bi-axial strain and out-of-plane stiffness tests to evaluate thermoplastic polyurethanes, co-polyesters and woven materials. His assessment showed that no materials met all the criteria listed above. Materials able to strain could not carry high loads and vice versa, these were opposing properties for materials. The best performing solution was a Tecoflex™ compound, a thermoplastic polyurethane, with low tensile strength and modulus, but high elongation capacity. The limitation was its ability to sustain a pressure load (i.e. low out-of-plane stiffness). Production with Tecoflex™ was further limited to extrusions or injection mouldings, as they were thermoplastic polymers which need to be processed with high temperatures.

FishBAC were able to produce an EMC to address some of the limitations of elastomers, specifically low out-of-plane stiffness, toughness and the necking effect under elongation. EMC capitalize on the favourable properties of elastomers but use reinforcements such as fibres or cores to increase their out-of-plane stiffness and reduce the necking effect. The concept was introduced by Bubert et al. [22], using silicone face-sheets with fibre or honeycomb cores. The use of honeycomb cores was further investigated by Olympio and Gandhi [43]. A corrugated core was investigated for the FishBAC concept [25]. All these systems required a rather complex analysis to design cores suitable for the applications, and their manufacturing processes were not simple.

Steering towards the use of conventional materials in this application, being able to use off-the-shelf elastomers was favourable. Given the elastomer was only to be applied in small portions, methods to overcome insufficient out-of-plane strength could be investigated. The work of Kikuta [32], was able to suggest a thermoplastic polymer which could be used; however, its processability was difficult. Other forms of elastomers which exist abundantly include silicones, which are generally single component, moisture curing compounds. Several different types exist, and they have many uses including use as sealing compounds, or as moulds. Comparative to the thermoplastics, silicones can have similar properties, with generally slightly higher flexibilities. The limitations of silicones come with bonding ability: once cured, it is difficult to bond materials to it [1], which is why they are often used for moulds. The best bonding is achieved by directly curing silicone on surfaces to be bonded. This method works by producing an airtight bond layer which is similar to a vacuum seal. Similar to thermoplastic polymers, they also have low out of plane strength when cured as a thin film.

Even with their limitations, the best choice of materials for this application was silicones, given their ease of availability and processability. Conceptual designs would need to consider their downfalls and provide means to overcome them. Several suppliers could be used; however, recommendations from experienced staff, as well as the wing manufacturer, pointed towards using Wacker Elastosil compounds. They were one component moisture curing silicone rubbers that could be processed at room temperature. Within the Elastosil range, there were multiple compounds which could be selected,

which are summarized in Tab. 5.1. Reviewing the range seen in the table, the compounds had varying levels of hardness, strength and elongation capacities. The hardness of the compound could be taken as a measure of the elastic modulus. Within the literature, an equation to approximate elastic modulus from Shore A hardness (S) was found [9]:

$$E = e^{0.0235*S-0.6403}$$

Given the design had to be completed in a limited time frame, an extensive comparative assessment between compounds was not done. A compound with a suitable balance between strength and elasticity was selected based on recommendations from the wing manufacturer. This was the Wacker Elastosil E41 compound. In the event this particular compound was found to be too limited, other compounds could be investigated for use.

Table 5.1: Wacker Elastosil Silicone Properties [10]

Compound	Hardness Shore A	Elastic Modulus, E	Tensile Strength	Elongation at break	Tear Strength
Elastosil E4	16	0.8 MPa	1.5 MPa	600%	5 N/mm
Elastosil E10	25	1.0 MPa	6 MPa	300%	5 N/mm
Elastosil E14	36	1.2 MPa	3 MPa	300%	6 N/mm
Elastosil E41	40	1.4 MPa	6 MPa	350%	11.5 N/mm
Elastosil E43	30	1.1 MPa	4.5 MPa	500%	13 N/mm

5.3. Conceptual Design and Analysis

The integration of silicones into the wing skin could be approached in several ways, and therefore a platform to evaluate each of these concepts was needed. This began in the form of developing a computational analysis model, from which deformations and stresses of the material could be evaluated simultaneously with the increases in actuation loads to flex the system. The analysis model did not consider pressure loadings as it was challenging to integrate each concept into the aeroelastic simulation tool that was previously developed. A conservative design estimate on material thickness was used to ensure the system could withstand applied pressure loads.

The analysis model was built in ABAQUS as the author had a lot more experience in setting up non-linear structural models with elastomeric properties with this tool (in contrast to NASTRAN), speeding up setup and debugging steps. It was found that this simulation tool was still limited in providing the necessary design information as simulations were unable to converge. Several hypotheses towards convergence issues are discussed in the succeeding sections; however, these problems could not be overcome. The results of the simulation did provide a direction to continue design work with prototype testing.

5.3.1. Analysis model overview

The analysis model featured two independent modules connected at the wing box and leading edge. At the trailing morphing surface, continuity designs could be modelled using partitioning schemes. The wing section was rigidly fixed at the wing box on both sides of the span, with a sliding constraint imposed on the free edge of the lip.

Each module was actuated by displacing nodes which were coupled rigidly to surfaces representing the bond area of the actuation pickups. This method provided a more representative assessment of how the elastomer would shear between the actuation points. Modules were actuated antisymmetric with chordwise displacement at the nodes prescribed as $4mm$ on one module and $-4mm$ on the other module. A graphical representation of the actuation application method is depicted in Fig. 5.1.

The wing skin was modelled with linear shell elements, with material and thickness specifications per the outcomes of design work presented in Sec. 3.5. The silicone was modelled with linear shell

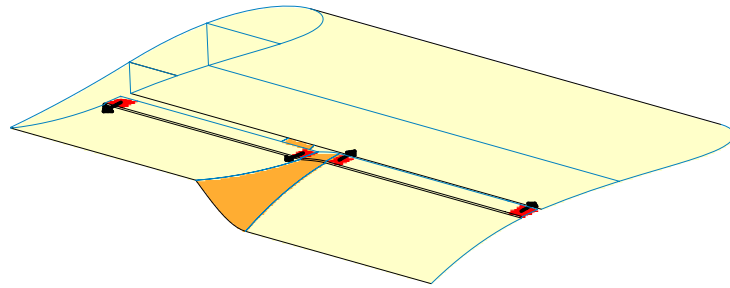


Figure 5.1: Graphical representation of actuation in the analysis model

elements with reduced integration formulation. This element type was recommended for modelling rubber-like materials which experience incompressibility and hence witness drastic changes in element thickness when they experience large in-plane stresses [36]. The system was analyzed with the non-linear structural solver to account for geometric non-linearities from large deformations of the structure and elastomer.

The silicone material specification was isotropic, with an elastic modulus of $1MPa$ and Poisson's ratio of 0.5. The thickness of the elastomer was set as $3mm$, which was a conservative approximation made to account for variability in controlling thickness during manufacturing.

Discontinuous module analysis

A discontinuous trailing edge morphing concept was analyzed for comparative assessments with designs employing a silicone connection. With this information, additions in actuation loads needed to stretch the silicone could be evaluated. An out-of-plane deformation plot with this analysis model is shown in Fig. 5.2. The system was able to achieve $\sim \pm 20mm$ tip deflections on the two respective modules, with actuation loads of $\sim \pm 40N$.

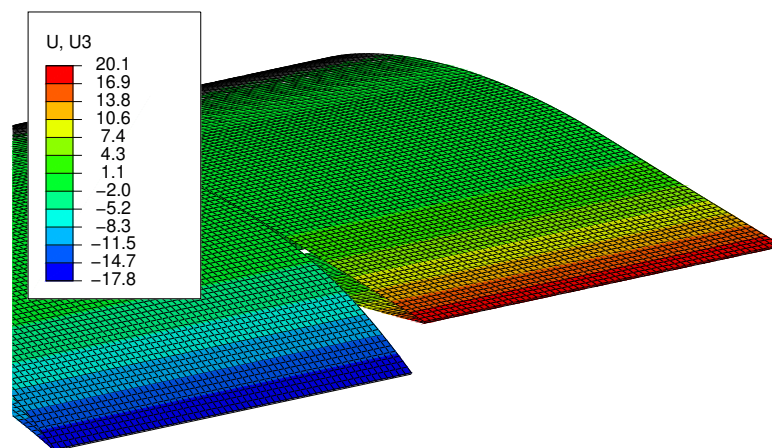


Figure 5.2: Tip deflections (mm) achieved with discontinuous modules

Concept 1

Given the major limitation of the silicone was the lack of out-of-plane stiffness, all designs always aimed to minimize the area between modules constructed from the silicone. The first concept, therefore, considered using slits in the wing skin which would be filled with the elastomer. This idea, depicted in Fig. 5.3, presents 4 cuts, 2mm wide (equivalent to blade thickness) filled with silicone. The design addressed the performance limits of the silicone and provided a simple to manufacture design. However, it was realized that the design was too stiff to shear between actuation patches.

Disappointingly, the results failed to converge beyond actuation limits of $\pm 1\text{mm}$. The results of the analysis are presented in Fig. 5.4. Careful assessment of the results showed very high strains in the elastomer near the actuation surfaces. With mesh refinements, simulations converged slightly more, although it was clear that substantial refinement would be required which would be very difficult to simulate in a reasonable timeframe.

Up to the point of convergence, the actuation loads were compared to the system without the elastomer connection. The comparison shown in Tab. 5.2 shows the loads were much higher with the elastomer connection, as a result of the high shearing experienced between the actuation patches. With several failed attempts of altering model setup and solving conditions to benefit convergence, this design was discarded in analysis. From this, the next design approach was to increase the flexibility of the system near the actuation patches in shear. The simplest method to do so was to increase the area filled by the elastomer.

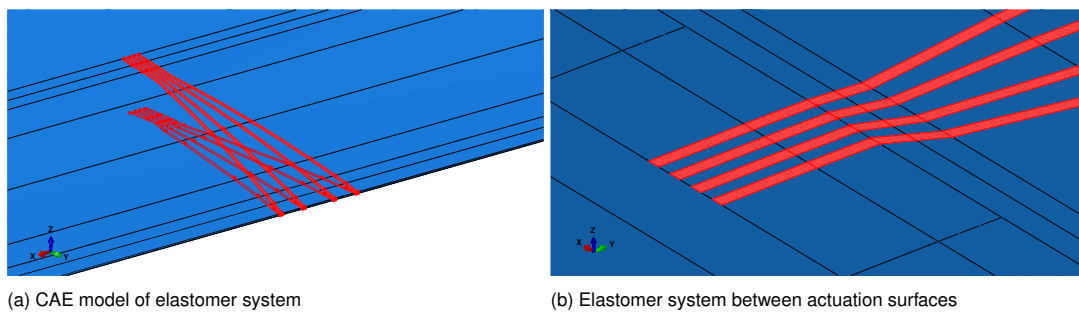


Figure 5.3: Patterned silicone elastomer system trialled in first analysis

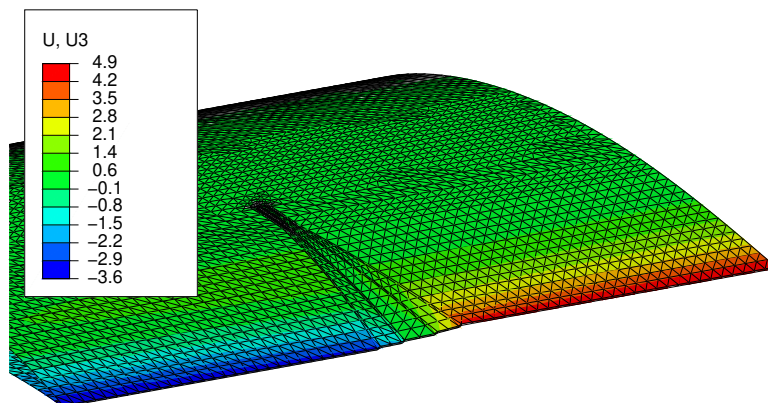


Figure 5.4: Tip deflections [mm] achieved with first elastomer system concept

Concept 2

For the second iteration, a revised design where the majority of the volume was filled with an elastomer was trialled. A fibre-glass skin segment in between was still included, as shown in Fig. 5.5. The results once again failed to converge, however simulations did get further in solving, now almost to 50% of the desired travel range. The results in Fig. 5.6 shows the converged results. The force scaling with and without the elastomer was approximately 5x as high, which was still considered too high. Therefore, keeping with the trend, for the next concept, the entire fibre-glass skin between modules was removed only to feature a silicone segment.

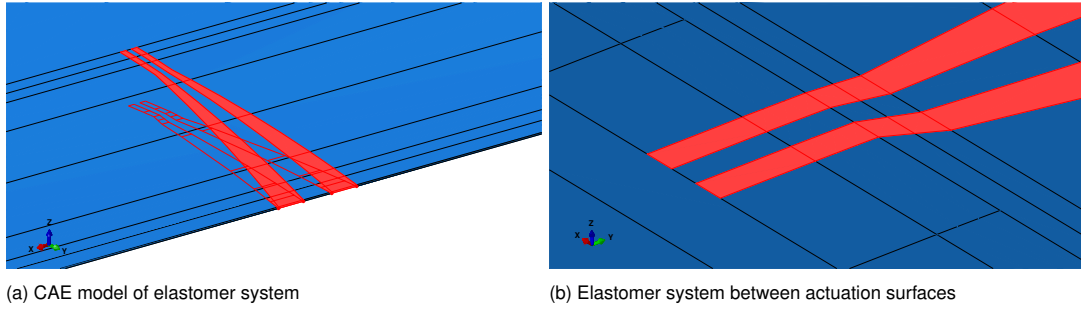


Figure 5.5: Elastomer system trialled in the second concept, with increase in volume of silicone

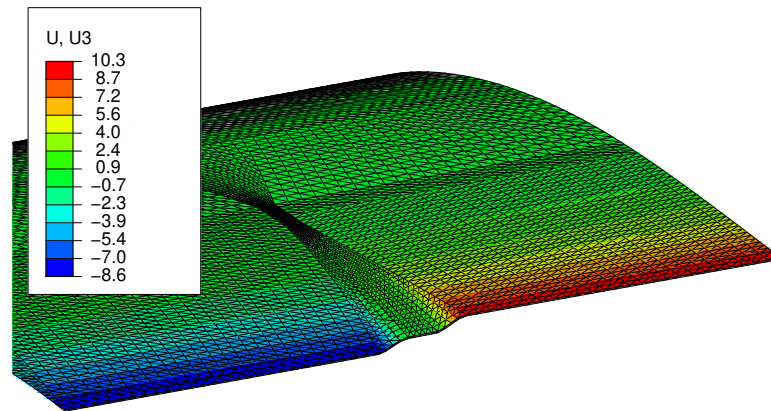


Figure 5.6: Tip deflections (mm) achieved with second elastomer system concept

Concept 3

In the final concept, the entire bridge was filled with a 3mm thick silicone skin, as shown in Fig. 5.7. The simulation once again came closer to completing, however, failed at 75% travel. The load scaling was once again reduced to 3x given the system was more flexible. The results of the last converged point are shown in Fig. 5.8.

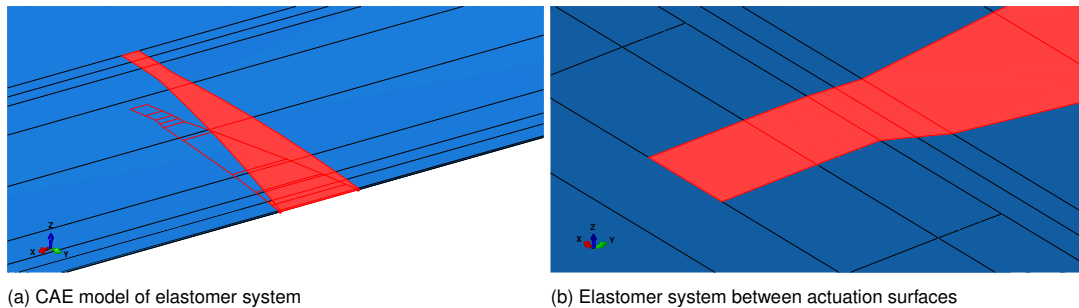


Figure 5.7: Elastomer system implemented in final concept, with the bridge completely filled with silicone

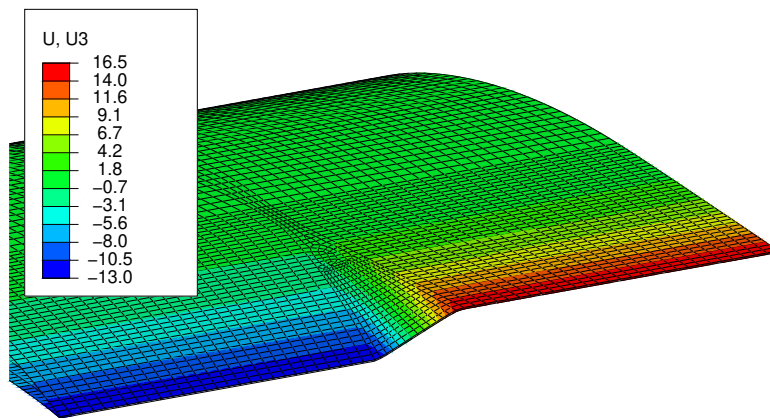


Figure 5.8: Tip deflections (*mm*) achieved with second elastomer system concept

Simulation conclusions

Table 5.2: Summary of actuator travel and loads measured in simulating different elastomer connection concepts

Concept	Travel	Load (w/ elast)	Load (w/o elast)	Scaling
1	$\pm 1mm$	$\sim \pm 245N$	$\sim \pm 15N$	$\sim 16x$
2	$\pm 2.1mm$	$\sim \pm 130N$	$\sim \pm 25N$	$\sim 5x$
3	$\pm 3.2mm$	$\sim \pm 115N$	$\sim \pm 35N$	$\sim 3x$

No concepts were able to converge to the full travel range prescribed in simulation. One of the primary reasons for this was likely due to a higher mesh resolution required in the shear area between adjacent actuation patches to properly model the amount of straining to occur in near the area. Carrying out this refinement, however, resulted in computationally expensive simulation setups which were not completed within a reasonable timeframe.

To bypass these issues in the simulation environment, prototype testing was sought out instead, which would provide more concrete solutions.

It was evident that the actuation loads were significantly higher in the simulation environment to flex the silicone. This could have been problematic as the actuator has a limited force capacity, up to 150N.

Given the skin design work carried out on a single module showed that a peak actuation load of $60N$ was required to actuate all morphing configurations, load scaling with the elastomer system included could not exceed beyond $\sim 1.5 - 2x$. Simulated concepts in this respect did not present a viable design; however, the conditions were to be tested in the real world to see how they compare to simulation.

5.3.2. Prototype testing

A printable test setup was designed, as shown in Fig. 5.9. The setup was physically representative of the intermediate morphing section between two adjacent wing modules, inclusive of the actuation kinematic geometry. Two of the selected DA22 actuators could actuate each apparent module. The spar structure was stiffened for this application to prevent unwarranted deformations.

Each test sample was constructed from the rapid prototyping of PLA plastic in the general shape of the NACA 6510 trailing edge shape. The thickness of the skin was maintained as $2mm$ as the focus of this assessment was purely towards finding a suitable means of integrating the silicone rather than accurately recreating deformed shapes. All samples were appropriately cut and then filled with silicone and left to cure. Post curing, printed sliding edge pickups were glued with cyanoacrylate (superglue) in their respective positions, and additional lip thickeners were glued to stiffen the sliding surface. Finally, the sample was placed in the test rig, and pushrods were attached between the actuators and the pickups.

A generic morphing sequence was programmed to deform the apparent modules to their most extreme positions in the opposing directions to visualize the behaviour of the silicone.

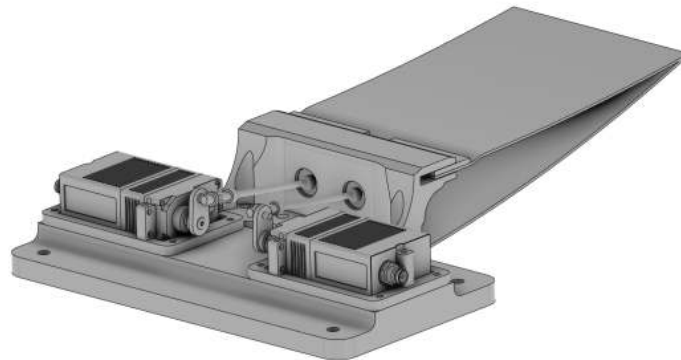


Figure 5.9: Printable test rig assembly to test different elastomer connection methods

From initial tests, several structural limitations were realized in the test setup. The spar structure was compliant and would deform when the test samples were deformed antisymmetric. Additionally, the lip surface region, which was unsupported at the actuation points, would show out of plane deformations under actuation. Both motions were caused by loads being redistributed when it was too difficult to shear the silicone. Taking the path of least resistance, beyond a certain travel range, all the actuation load would be redirected into deforming the structure rather than the elastomer. No direct means to address these issues were realized in time, but they were considered when selecting a viable design for this application.

Prototype concept 1

The first prototype attempted to test the first simulated concept with thinly sliced cuts in the wing skin, which were filled with the elastomer as shown in Fig. 5.10. When tested, the pickups immediately debonded as the shear stiffness of the skin/silicone pattern was too high. It confirmed the expectations of the simulation that the actuation loads required to shear this type of connection would be too high.

Moving with the trends of the simulation, the next samples only featured a silicone connection between modules.

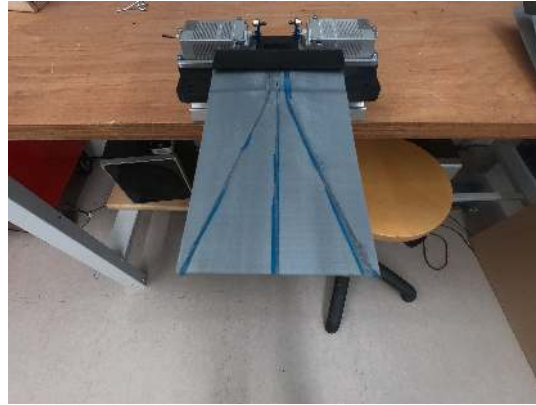
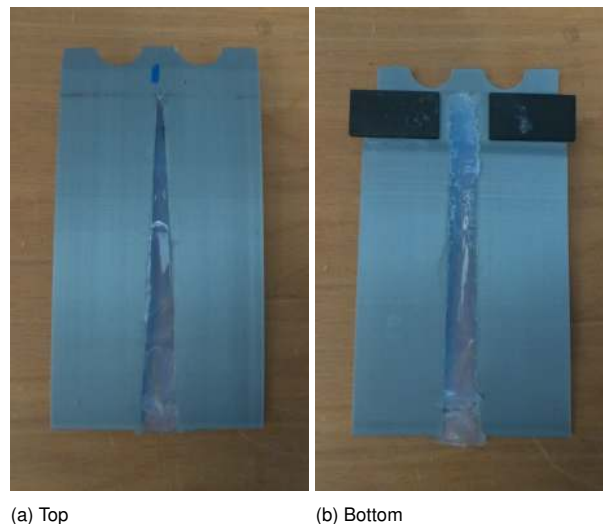


Figure 5.10: Test sample which thin silicone joints trialed to achieve continuity

Prototype concept 2

With the TRIC design, majority of the shearing in the silicone was occurring the bottom side of the wing. In contrast, on the top surface, the elastomer was primarily being stretched in tension. Therefore, it was decided that on the bottom surface, a larger patch of silicone would be implemented by using two parallel cuts in the wing skin, from the start of the lip to the trailing edge. On the top side, a reduced area could be used, by cutting the wing skin in a triangular fashion, as shown in Fig. 5.11.



(a) Top

(b) Bottom

Figure 5.11: Second design prototype, with a 15mm wide shear area provided on the bottom surface terminating to a 3mm tip on the top surface

A 15mm wide segment of silicone was trialed on this concept on the bottom surface, which on the top surface terminated to a 3mm wide tip. The system showed significant improvements over the first trial, being able to accommodate the full antisymmetric servo motion. There was however a design

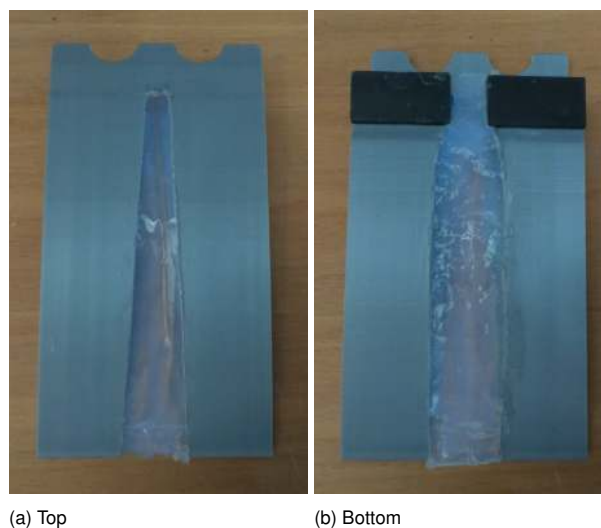
limitation where, at a certain point the load redistributed to bulging the wing skin rather than shearing the silicone. Therefore the travel range of the trailing edge tip was compromised. This bulging effect is highlighted in Fig. 5.12. To prolong load distribution, the system had to be easier to shear, which could be made possible with a wider silicone segment used to connect the modules.



Figure 5.12: Bulging effect seen on the second prototype during anti-symmetric actuation

Prototype concept 3

For the final prototype, a 30mm wide silicone segment was used on the bottom surface, which terminated to a 10mm wide tip on the top surface. Between pickups, a 15mm gap was still maintained as shown in Fig. 5.13. The revised design performed much better, but some bulging still occurred on the lower skin (Fig. 5.14). Given tip deflections at the trailing edge were much higher (confirmed from visual observation (Fig. 5.15)), this design was considered viable for implementation on the final wing. A segment any wider than this would be difficult to produce hence the width of the silicone was capped to 30mm .



(a) Top

(b) Bottom

Figure 5.13: Third design prototype, featuring a 30mm wide silicone connection on the bottom surface, terminating to a 10mm wide tip on the top surface



Figure 5.14: Bulging effect still prominent on the third concept, however to a lesser effect



Figure 5.15: Peak anti-symmetric tip deflections captured on the final prototype

5.3.3. Integration

To fill such a wide cutout with silicone, moulds to support the wet system during curing would be necessary. Therefore, a printable mould pair for the top and bottom surfaces was designed. These could be lined with a release film and attached to the outside surface of the wing, to provide a surface to support the silicone. External moulds had to be used to achieve a good surface finish on the exposed surfaces of the wing.

With a mould system designed, manufacturing and integration steps could be carried out. All work was done with the lip exposed. The first steps were to cut the fibre-glass skin to outline the geometry of the silicone system. Markings were done precisely, and an oscillating cutting tool was used to carry out the cutting work. Cut edges could be cleaned up with a file and sandpaper. This process is shown in Fig. 5.16.

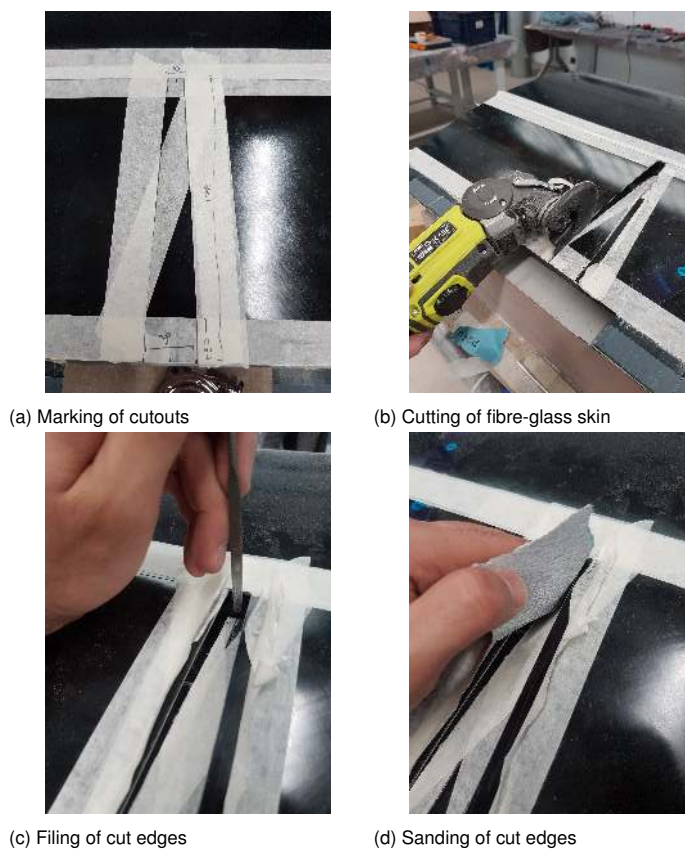


Figure 5.16: Preparations of wing skin to be able to connect adjacent modules with silicone

The next stages involved curing the silicone, but that had to be done with two curing steps for the two wing sides to prevent the silicone from dripping. It was decided that the first side to be cured will be the top side, given silicone could be easily fed from the underside of the wing, which was cut and so exposed to the top area. The silicone supporting moulds were lined with Teflon tape and attached to the wing skin with a thin double-sided tape. The wing was then oriented such that the region of silicone application was near flat, relative to the ground plane, to prevent pooling of the silicone during curing. The silicone was applied generously and scraped to fill the entire top surface gap. Curing occurred over 24 hours. The wet silicone system curing on the top wing surface is shown in Fig. 5.17.

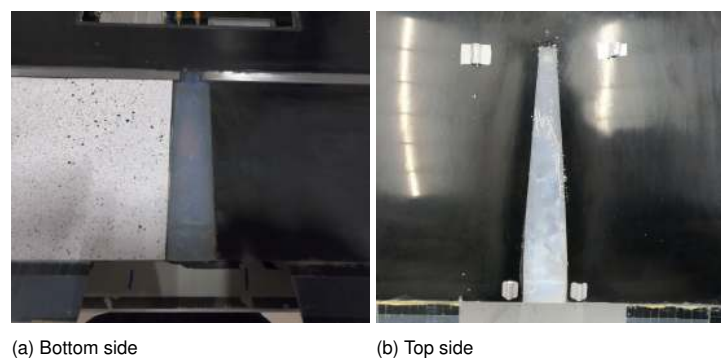


Figure 5.17: Application of the silicone on top wing surface through the underside of the wing

The next stage was to apply the silicone on the lower wing surface. This would be done by first attaching the silicone support moulds to the underside of the wing, with double-sided tape, and then flipping the wing to lay parallel to the ground plane. To feed the silicone in the gap, the exposed lip would be propped up with spacers, and silicone would be fed through an injection tube which was long enough to reach the trailing edge wingtip. With a custom scraper, the silicone would be spread across the gap and then left to cure.

This method of integration was rather complex but necessary at the time. The result was successful; however, controllability of the elastomer thickness was highly inconsistent. A generous amount of silicone was used to ensure the system would not tear. This approach was taken as it was understood that the system could be replaced at a later date if the design was not sufficient.

The resulting system is shown in Fig. 5.18. Within Sec: 7, the deformation behaviour of the morphing wing with and without the influence of the silicone shearing is discussed.



(a) Bottom side

(b) Top side

Figure 5.18: Elastomer system cured on final wing shown for the connection between two wing modules

6

Surrogate Model Development

The smart control of the wing had to be based off a surrogate model that was able to provide an accurate approximation of lift, moment and drag distribution across the morphing wing for given actuator inputs and aerodynamic state (i.e. angle-of-attack and wind speed). Model development for the scope of this thesis was capped to developing a surrogate model predicting lift for a single module and completing preliminary verification with mechanical testing (discussed in the following chapter). The previously developed aeroelastic analysis tool served as the foundation for this work.

6.1. Model Requirements

It was beneficial for the controller to know that for given actuator positions, free-stream velocity (V_∞) and angle-of-attack, how would the lift coefficient change, relative to the baseline conditions.

The previous statement could be summarized into a list of surrogate model requirements, specifically the inputs and outputs of the model:

Inputs:

- Actuator 1 Angular Position
- Actuator 2 Angular Position
- Free-stream velocity (V_∞)
- Angle-of-Attack (angle-of-attack)

Outputs:

- ΔC_L , relative to baseline

6.2. Model Simplifications and Assumptions

The basis of this model was adapted from the aeroelastic model developed for design. No modifications were made to the simplifications and assumptions used for the design model. However, this compromised the prediction of stall, and drop in lift due to boundary layer separation without the use of a viscous flow model.

This information would, of course, be critical to the controller; however, time did not permit inclusions of these considerations into the surrogate model. These additions would be recommended as future development work, further discussed in Sec. 8.

6.3. Surrogate Model Assembly

The assembly of the surrogate model began with understanding how the various input parameters individually influenced the output ΔC_L . This included an evaluation of how free-stream velocity V_∞ and angle-of-attack could alter the equilibrium shape of the wing due to increased loadings at higher values. Modifications to the equilibrium shape could potentially introduce non-linearities in lift predictions which had to be considered. Additionally, it had to be evaluated how variation in actuator inputs influence the change in lift. The findings from these assessments are discussed in the following subsections.

6.3.1. Influence of free-stream velocity on C_L

The first simulations completed were directed towards understanding the influence of free-stream velocity on the change in the deformed equilibrium shape of the wing. This assessment was completed to determine how higher dynamic pressures altered C_L .

The assessment was completed with the most adverse loading conditions: the airfoil bent down with actuation inputs set as $-5mm$ and angle-of-attack set at 5° . Free-stream velocity was swept from $10m/s$ to $30m/s$ in increments of $5m/s$ to evaluate ΔC_L .

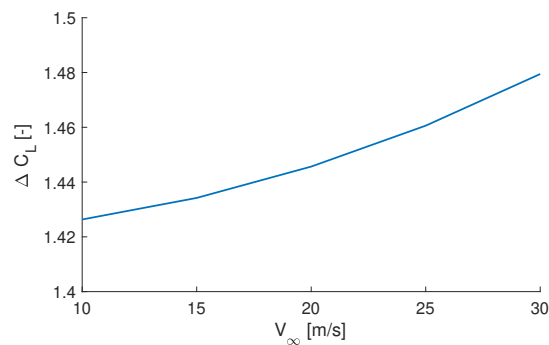


Figure 6.1: Influence of free-stream velocity on ΔC_L

The results in Fig. 6.1 show that with increasing velocity, the global change in ΔC_L was negligible. Between $10m/s$ and $30m/s$, the lift increment only changed by 0.05. Therefore it could be assumed that velocity would not substantially influence C_L for it to be warranted as an input. The degree of the change in C_L as a result of velocity would, however, be influenced with flow viscosity due to changes in pressure distributions especially at high angle-of-attack. However, as stated previously, these are considerations to be made in the future.

6.3.2. Influence of angle-of-attack on C_L

Generally for all airfoils, the relationship between C_L and angle-of-attack is linear at low angles of attack. Similar was likely to be true for this application. There was a risk that a changing angle-of-attack would alter the equilibrium shape of the wing with an increase in the pressure load, but unlikely to occur given it was already verified that the change in velocity did not substantially alter the wing shape.

This hypothesis was verified by conducting an analysis once again on an airfoil morphed in all three configurations (peak bending up/down and twist) at a velocity of $30m/s$. The angle-of-attack was swept from -12° to 5° in increments 1° . The results from the analysis are shown in Fig. 6.2. It presents a

linear relationship between C_L and angle-of-attack. The gradient for these configurations was constant at ~ 0.12 with only a varying offset at 0° angle-of-attack. It was expected that with a viscous analysis, lift drop-off points at sufficiently high angle-of-attack would have been captured by the assessment.

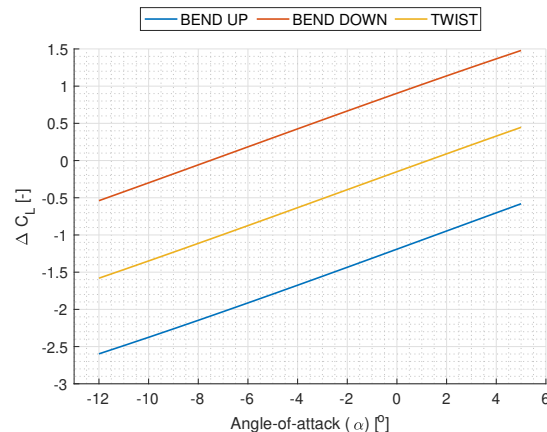


Figure 6.2: Influence of α on ΔC_L

Given the equilibrium shape was not altering with varying angle-of-attack, the surrogate model could be more simply built by performing a static aeroelastic simulation of the wing at 0° angle-of-attack to evaluate the deformed shape of the wing (at given actuator inputs), and then parsing this shape into the aerodynamic solver to calculate the change in C_L for varying angle-of-attack.

6.3.3. Influence of actuator inputs on C_L

The final assessment needed to assemble the surrogate model was how actuator inputs influenced C_L . The simplest way to carry out this assessment was to vary actuator inputs one at a time and run through every possible combination to create a map of input to C_L .

This process had to be automated given the sheer number of possibilities in combination of actuation inputs. To do so, a BDF writing function was developed to generate new simulation files for each combination. The assessment was carried out at $30m/s$ at 0° angle-of-attack. Each actuator input could be varied from $-5mm$ to $7mm$ in increments of $1mm$. Reversed combinations were not simulated, as the results would be the same, i.e. if actuator 1 translates $1mm$ and actuator 2 translates $5mm$, the lift coefficient calculated would be the same as if these were inverted. The number of simulations was reduced with this approach.

The results of the assessment showed that the change in C_L was a linear function of the actuation inputs as shown by the planar mapping of C_L in Fig. 6.3.

It was realized that all input parameters had a linear relationship with the output parameters. Given variations in results from structural linearity and non-linearity was already proven to be minimal in the design work, any changes in the linear behaviour of this model would be realized by extending the aerodynamic solver with viscous flow conditions.

6.3.4. Full model assembly

All the pieces of the puzzle could now be brought together to build the surrogate model of a single wing module. From the previous assessment of deformed shapes with actuator input, these shapes could be parsed through the aerodynamic solver to evaluate the change in C_L with changing angle-of-attack.

The results of this assessment for angle-of-attack ranging from -12° to 3° , in 4° increments shown in Fig. 6.4 shows how a constant offset is present between each planar surface. This shows that the

gradient in the lift curve for a given shape is maintained at 0.12 for changing angle-of-attack. The only variation in the lift curve function for a certain shape is offset at 0° angle-of-attack.

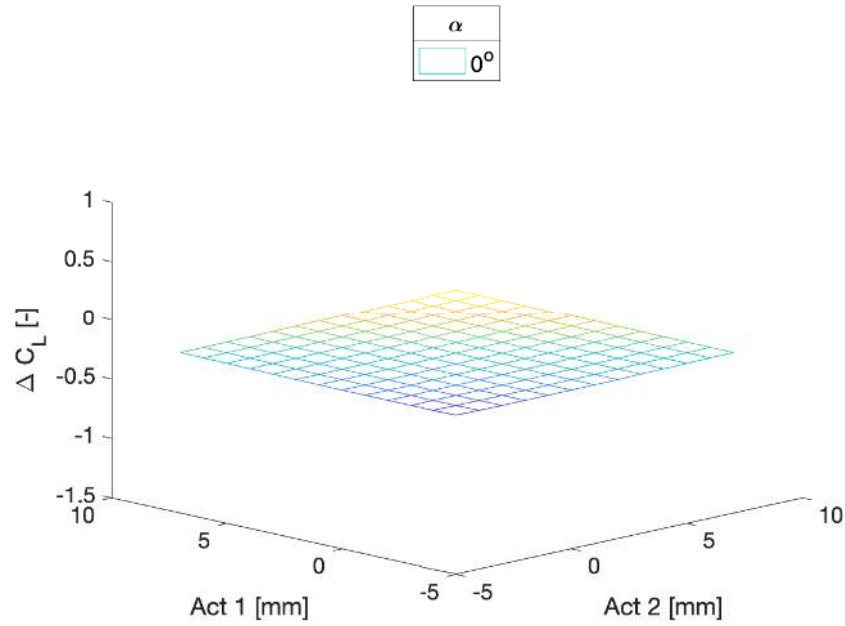


Figure 6.3: Influence of actuation inputs on ΔC_L

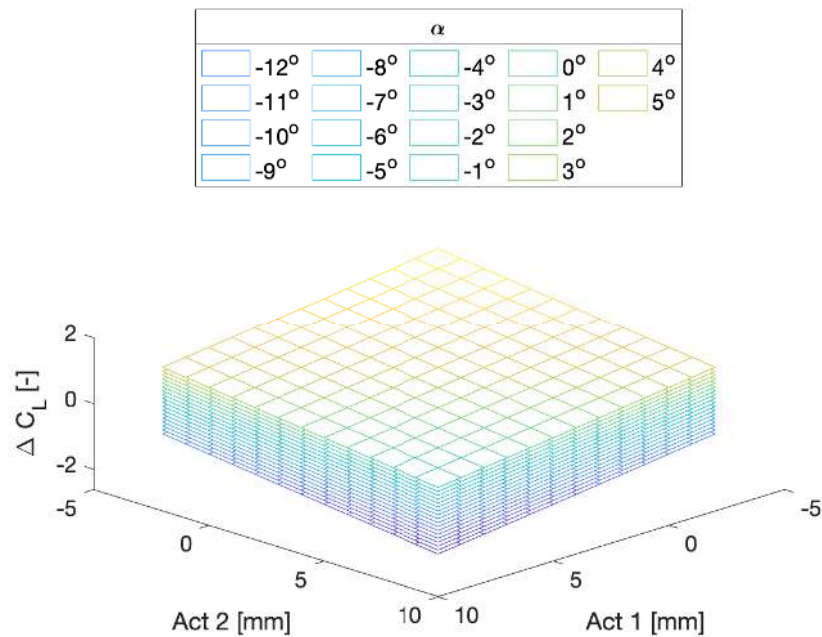


Figure 6.4: Single module surrogate model presenting a lift increment (ΔC_L) relative to baseline for given actuation inputs and angles-of-attack

7

Analysis validation

The theoretical model of the wing module behaviour discussed in the previous chapter had to be verified with real-world testing to determine the accuracy in predictions of the model. This work started with using DIC to measure deformations of the structure under actuation inputs.

7.1. Structural Testing with DIC

A DIC test setup was built to assess morphing shape changes on the top and bottom wing surfaces of the two trailing edge modules near the root of the wing. The test setup of the system whilst measuring the deformations on the bottom surface is shown in Fig. 7.1. The two sides were analyzed separately, given enough equipment was not available for simultaneous assessment of both sides.

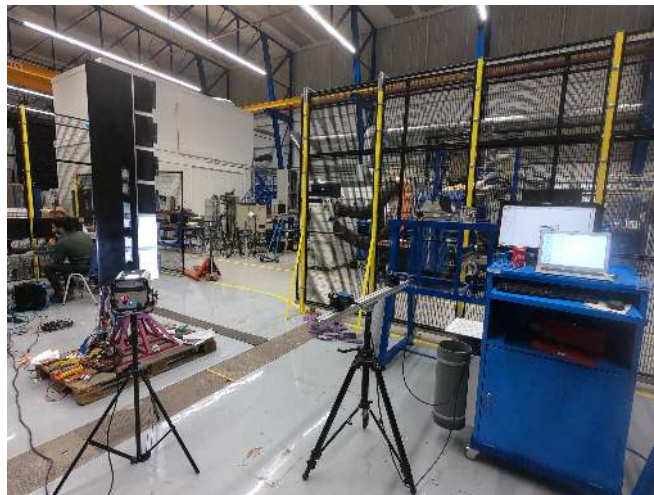


Figure 7.1: DIC test setup to measure deformations on bottom wing surface

The speckle pattern needed to analyze shape changes was implemented by speckling a matte white, adhesive film which could be cut to shape and adhered onto the surface of the wing. This approach was used to protect the surface finish of the wing and was considered allowable as strains were not being measured from the system, only change in deformations under actuation.

Several tests were completed to build a good understanding of how the wing deforms, with and without the stretching of the elastomer in between. These are listed below. To have a rich data set, all tests

were carried out by positioning the actuators from 0° to $\pm 25^\circ$ in increments of $\pm 5^\circ$, with direction altered respectively of the test. Actuation was limited to $\pm 25^\circ$ due to manufacturing tolerances affecting higher actuation inputs.

- **Module 1 and 2, Bend down:** Both modules were deflected down from 0° to -25° , to determine the structural shape of module 1 without the influence of the silicone in the bend down configuration.
- **Module 1 and 2, Bend up:** Both modules were deflected up from 0° to 25° , to determine the structural shape of module 1 without the influence of the silicone in the bend up configuration.
- **Module 1 Bend down, Module 2 Bend up:** Module 1 was deflected down from 0° to -25° , with module 2 deflected up from 0° to 25° , to determine the structural shape of module 1 with the influence of silicone being overly stretched in the bend down configuration.
- **Module 1 Bend up, Module 2 Bend down:** Module 1 was deflected up from 0° to 25° , with module 2 deflected down from 0° to -25° , to determine the structural shape of module 1 with the influence of silicone being overly stretched in the bend up configuration.

The respective areas where deformations on the top and bottom surfaces were measured are shown in Fig. 7.2. On the lower surface, the trailing 130mm portion of the wing was analyzed, aft of the lip. The measurement area covered the entire span of the module up to the start of the elastomer. On the top surface, the trailing 190mm portion of the wing was analyzed. The measurement area spanned 200mm and was centred on the module. The location of the elastomer relative to the measurement areas is highlighted in the figure.

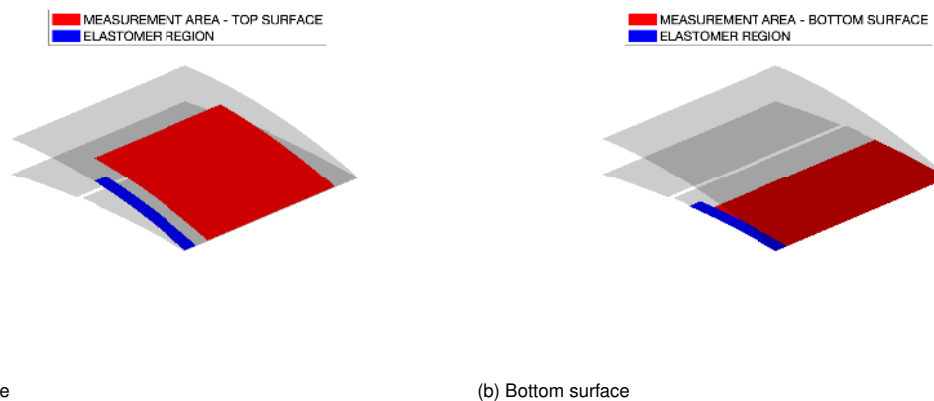


Figure 7.2: Areas measured on the top and bottom surfaces in DIC testing

7.2. Calibration of Results

The results output from the post-processing software was in an arbitrary global reference frame determined by the location and orientation of the cameras used. To be able to perform comparative analyses against theoretical models, the results had to be transformed into a usable reference frame.

Calibration of results was completed by orienting the trailing edge of the measured surfaces in line with the spanwise axis of the analytical model. A rotation about this axis was then performed to ensure the undeformed surfaces measured aligned with the undeformed analysis model.

Verification of the calibration method on the top surface was conducted by comparing the trailing edge tip deflections measured from DIC testing against deflections measured with a Vernier height gauge. The latter test was conducted by the orienting the wing in the horizontal position and offsetting it from

the ground plane. The bend up and bend down morphing sequences were employed to measure the deformations of the morphing surface on this test setup, with trailing edge tip height measured for each actuation increment at the extremity of the wing module as shown in Fig. 7.3.



Figure 7.3: Rudimentary test setup to measure trailing edge tip deflections with a Vernier scale height gauge

A comparative presentation of the tip deflections measured from DIC and the more rudimentary mechanical measurements is presented in Fig. 7.4. The trailing edge tip deflections calculated for the DIC dataset equates to the average of tip deflections measured across of the span of the measurement area. In the bend down motion, all measurements showed a strong correlation, suggesting a predictable behaviour in morphing. However, with the bend up configuration, the two trials conducted for DIC testing and the results measured with the Vernier showed more deviations in results. Although trends were similar, magnitudes varied. These results verified that the calibration approach was appropriate, but also suggested that there was a certain limitation in the repeatability in behaviour during the bend up motion warranting further investigation.

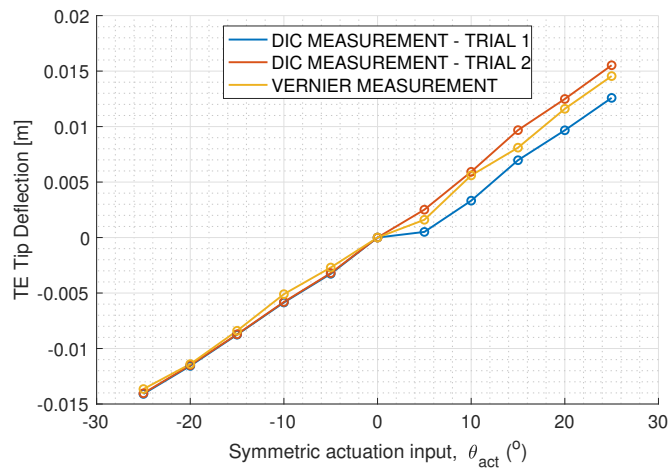


Figure 7.4: Comparison of results between DIC measurements and calliper measurements

7.3. Results and Discussions of DIC Testing

7.3.1. Assessment of repeatability

For several reasons, an assessment on the repeatability of the wing to assume the same deformed shapes had to be carried out. This was important to understand as the top, and bottom surfaces were analyzed separately. To be able to draw conclusions relating the influence of the bottom surface on the deformations at the top for the same testing configuration and actuation position, it had to be known that the wing assumed the same shape when testing the bottom surface and the top surface.

Two assessments of repeatability were conducted. As all tests started at the unloaded, baseline condition, with the airfoil assuming the NACA 6510 shape, the first assessment checked repeatability of the baseline shape. For each trial, and test configuration, the baseline shape measured was compared to that of the ideal NACA 6510 airfoil. In Fig. 7.5, this comparison is shown for the baseline shapes assumed before starting the bend down and bend up tests for the first and second trials. A contour plot is used to visualize the out-of-plane deviations of the measured surface relative to the baseline airfoil, where positive deviation represents the surface bulging out of the page. The limits of the colour scale are constant across the plots for each surface for ease of comparability. The deviations between trials at the baseline position for most cases follow very similar trends and magnitudes. An outlier is measured for the second trial of the bend down subcase for the bottom surface and the second trial of the bend up subcase for the top surface where deviations are an order of magnitude higher, however, this is circumstantial. Similar plots were generated for all baseline shapes measured at the beginning of all tests, and they are presented in App. C. A careful review of these results would show that in general, the same shape is assumed for the baseline position.

The second assessment on repeatability evaluated how deformations compare for the same tests, between trials. In the following figures comparisons of out of plane deformations on the top and bottom surfaces for the peak bend up and bend down conditions are shown. The colour scale of the contours represent the out of plane deflection measured, and they are set to the same limits for each surface to be able to compare results visibly. The contour maps in Fig. 7.6 show very similar trends and magnitudes of deformations for the bend up and bend down cases, bringing confidence to the repeatability of the results. Further comparisons were also carried out on other test conditions, the results of which are presented in App. C. For all tests, repeatability of deformations to a suitable degree was confirmed.

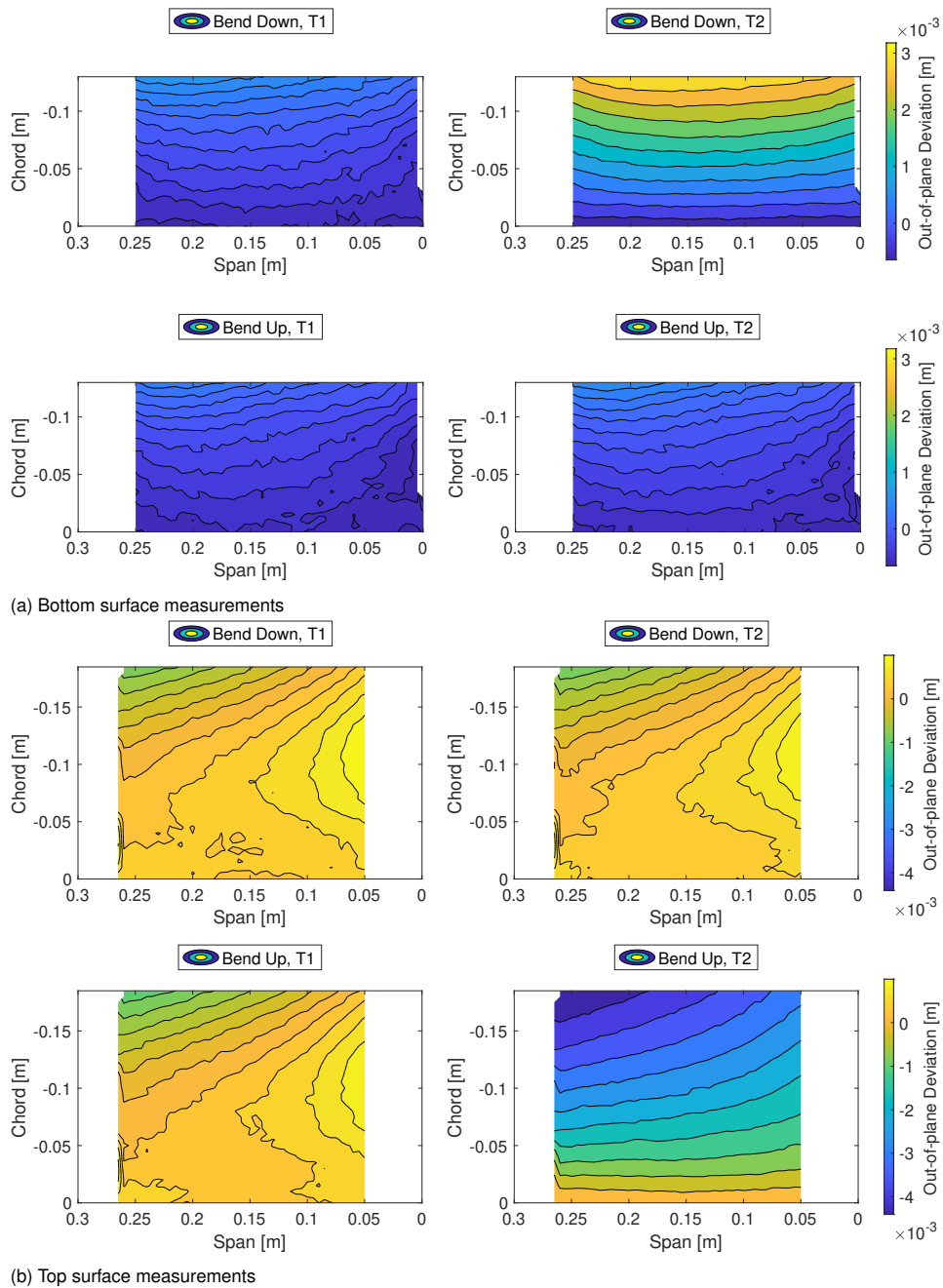


Figure 7.5: Comparison of baseline measured surfaces with baseline NACA 6510 airfoil to judge for repeatability

7.3.2. Evaluation of baseline shape

In the previous subsection, deviations of the measured surfaces from the ideal NACA 6510 airfoil were presented. Looking at the results before starting the first bend up test, several observations could be made. These deviations are presented in Fig. 7.7, alongside a 2D view of the measured surface.

Firstly, the order of magnitude of deviations seen is in the order of $10^{-4}m$ (i.e. 0.1mm), which is considered negligible. However, it can be observed that on the top surface, there is an out of plane deviation at the top right corner. This is thought to be caused by a lack of restraint on this free edge, as a comparison to the otherside where the skin is connected to neighbouring morphing module. Without reinforcement, the wing skin has more degrees of freedom to take on a shape of least resistance. This

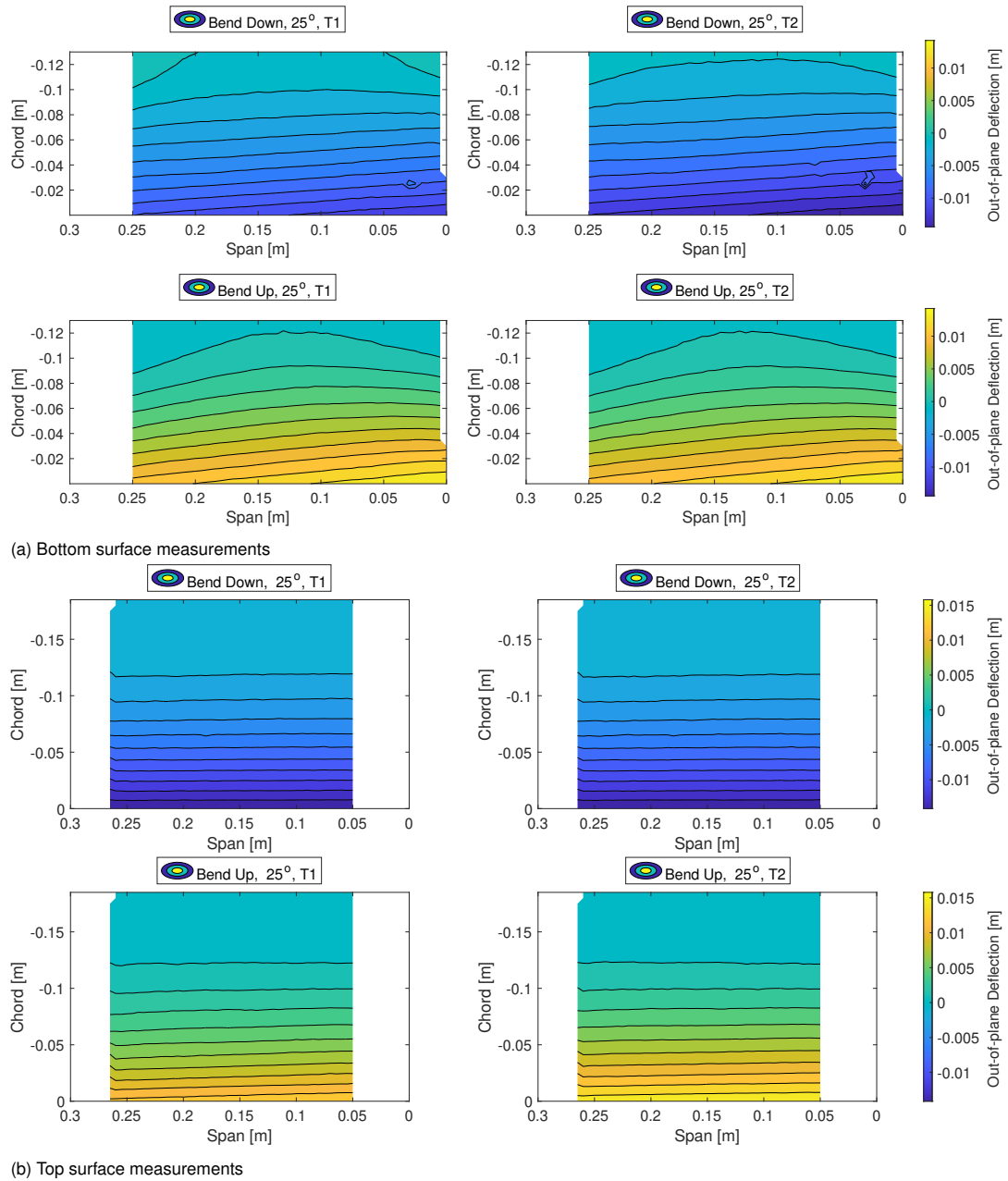


Figure 7.6: Comparison of out-of-plane deflections measured on top and bottom surfaces between trials for peak bend up, bend down tests

shape may be influenced by a slight deviation in the actuation position from theoretical zero, as a result of assembly/manufacturing errors.

Similarly, on the bottom surface, the contour map shows a slight bulge outwards near the left actuator. This asymmetric deviation about the centre-line of the module is thought to be caused by the slightly different boundary conditions between the sides of the modules.

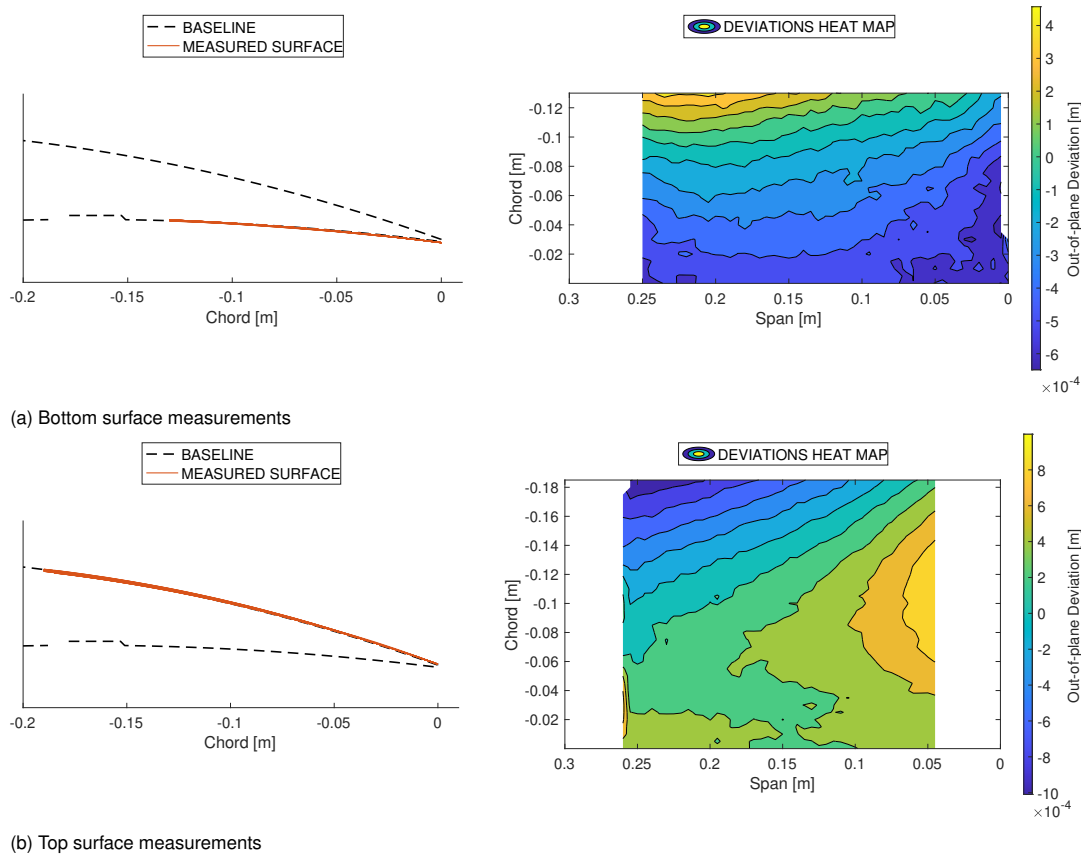


Figure 7.7: Baseline measurements carried out before starting the first bend up test shown in comparison to the ideal NACA 6510 airfoil shape

7.3.3. Evaluation of camber morphing

With the first two tests, the camber morphing behaviour of an individual wing module could be evaluated. In these tests, the influence of straining the elastomer was not considered.

The first assessment carried out with this data set was a comparison of trailing edge tip deflections between simulated and measured results, which is shown in Fig. 7.8. The tip deflection for measured results was evaluated by averaging the tip displacement measured along the span of the top surface. The contour plot is shown in Fig. 7.6 of the measured deflections on the top surface (from the first bend up trial, with 25° actuation) showed that the tip deflection on the top surface was near-constant across the span of the module. Therefore calculating the average deflection across the span would be a representative evaluation on the behaviour of the trailing edge tip. The trailing edge deflection was evaluated from simulated results in a similar fashion; however, actuation inputs were prescribed by calculating a chordwise translation of the actuation nodes based on the actuator position and theoretical kinematic model of the actuation system.

The figure shows that the theoretical model substantially overestimates the tip deflection. To understand why a comparative contour plot on the top and bottom surfaces for the peak bend up conditions were produced and are shown in Fig. 7.9. When analyzing the out of plane deflections between the simulated and measured conditions, the relative displacement gradient in the chordwise direction was very similar, although a with a noticeable bulging effect occurring near the actuation areas on the bottom surface. Given the gradient was near similar between theoretical and measured results, the bulging effect was not considered the primary influencer in the reduced tip deflections. A revised plot was created, but now with chordwise translation mapped, which is shown in Fig. 7.10.

This plot was very revealing. It showed that on the lower surface, the chordwise translation at the

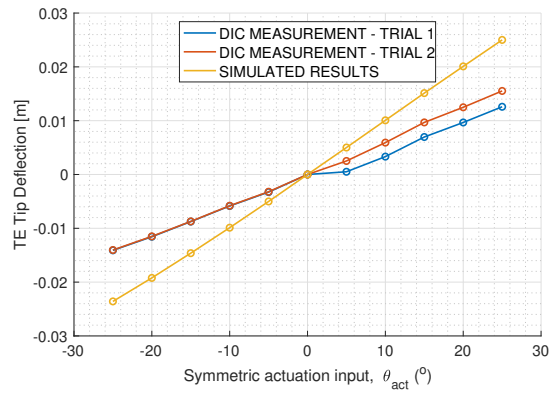


Figure 7.8: Comparison in tip deflections measured and simulated

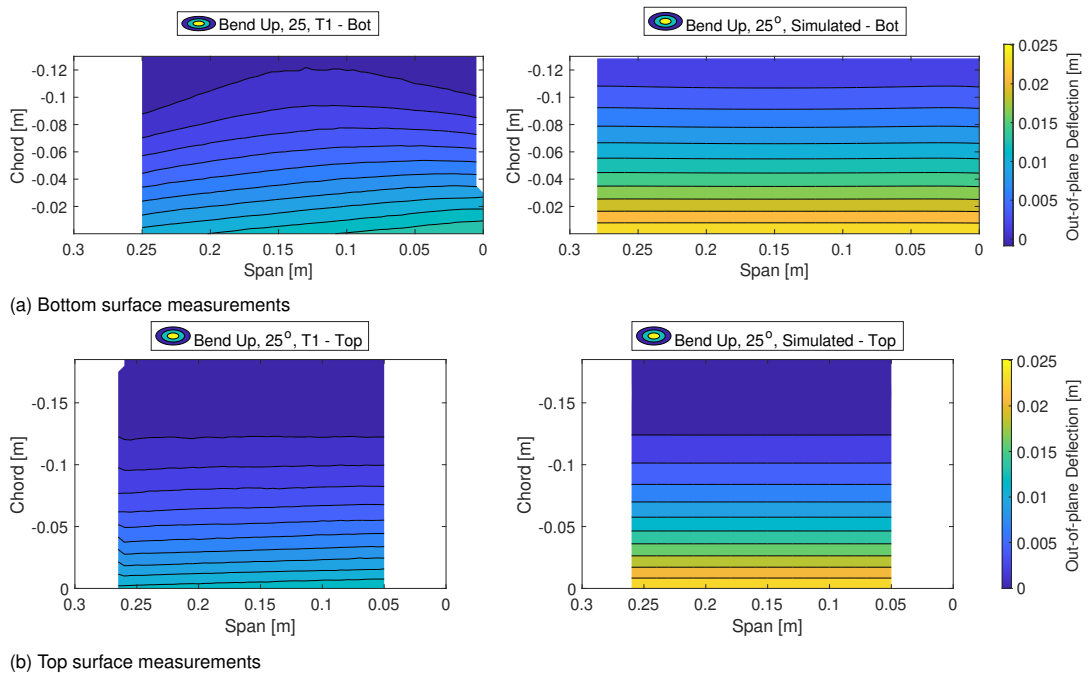


Figure 7.9: Out-of-plane deflections compared between simulated and measured conditions for the peak bend up actuation of 25°

actuators was much lower than predicted by the kinematic model. To understand why, the bending motion was carried out with the behaviour of the pickups analyzed visually from the side of the wing. It was noticed that when actuating, a portion of the actuation motion contributed purely to pivoting the sliding surface as a pose to producing a chordwise translation of the sliding surface. This behaviour was also captured in the elastomeric test setup and is shown in Fig. 7.11. In addition to reduced translation, it was clear that even with symmetric inputs, the sliding surface translated asymmetric due to the boundary conditions present at the span extremities of the module (i.e. one side was free, and the other was not). This system behaviour was considered a significant design limitation. Addressing this issue formulates a segment of future work discussed in Sec. 8.

It was clear that the theoretical kinematic model was not representative of real-world behaviour. Although, revised actuation inputs could be provided in the analytical models to reduce tip deflections to compare deformations to real-world results.

With revised actuation inputs, contour plots showing out-of-plane deflections for simulated models could be compared to real-world results, which is shown in Fig. 7.12 for the peak bend up subcase.

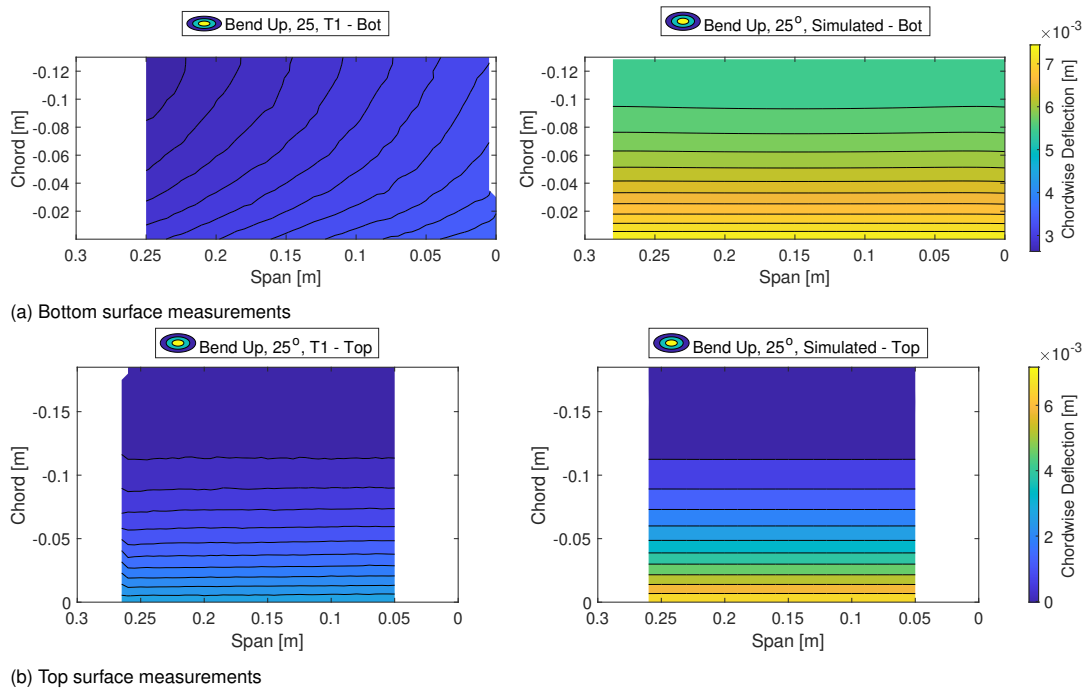


Figure 7.10: Chordwise deflections compared between simulated and measured conditions for the peak bend up actuation of 25°



Figure 7.11: Pivoting effect witnessed under actuation, shown in the elastomer test setup during a camber morphing configuration

From the plots, it was evident that the trends in the results were very similar, as were the magnitude of the deformations, especially on the top surface. On the lower surface it was evident that near actuation points, the measured results showed a localized out of plane deflection which was resulting from the lack of spanwise bending stiffness. For the bend down subcase, this localized deflection caused the skin to bulge outwards in between actuation inputs. In contrast, for the bend up subcase, this localized deflection caused the skin to bulge inwards in the same area. The pivoting effect likely caused this effect during loading exaggerated by the lack of support directly above the actuation pickups.

A 2D profile assessment between the measured and simulated results was conducted for the bend up and down cases, with measured results showing the behaviour at the extremity of the span. This is presented in Fig. 7.13. For the bend up cases, observation of the top surface shows a strong correlation between the simulated and measured results. However, for the bottom surface, there is a bulging effect witnessed at the extremities. This effect is likely caused by the pivoting effect in the bend up case redistributing the load to force the skin to bulge. Observations from the bend down

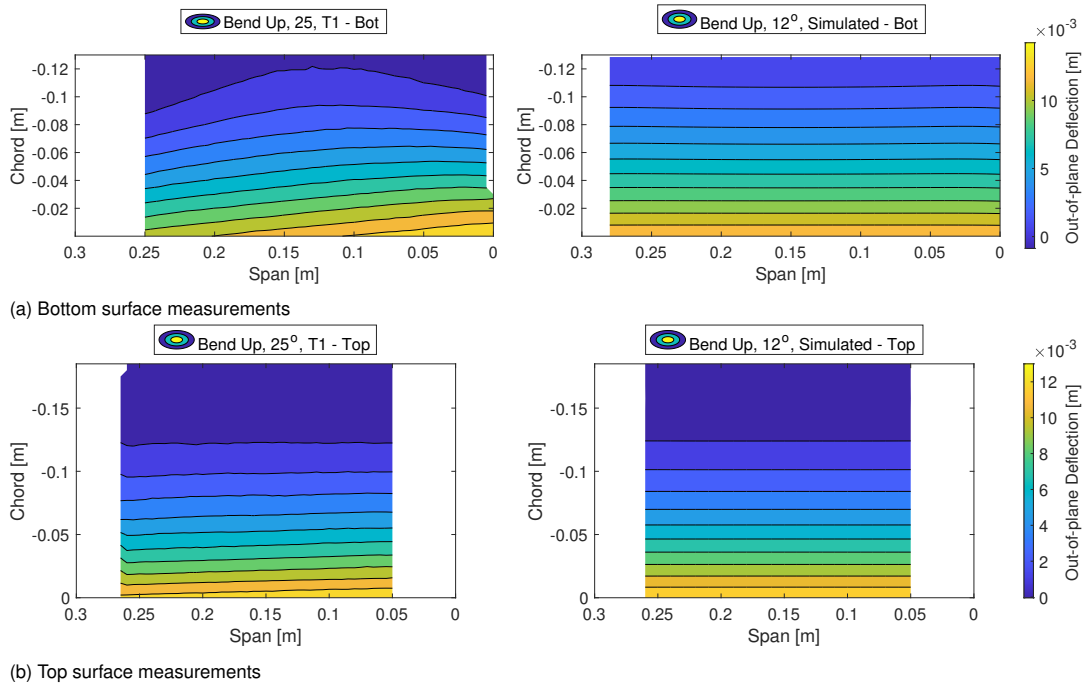


Figure 7.12: comparison of measured surfaces with reduced simulation actuation inputs

assessment showed strong correlations on the top and bottom surfaces. The out-of-plane bulging did not come into play as the lower surface was loaded in tension when bending down. The slight offset on the bottom surface is explainable by slight deviations in calibration; however, the equivalency seen in curvature shows a good correlation.

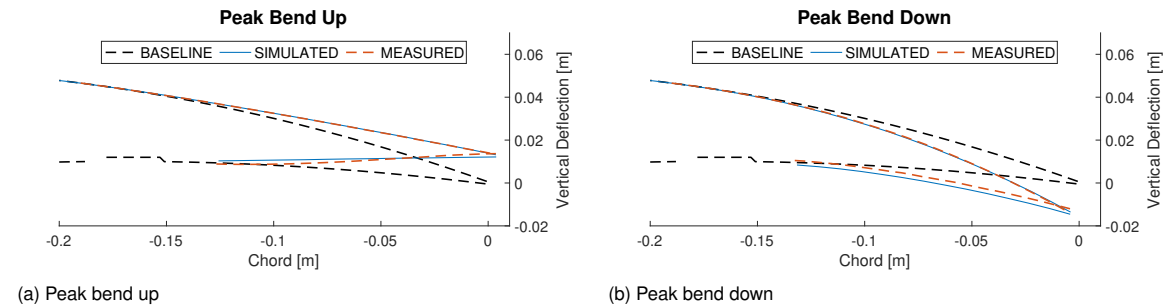


Figure 7.13: Comparison in 2D deformations between measured and simulated conditions for matching trailing edge tip deflections

7.3.4. Evaluation of camber morphing with the influence of silicone

To understand the influence of the silicone shearing on the behaviour of the modules, antisymmetric actuation inputs were enforced between two adjacent modules. Results were analyzed on the root module.

A revised plot showing measured tip deflections with antisymmetric module actuation inputs was very revealing. This is shown in Fig. 7.14 which presented that when the module would try to bend up, the trailing edge tip reach would be severely compromised. This reduction in magnitude also occurs when bending down, although to a much lesser degree.

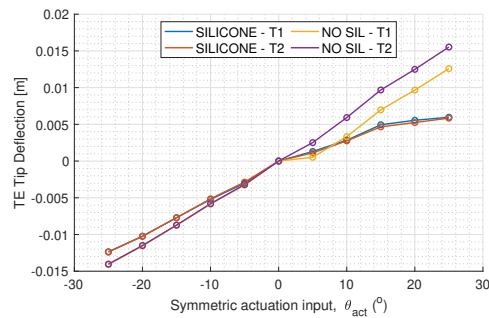


Figure 7.14: Influence of silicone on measured trailing edge tip deflections

The out-of-plane deflection contour assessment for the peak bend up and bend down measurements from the first trial on the top surface are shown in Fig. 7.15. Whereas bend down actuation on the first module shows comparable results, bend up deformations are significantly reduced. Evaluating the out-of-plane deflections on the bottom surface reveals a substantial bulging out effect, as seen in Fig. 7.16. This bulging effect is created by the significant shearing occurring in the silicone, forcing the skin to bulge outwards, rather than continue shearing the silicone, taking the path of least resistance. This was a failure of the continuity system to meet the desired functional requirements enabling complete independent morphing to the full desired range. Within Sec. 8, recommendations to address this limitation are discussed.

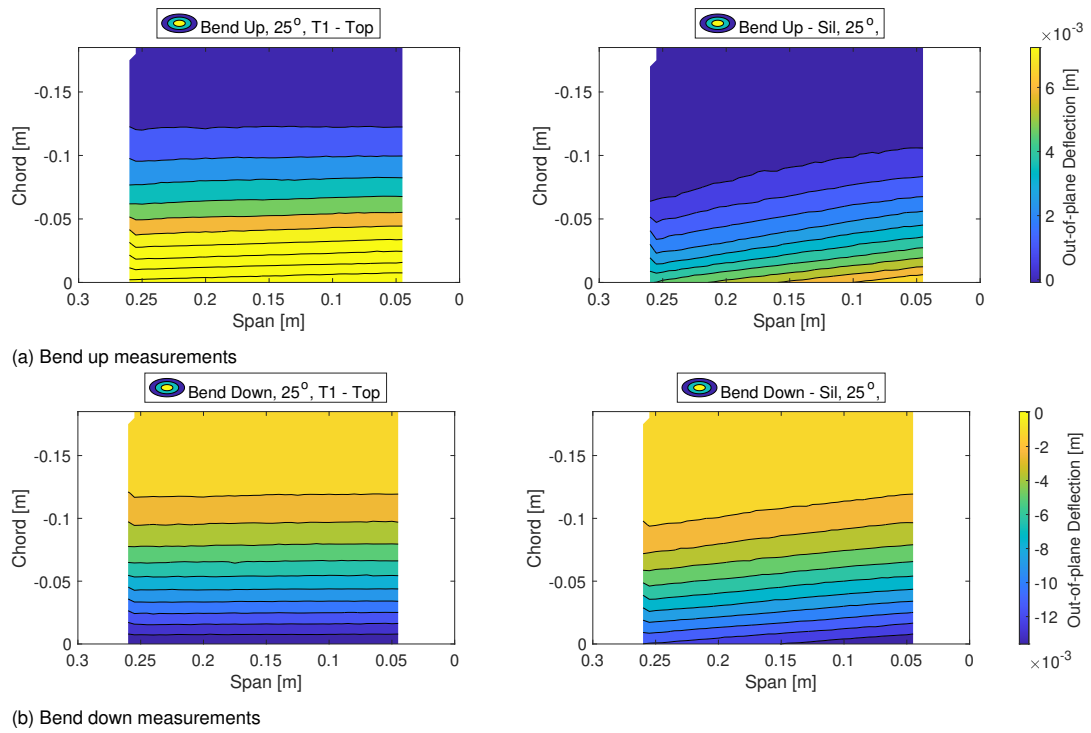


Figure 7.15: Out-of-plane deflections compared for peak bending cases with and without silicone shearing on the top surface

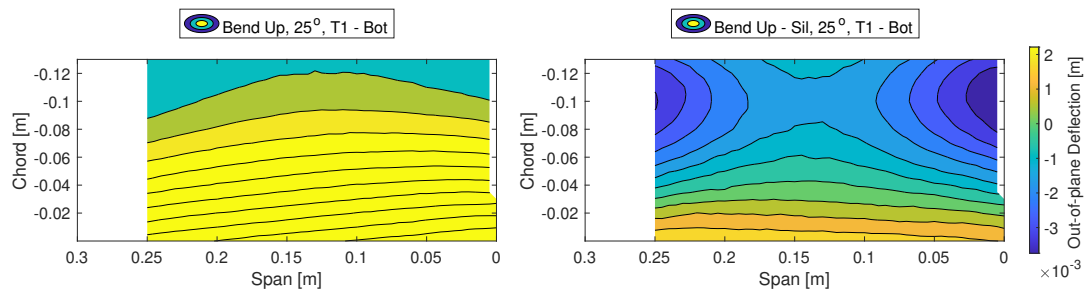


Figure 7.16: Out-of-plane deflections compared for the peak bend up case with/without silicone shearing on the bottom surface

8

Recommendations

Throughout the process of design, analysis and testing of the Smart-X wing, several key lessons have been learnt, and design limitations have been found. These learnings formulate the recommendations for future work.

Three key areas of focus are suggested to improve the method of design, increase the accuracy of the surrogate model and be able to achieve seamless continuity between adjacent modules with full independent morphing functionality:

- The analysis framework for design has to increase in complexity to include considerations for loading moments and tolerances in the gap between the sliding surface and sliding support.
- The surrogate model needs to be extended to include viscous flow effects and 3D flow distribution for a more accurate prediction of lift, drag and moment predictions on the wing to benefit smart control.
- More investigation into flexible skin system needs to be carried out to address the restrictions witnessed in morphing during system shear.

To be able to address these areas, the following recommendations are made.

Inclusions of loading moments can be built in the analysis model by using multi-point constraints to couple an actuation node (that is offset from the sliding surface) to a distributed load patch. Upon actuation of this node, an equivalent loading moment would be induced simultaneously. To consider the induced deformations from the loading moment on the sliding surface, the degree-of-freedom relating to the rotation about the spanwise axis for the sliding edge would need to be made free. A revised target shape preventing out-of-plane bulging under actuation could then be enforced on the bottom surface to present designs with potentially thicker layups that do not bulge under bend up actuation, even with a loading moment.

To extend viscous effects into the surrogate model would require calibration of the viscous model to find the right modelling parameters able to capture flow separation and stall conditions accurately. Calibrations could be carried out with experimental datasets acquired from the wind tunnel testing regime. Beyond that, the use of ELLT to capture 3D flow effects would present a more accurate means of approximating the flow over the wing, taking into account vortices created at the wing tip and associated downwash on the drag and lift distribution influencing the drag coefficient and root bending moment of the wing. With this information, the smart controller would benefit in alleviating loads and optimizing the wing shape for increases in L/D .

Finally, the silicone system implemented represented a good direction in achieving seamless continuity; however, much more investigations need to be carried out addressing manufacturability and structural performance. The analysis model should be evaluated and improved to overcome the convergence issues seen to be able to design a system that can meet the functional requirements in the analysis environment. These models can be further evaluated with prototype testing on a more rigid testing jig, and representative skin samples to have a more affluent design foundation to move forward with implementation on the next iteration of the wing. Beyond improving the analysis and test systems, further investigation into materials that can be used for this application should be considered. The silicone system used in this application was operational; however, its use is not scaleable for larger wings as it is very weak in supporting out-of-plane pressure loads. Employing EMC may be a path forward to achieve more flexible skin designs that can sustain pressure loads, but this would result in a more challenging to manufacture concept. It comes to show that this work can formulate a thesis topic in itself, attempting to answer the question along the lines of "How can a flexible skin system be integrated with a distributed TRIC morphing wing to achieve a fully functional seamless morphing wing that is scalable to larger wing sizes?"

9

Conclusions

The objective of this thesis was to design a seamlessly distributed smart trailing edge TRIC concept morphing wing able to achieve simultaneous load alleviation, flutter suppression and drag minimization capabilities. Also, the surrogate model mapping the input/output behaviour of the wing had to be developed to support the autonomous control of the wing.

To be able to meet the desired objectives, an aeroelastic analysis framework was built to define the laminate structure of the wing skin, and build a surrogate model of the system. To carry out the optimization task, the framework interfaced MSC NASTRAN's optimization solver with XFOIL to assess the FSI of the wing structure using aerodynamic strip theory model assumptions. This analysis method served the objective of minimizing actuation forces to the morph the wing in the most adverse bending and twist configurations, with trailing edge tip deflections that ranged from $-20mm$ to $30mm$. A laminate structure was defined with a ply dropping sequence on the morphing trailing surface, with woven fibre-glass plies, oriented in the $\pm 45^\circ$ orientation selected. The remainder of the wing structure, inclusive of the wingbox was designed relatively rigid in comparison to the morphing trailing surface. To carry out the actuation task, the VOLZ DA22-12-4112 servos were selected.

The task of achieving a seamlessly transitioning wing skin with independently morphing trailing edge modules was completed with the development of analytical models and extending the design work to prototype testing. Several concepts were trialed in the simulation environment, but failed to converge, promoting real-world testing. A printed test setup was produced with continuity concepts trialed on samples that were also printed. Three different designs were tested to conclude that achieving seamless transitioning would be made possible by connecting adjacent wing modules with a $30mm$ wide silicone segment.

Preparations for building a full-scale surrogate model were started by establishing an input-output mapping of actuation position/angle-of-attack to lift increment with a linear inviscid aeroelastic analysis model. This system was theoretically able to approximate idealized behaviour of a single module at low angles of attack where viscous flow effects would be less prominent. A linear relationship was found between actuation inputs, angle-of-attack and lift increment.

To verify the analysis models that were built, DIC testing was conducted on the wing. Several tests evaluating the deformations of the wing with and without the influence of the shearing of the silicone connection were carried out. Key observations from the testing showed the morphing deformations achieved at the trailing edge tip were much lower than idealized in simulation, being caused a substantial loading moment pivoting the sliding surface in place of providing chordwise translation need to achieve higher deflections. Additionally, the influence of the elastomer on the morphing range was substantial when choosing to bend up relative to adjacent modules bending down. The shearing of the silicone proved to be too stiff, and hence any bend up motion was compromised by the out-of-plane

bulging of the wing skin.

At the conclusion of this thesis, a wing prototype was built and tested in the wind tunnel environment to show capabilities in achieving load alleviation, flutter suppression and minimizing drag. Structural testing, however, showed some limitations, which formulated some of the recommendations for future work in improving the design and analysis framework. Namely, these were (i) improve the accuracy of the FEM model to take into account loading moments applied with a sliding surface pickup point that is offset from the plane of the sliding surface, and (ii) perform a well executed analysis and testing approach for the design of seamless continuity between adjacent modules to be able to successfully morph each wing module to the full design range, independent of the position of the adjacent module. Finally, the surrogate model should be enhanced to take into account more accurate flow modelling with 3D flow effects and viscous flow models integrated to benefit autonomous control of the wing. This modelling work could be further validated and calibrated with wind tunnel test results that were acquired from the testing conducted at the OJF.

A

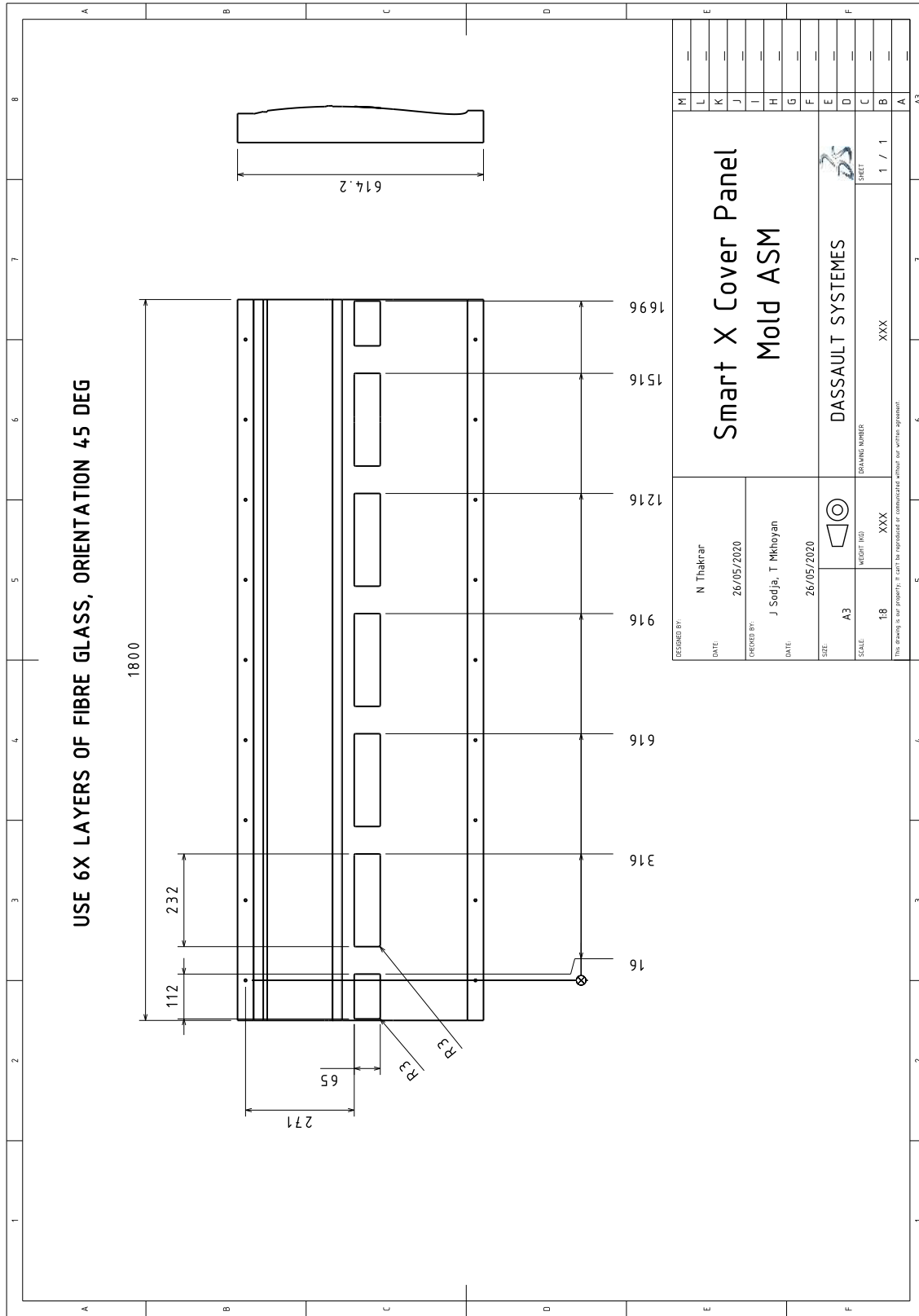
VOLZ SERVOS Performance Specifications

Table A.1: VOLZ SERVOS Performance Specifications [11]

Name	Peak Torque [N.cm]	Response Time [ms]	Minimum Arm Length [cm]
DA10-05-42	5	325	0.7
DA13-05-32	4.5	520	0.7
DA13-05-60	6	310	0.7
DA14-05-32	4.5	510	0.7
DA14-05-60	6	310	0.7
DA15-05-32	5	510	0.7
DA15-05-60	6.5	310	0.7
DA15-N-12-BLDC	25	280	0.7
DA15-N-12-BLDC-32	18	500	0.7
DA20-12-2515	80	120	1.25
DA22-12-2615	80	120	1.25
DA22-12-4112	120	180	1.25

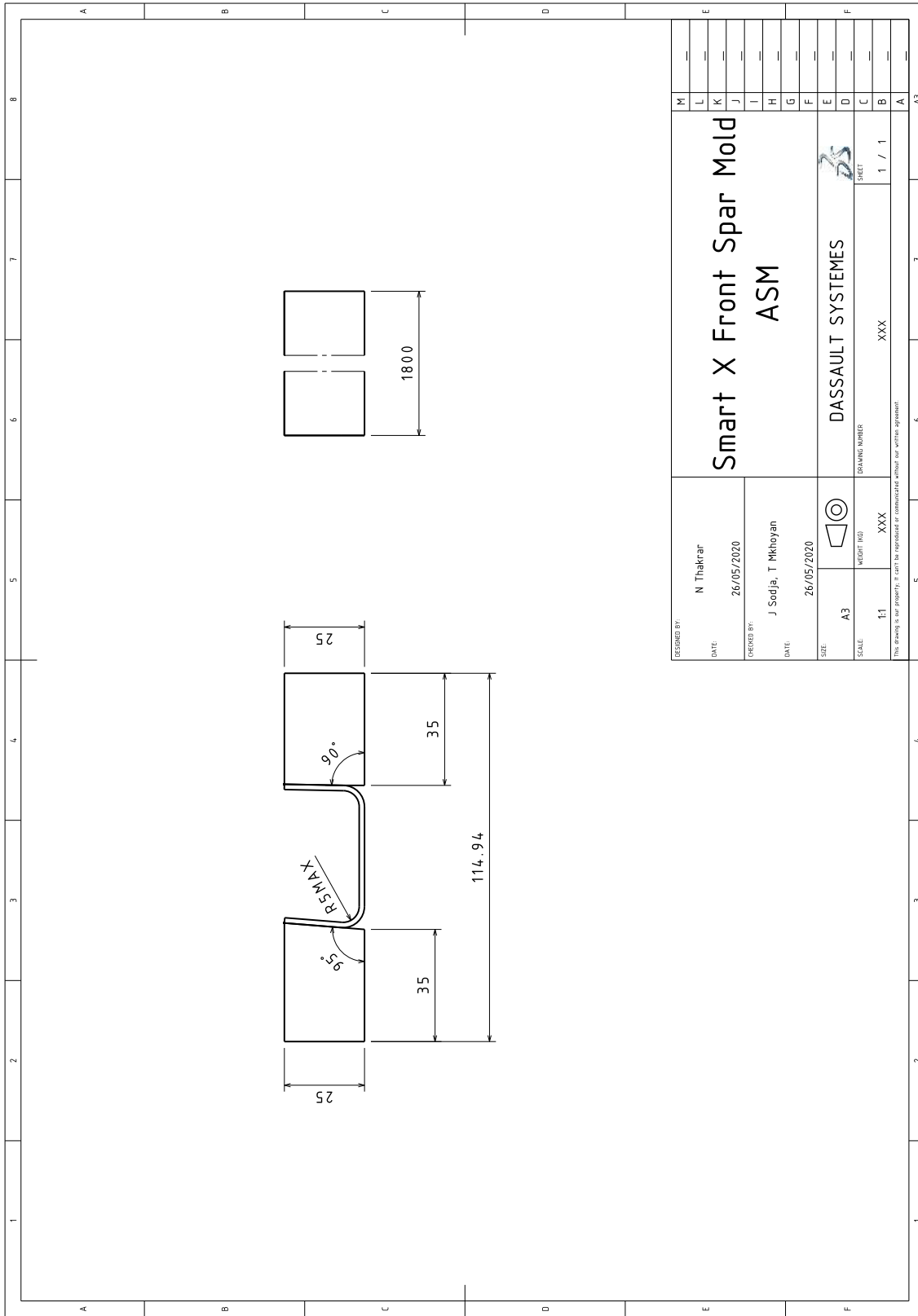
B

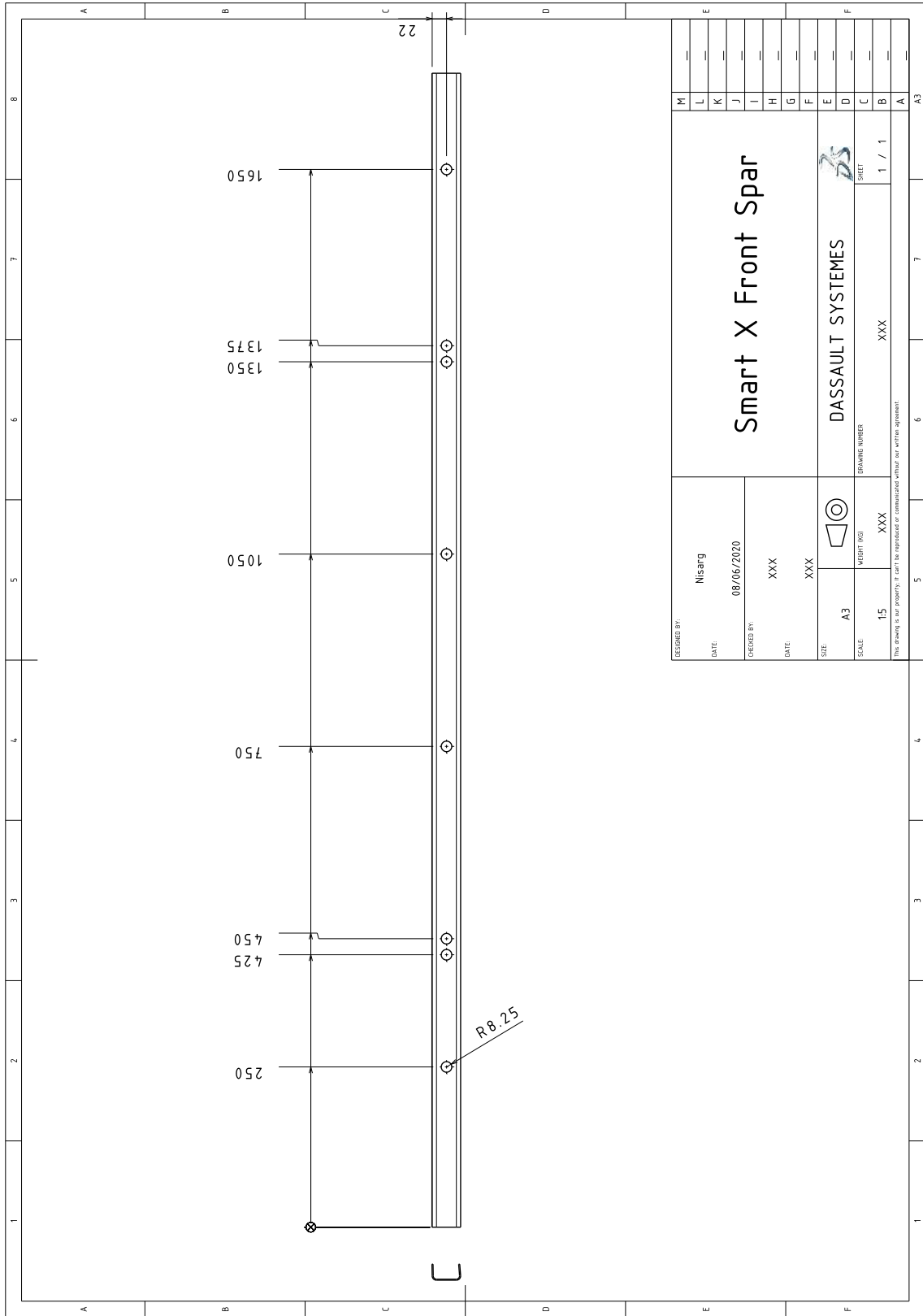
Technical Drawings

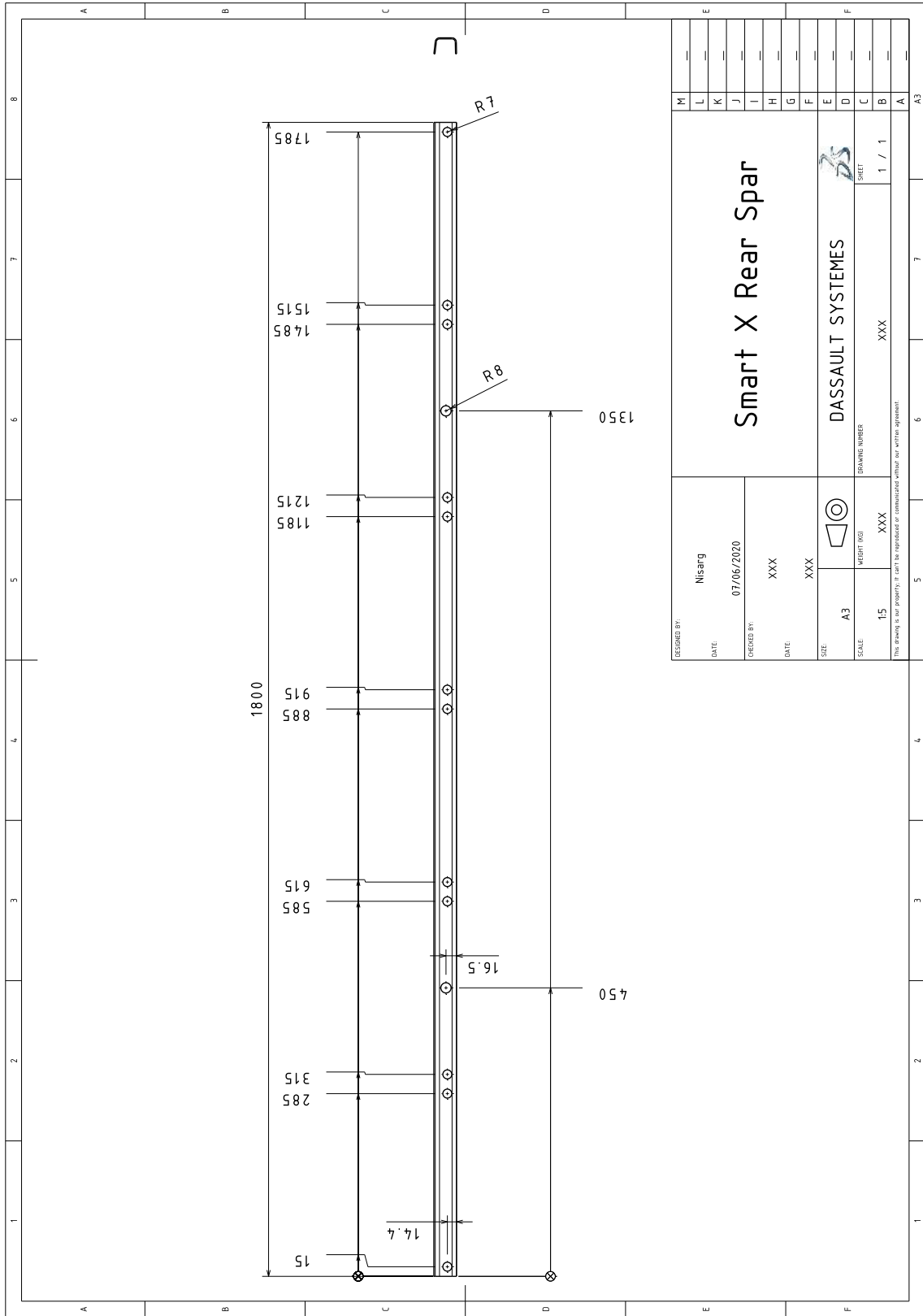


DESIGNED BY:	N Thakrar	DATE:	26/05/2020
CHECKED BY:	J Sodja, T Mkhoyan	DATE:	26/05/2020
SIZE:	A3	HEIGHT (mm):	XXX
SCALE:	1:8	DRAWING NUMBER:	XXX
This drawing is our property, it can't be reproduced or communicated without our written agreement.			

Smart X Cover Panel Mold ASM		DASSAULT SYSTEMES	
1 / 1		1 / 1	







DESIGNED BY:	Nisarg	DATE:	07/06/2020
CHECKED BY:	XXX	DATE:	XXX
SCALE:	A3	WEIGHT (KG):	XXX
SCALE:	1:5	DRAWING NUMBER:	XXX
This drawing is our property. It can be reproduced or communicated without our written agreement.			

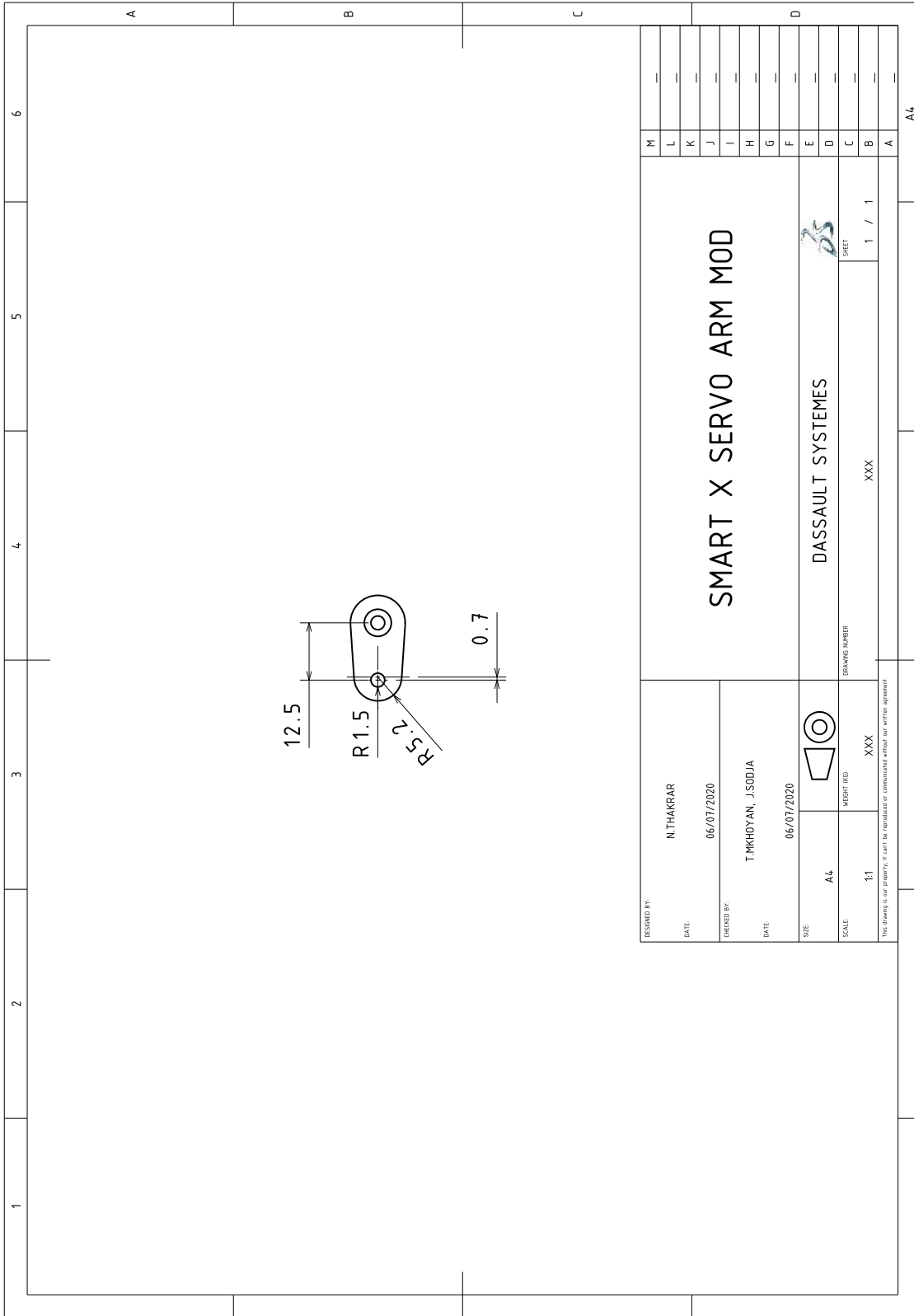
M	---
L	---
K	---
J	---
I	---
H	---
G	---
F	---
E	---
D	---
C	---
B	---
A	---

Smart X Rear Spar

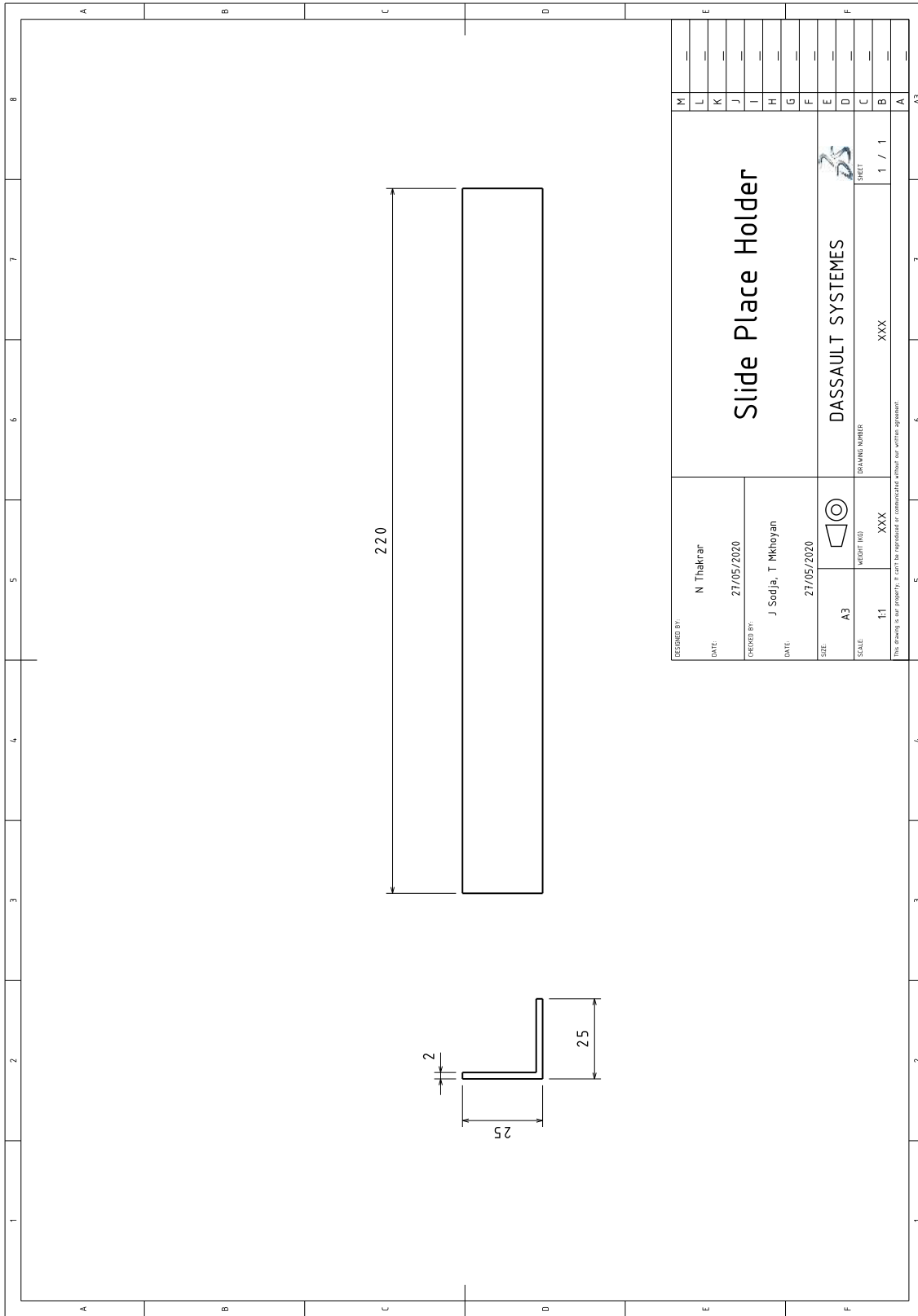
DASSAULT SYSTEMES

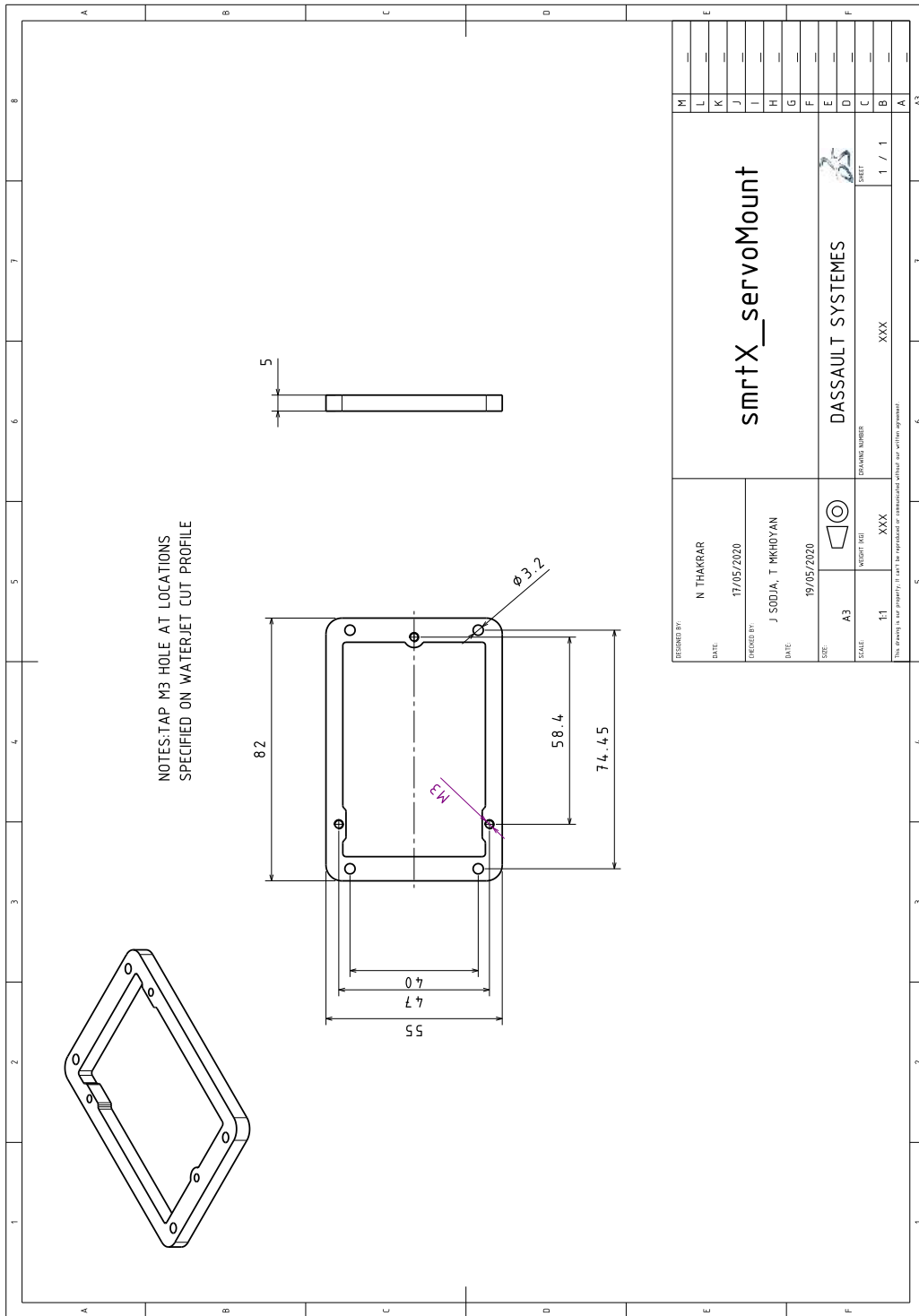
SHEET
1 / 1

5	6	7	A3
---	---	---	----



DESIGNED BY: N. THAKRAR	DATE: 06/07/2020	CHECKED BY: TIMHOYAN, JSODJA	DATE: 06/07/2020	SIZE: A4	WEIGHT (KG): XXX	SCALE: 1:1	DRAWING NUMBER: XXX	SHEET: 1 / 1	M	L	K	J	I	H	G	F	E	D	C	B	A
SMART X SERVO ARM MOD																					
DASSAULT SYSTEMES																					
A4																					





DESIGNED BY:	N THAKRAR	DATE:	17/05/2020
REVIEWED BY:	J SODJIA, T MKHAYAN	DATE:	19/05/2020
SIZE:	A3	WEIGHT (KG):	XXX
SCALE:	1:1	DRAWING NUMBER:	XXX
THIS DRAWING IS THE PROPERTY OF DASSAULT SYSTEMES. IT IS TO BE REPRODUCED OR TRANSMITTED IN ANY FORM OR BY ANY MEANS, WITHOUT PERMISSION IN WRITING FROM DASSAULT SYSTEMES.			

smrtX_servoMount		M	---
		L	---
DASSAULT SYSTEMES		K	---
		J	---
1 / 1		I	---
		H	---
DASSAULT SYSTEMES		G	---
		F	---
1 / 1		E	---
		D	---
1 / 1		C	---
		B	---
1 / 1		A	---
		---	---

C

DIC Testing Results

C.1. Baseline Measurements

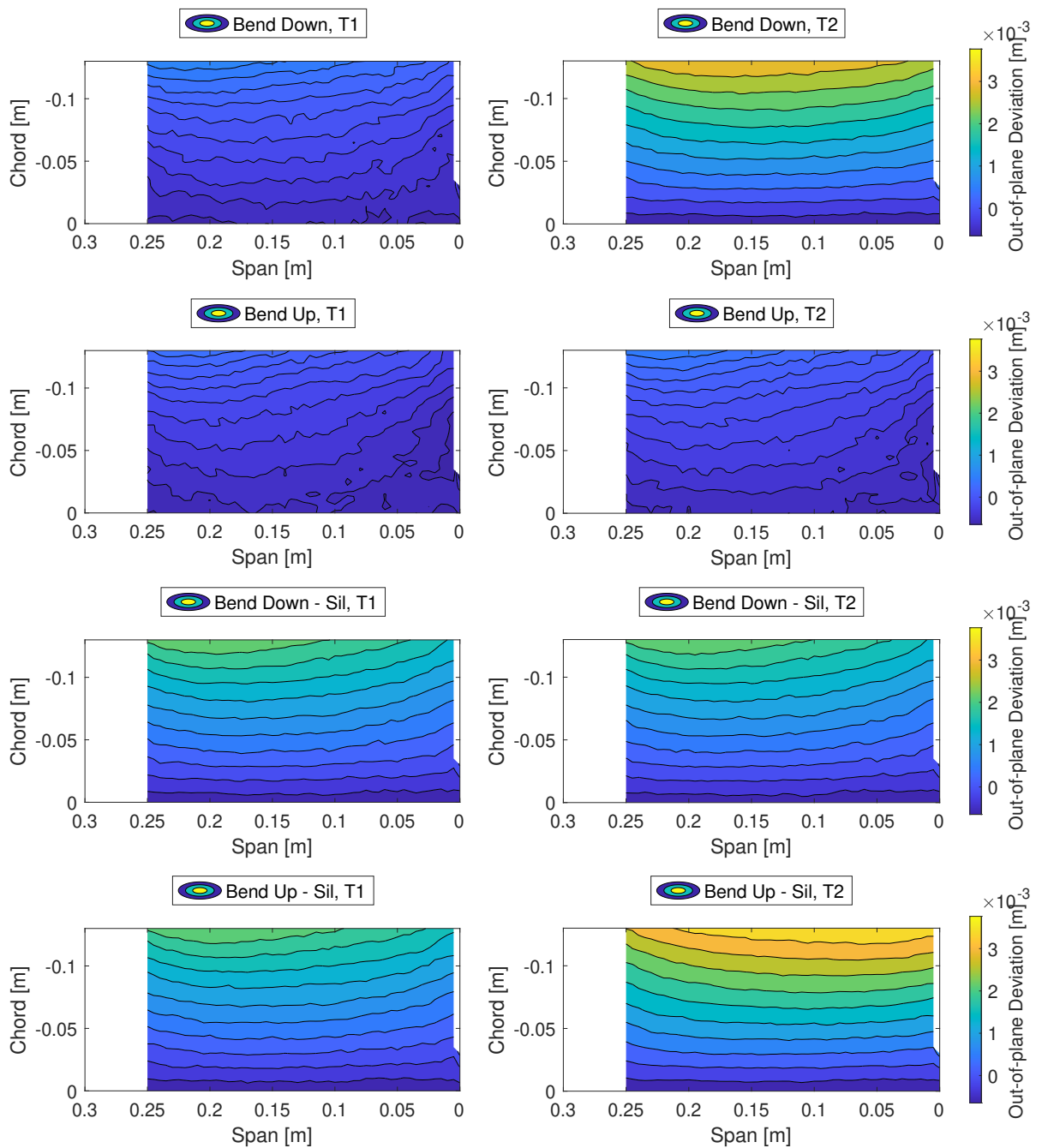


Figure C.1: Baseline measured surfaces compared to the ideal NACA6510 airfoil, bottom surface

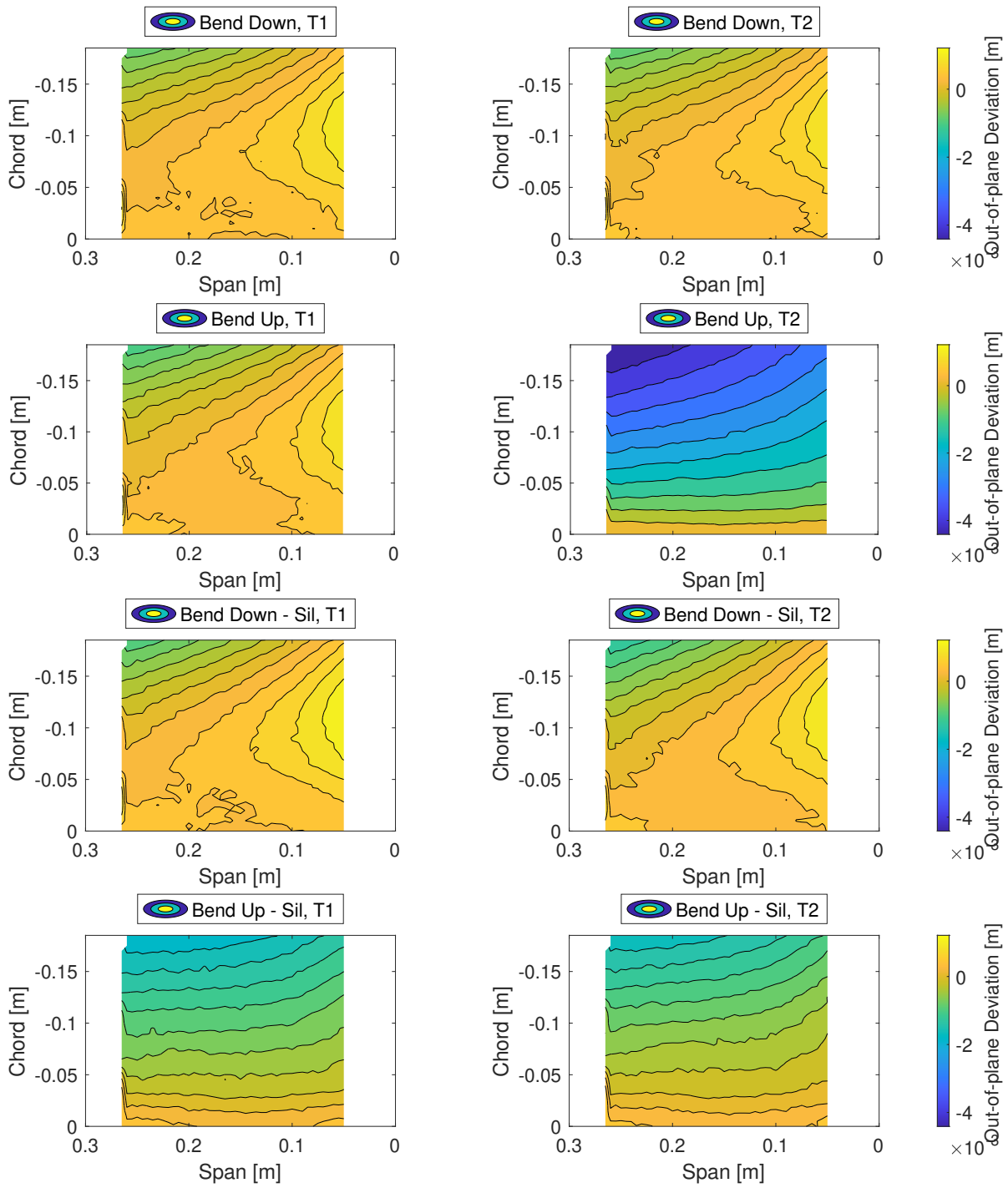


Figure C.2: Baseline measured surfaces compared to the ideal NACA6510 airfoil, top surface

C.2. Out-of-plane Deflection Measurements

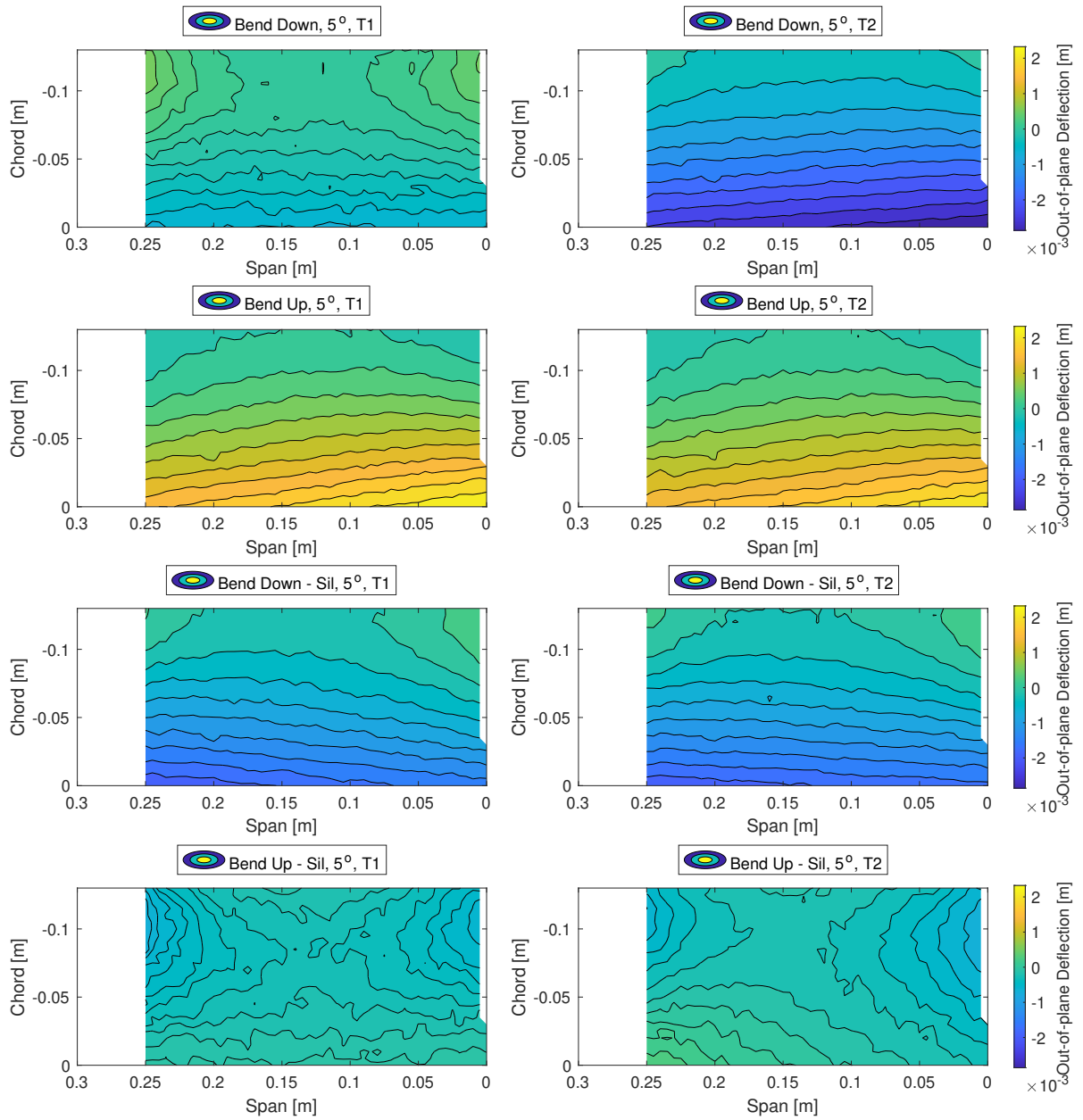


Figure C.3: Out-of-plane measurements on bottom surface for all tests at 5° actuation

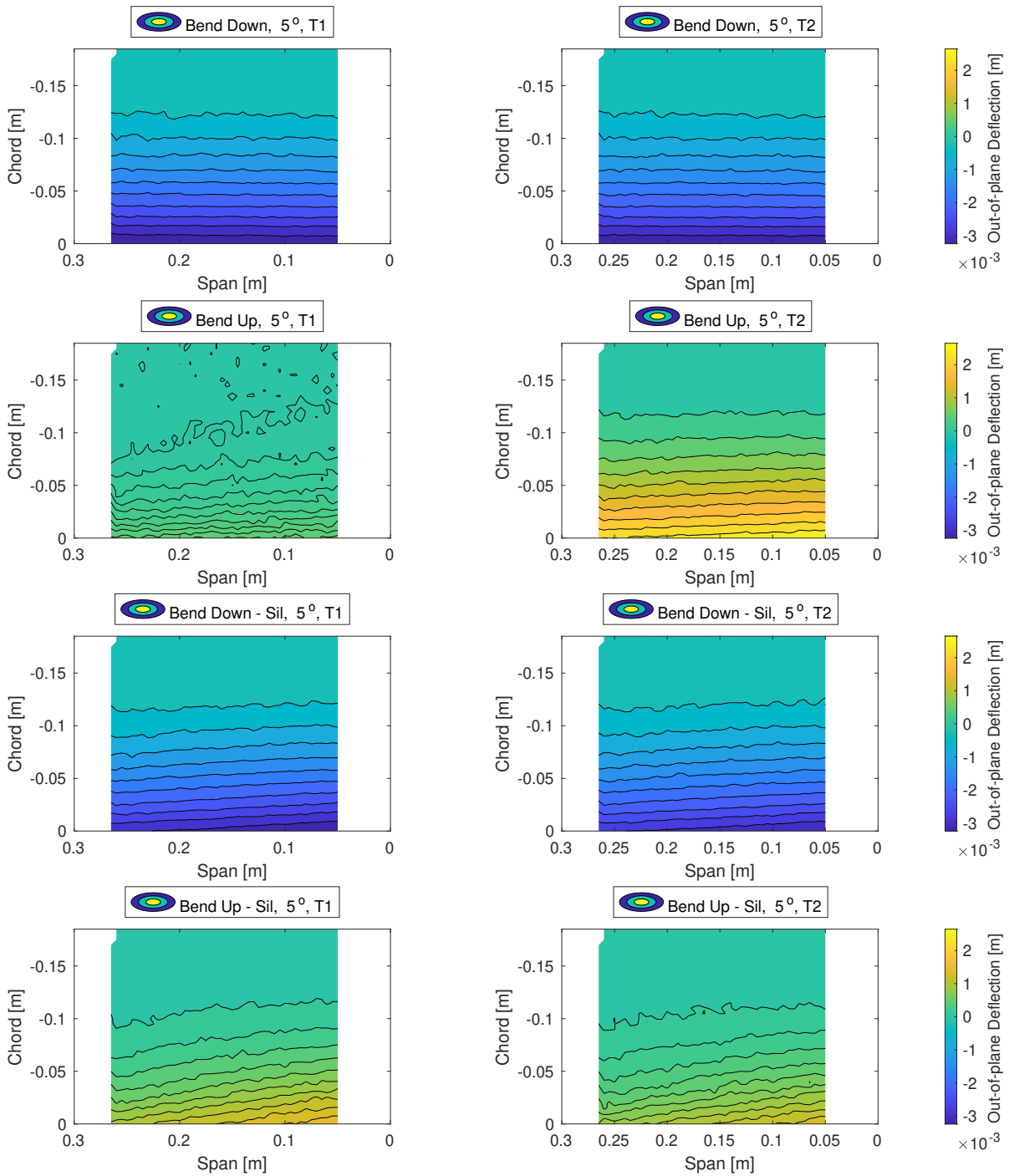


Figure C.4: Out-of-plane measurements on top surface surface for all tests at 5° actuation

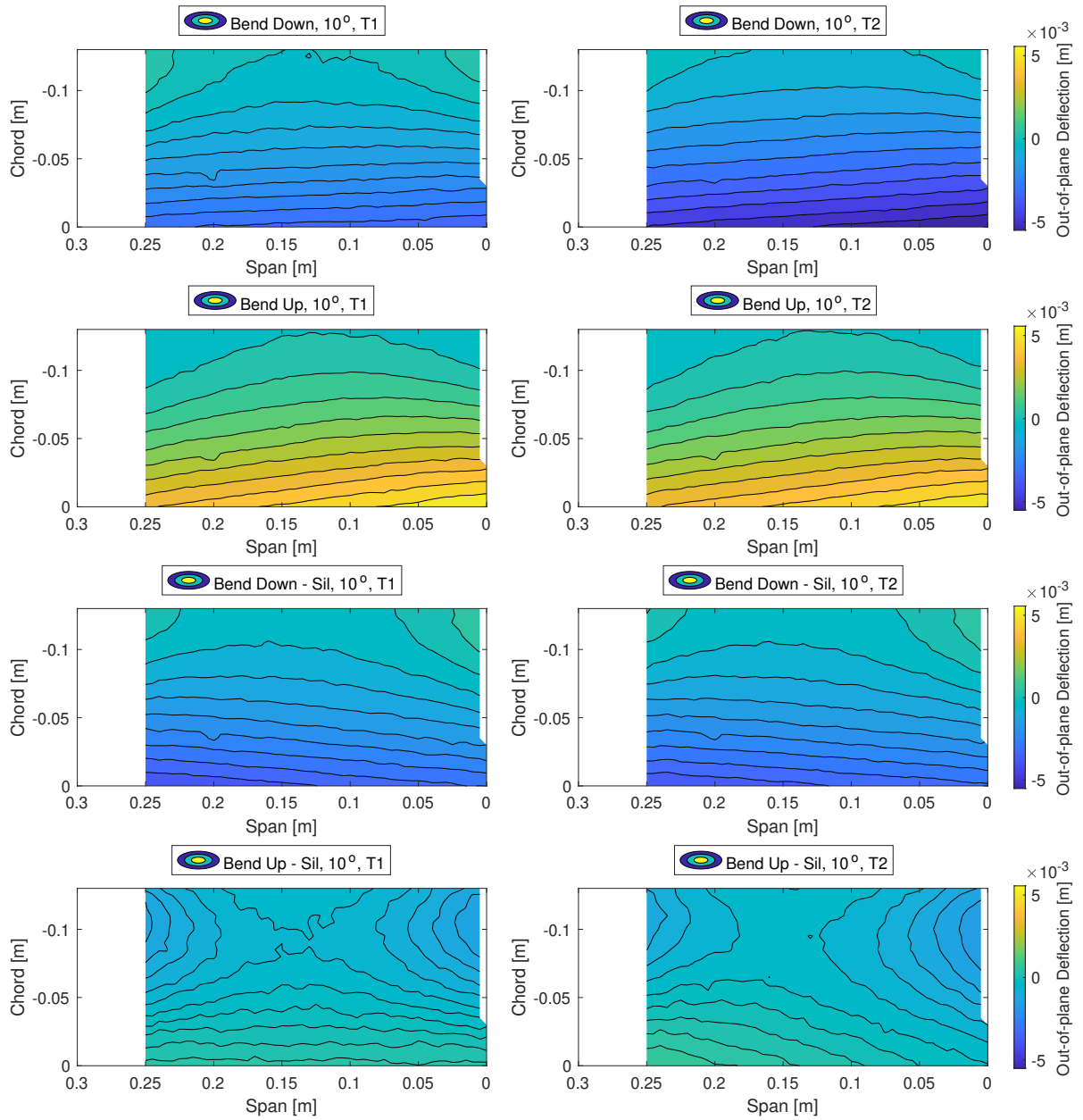


Figure C.5: Out-of-plane measurements on bottom surface for all tests at 10° actuation

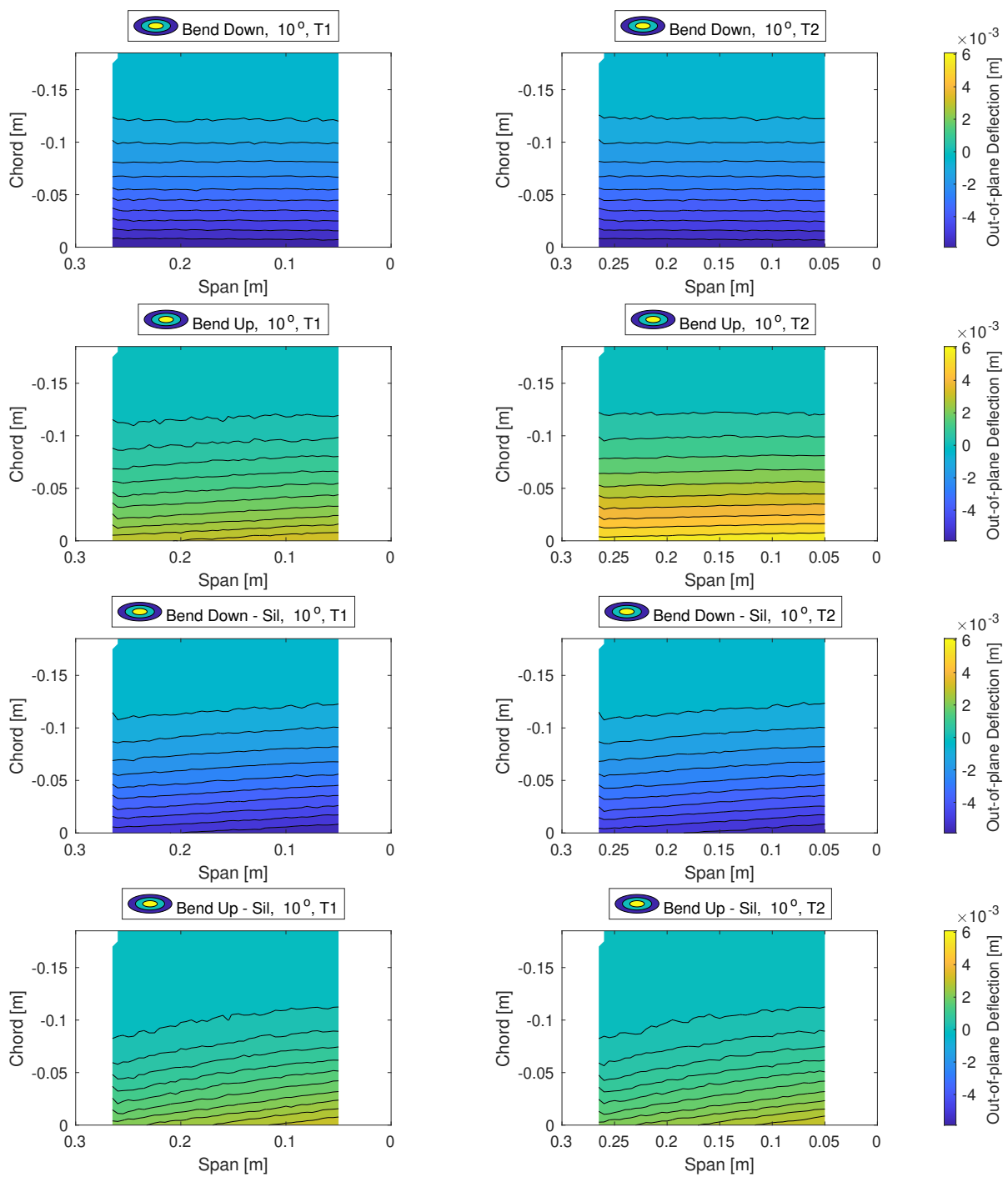


Figure C.6: Out-of-plane measurements on top surface surface for all tests at 10° actuation

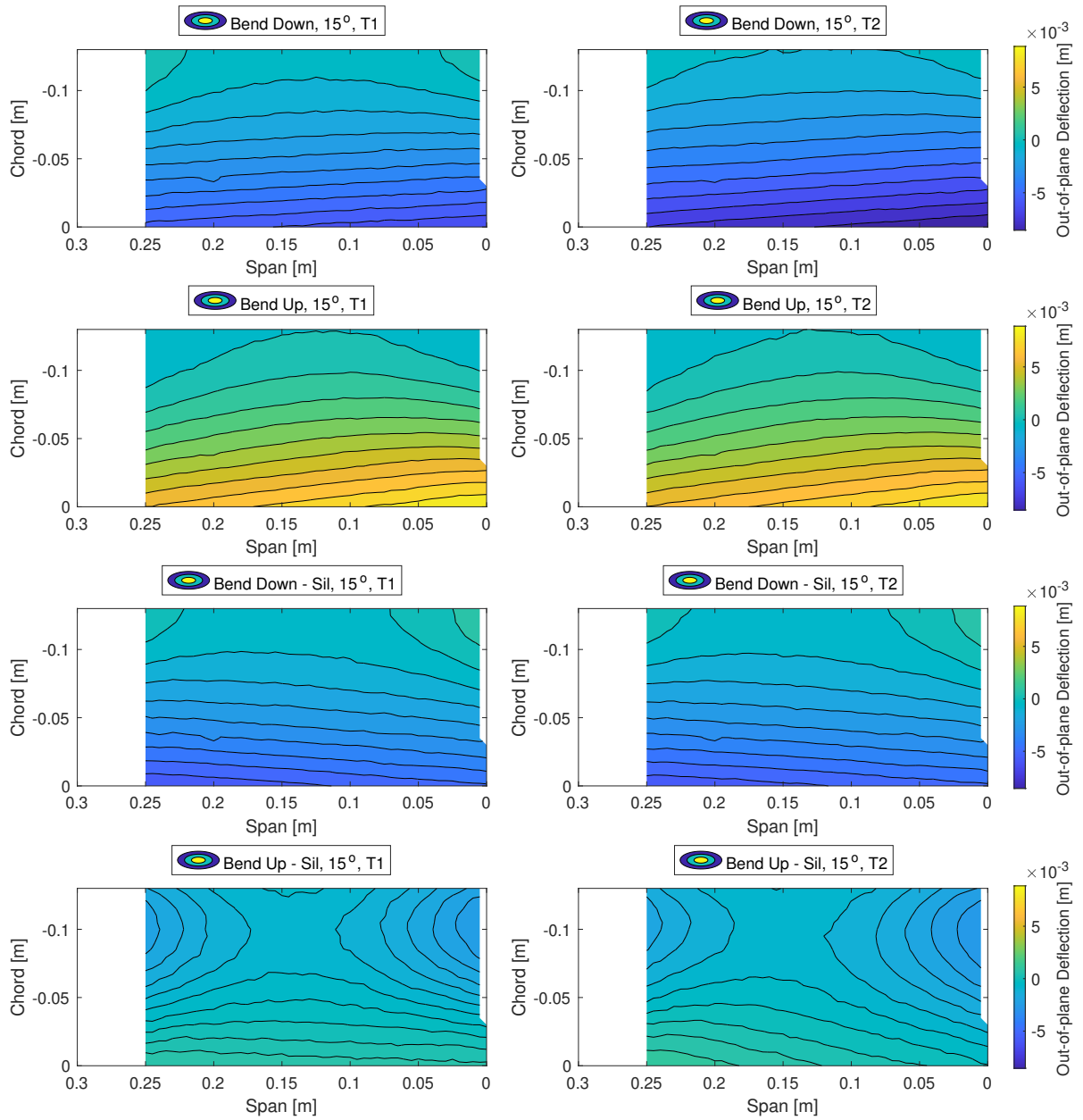


Figure C.7: Out-of-plane measurements on bottom surface for all tests at 15° actuation

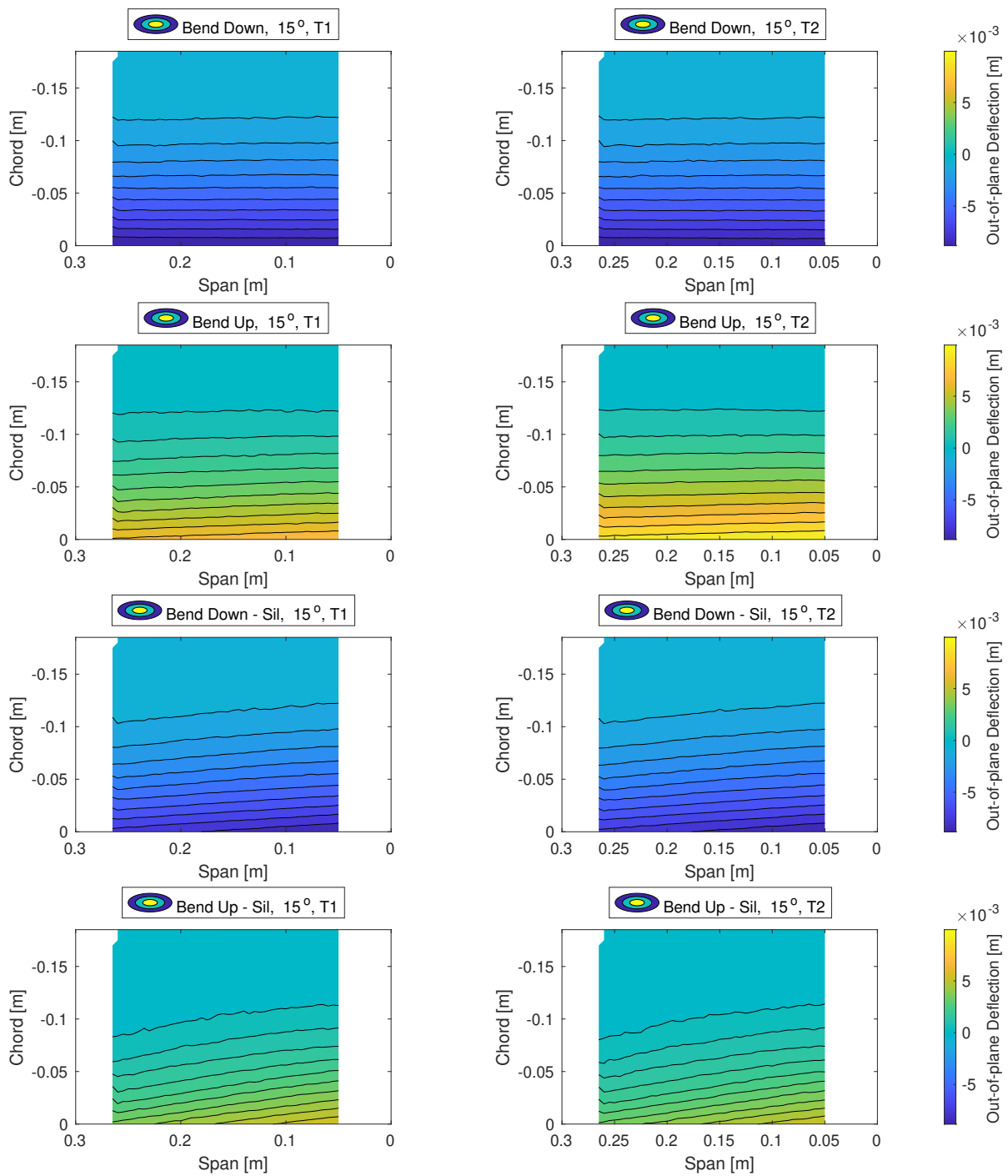


Figure C.8: Out-of-plane measurements on top surface surface for all tests at 15° actuation

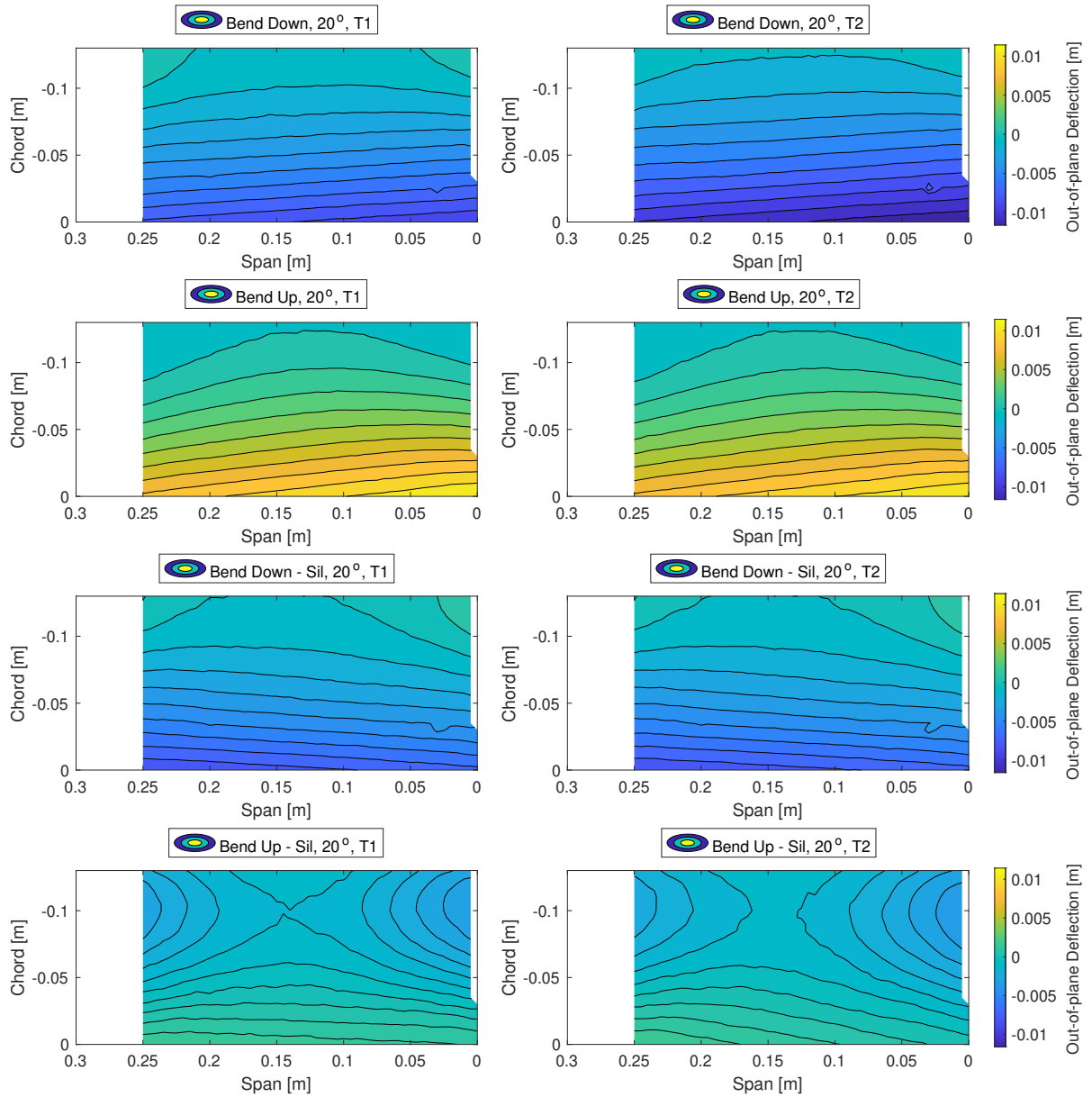


Figure C.9: Out-of-plane measurements on bottom surface for all tests at 20° actuation

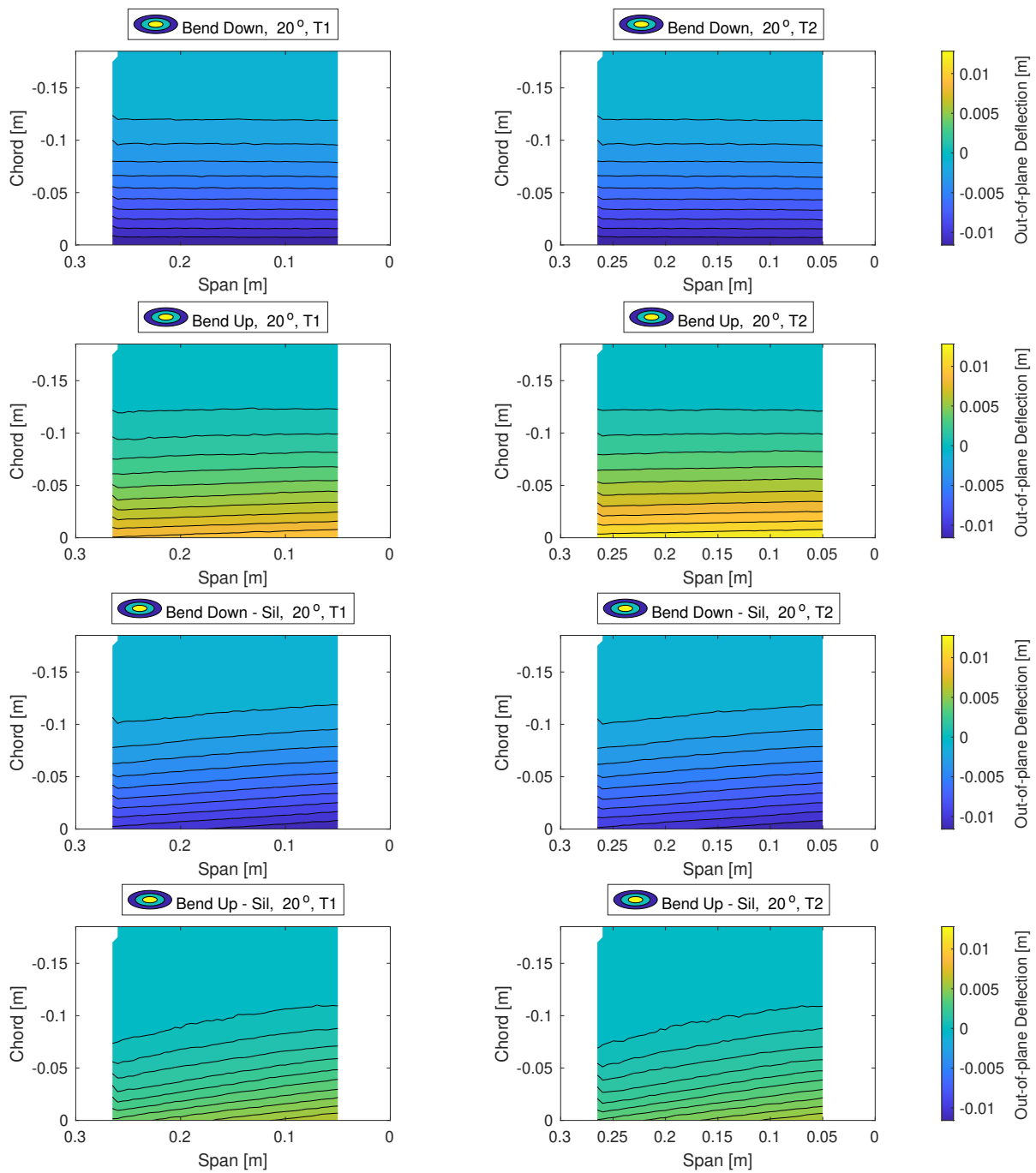


Figure C.10: Out-of-plane measurements on top surface surface for all tests at 20° actuation

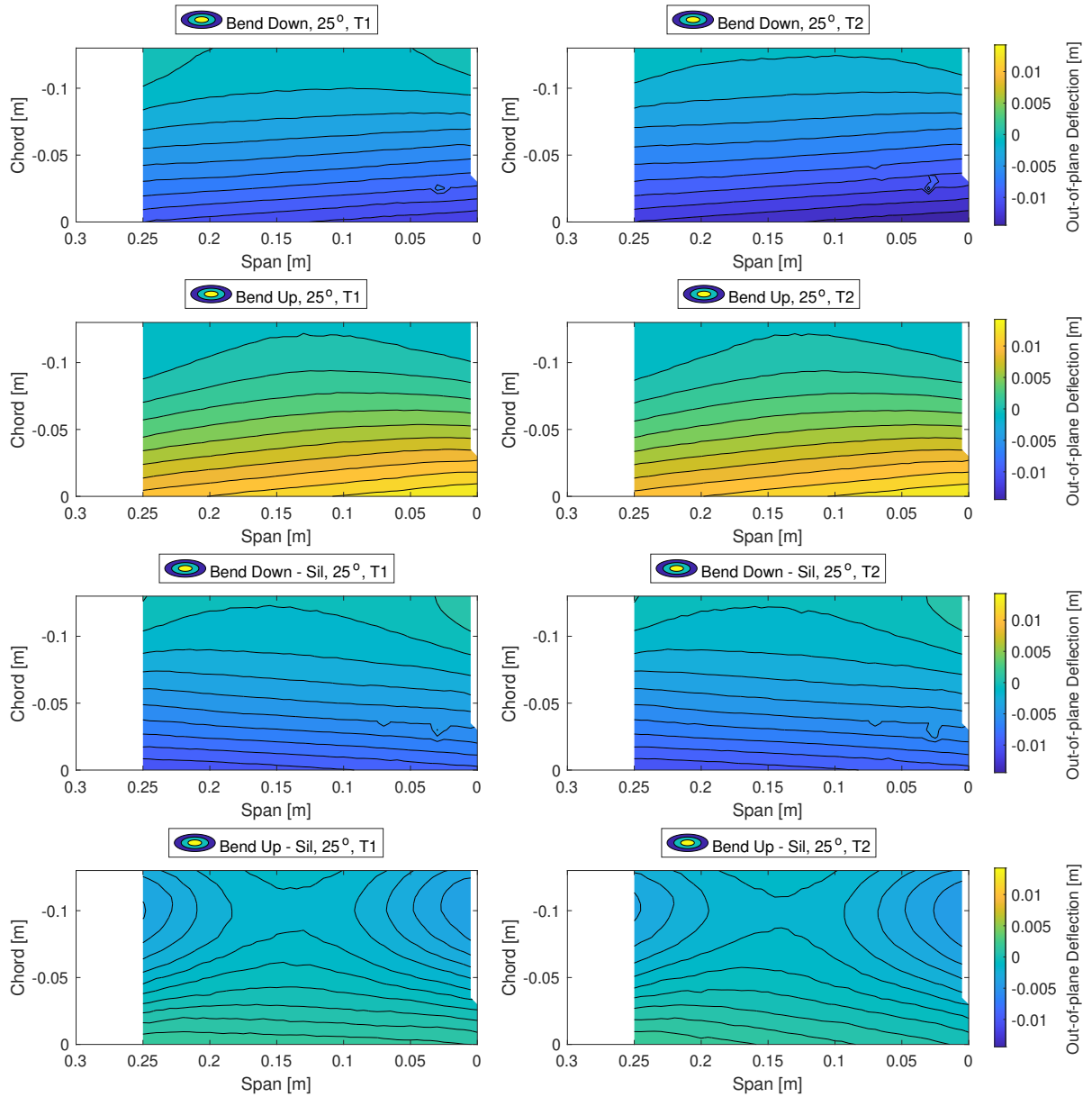


Figure C.11: Out-of-plane measurements on bottom surface for all tests at 25° actuation

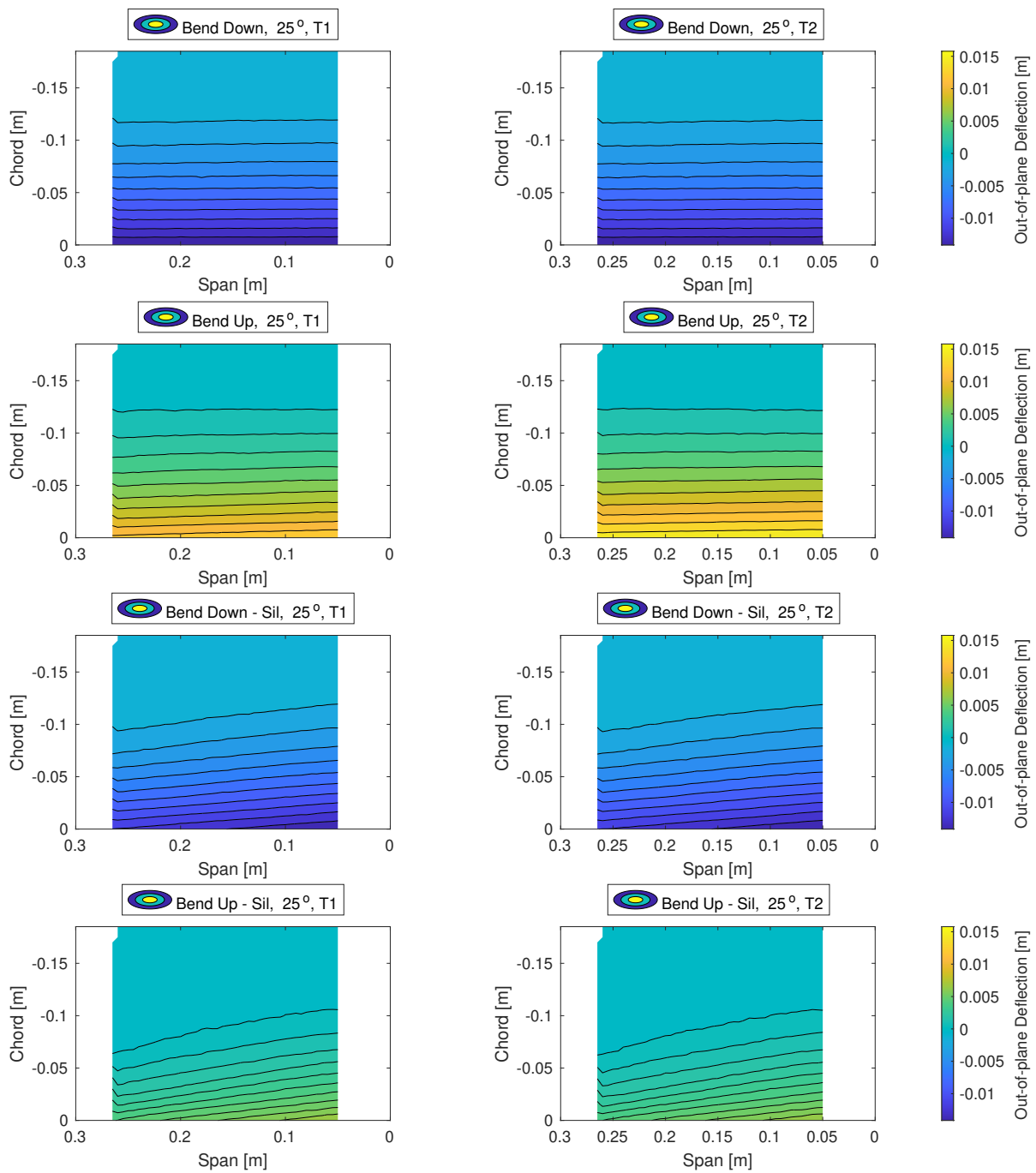


Figure C.12: Out-of-plane measurements on top surface surface for all tests at 25° actuation

C.3. Chordwise Deflection Measurements

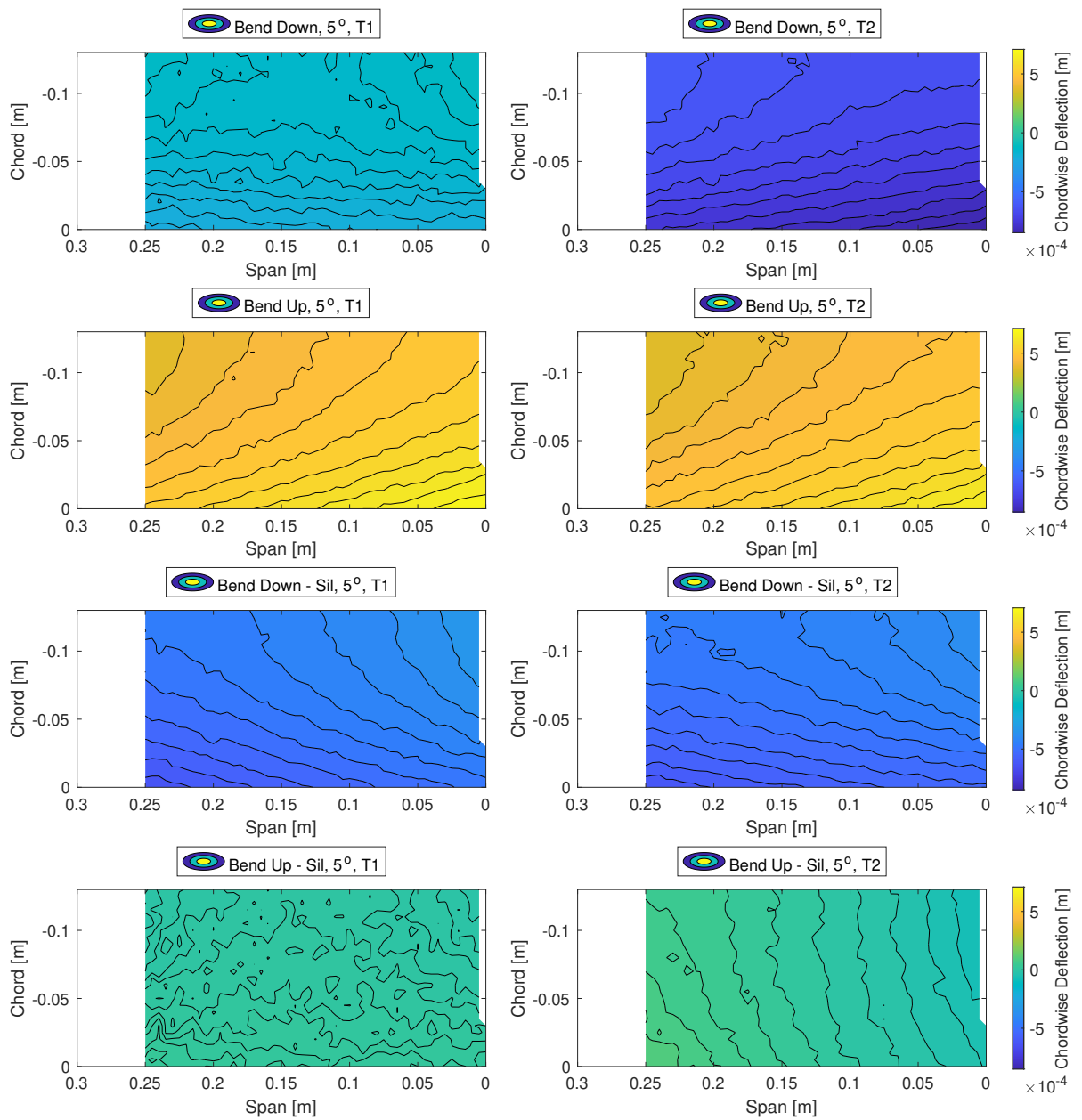


Figure C.13: Chordwise translation measurements on bottom surface for all tests at 5° actuation

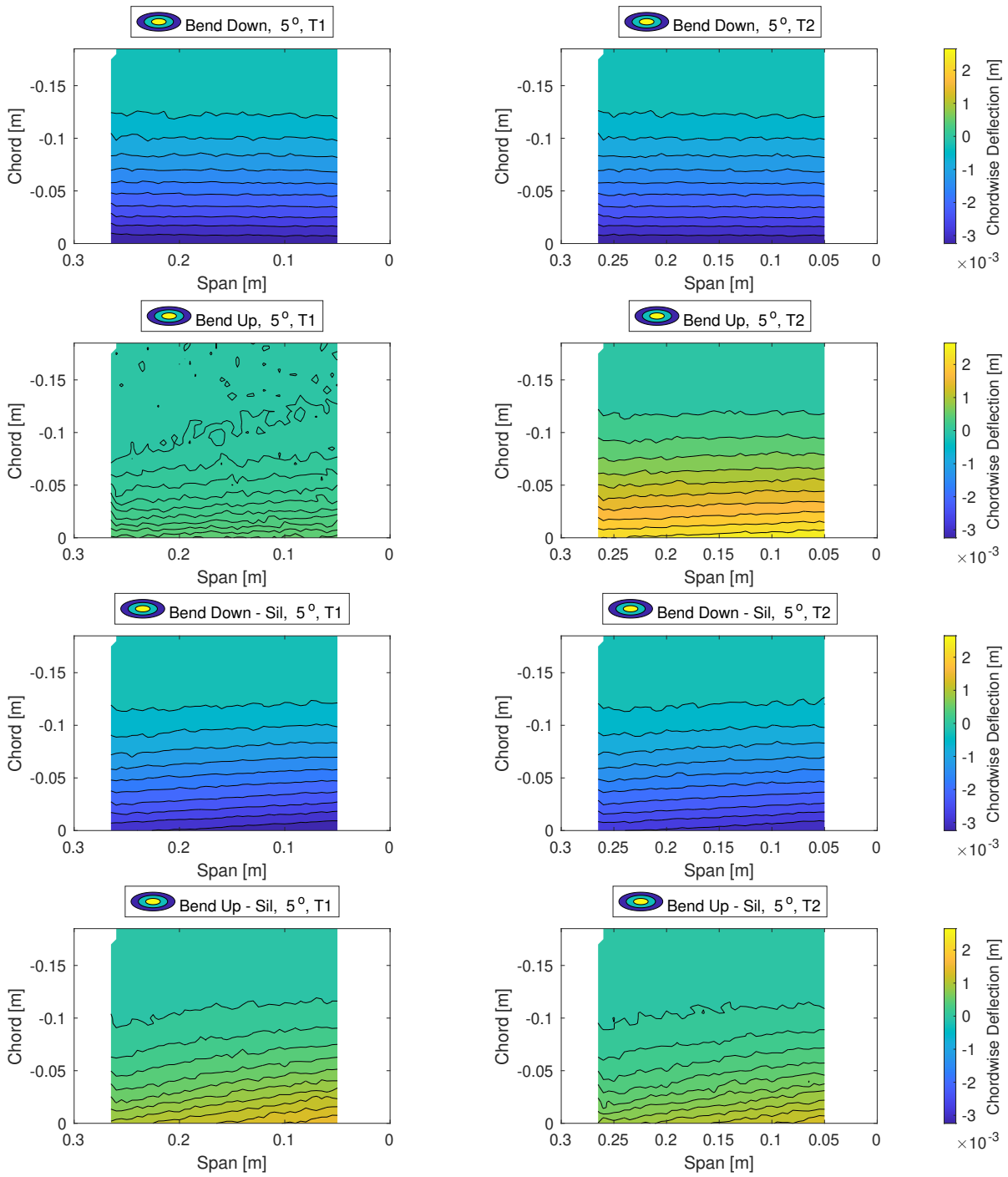


Figure C.14: Chordwise translation measurements on top surface surface for all tests at 5° actuation

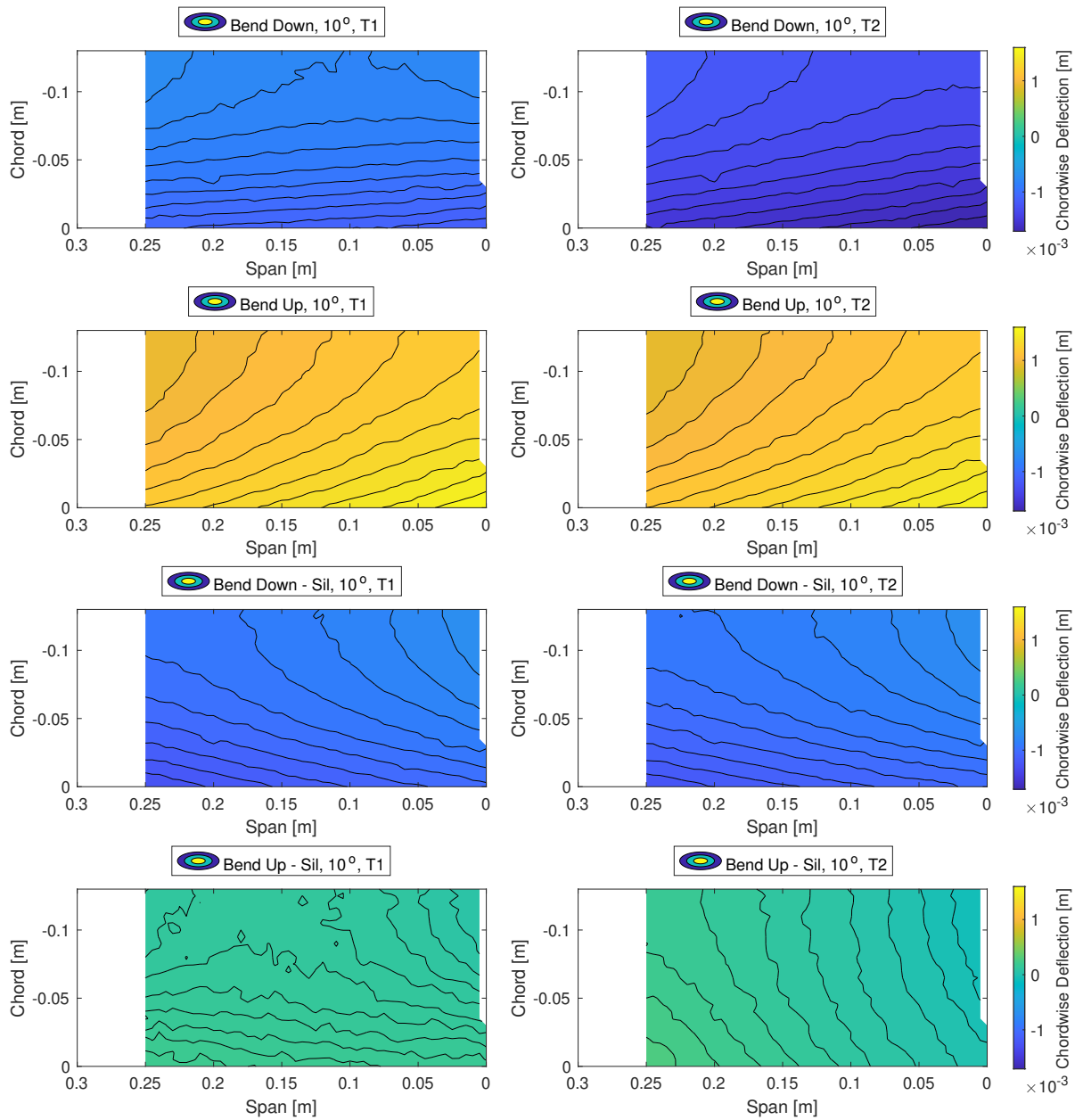


Figure C.15: Chordwise translation measurements on bottom surface for all tests at 10° actuation

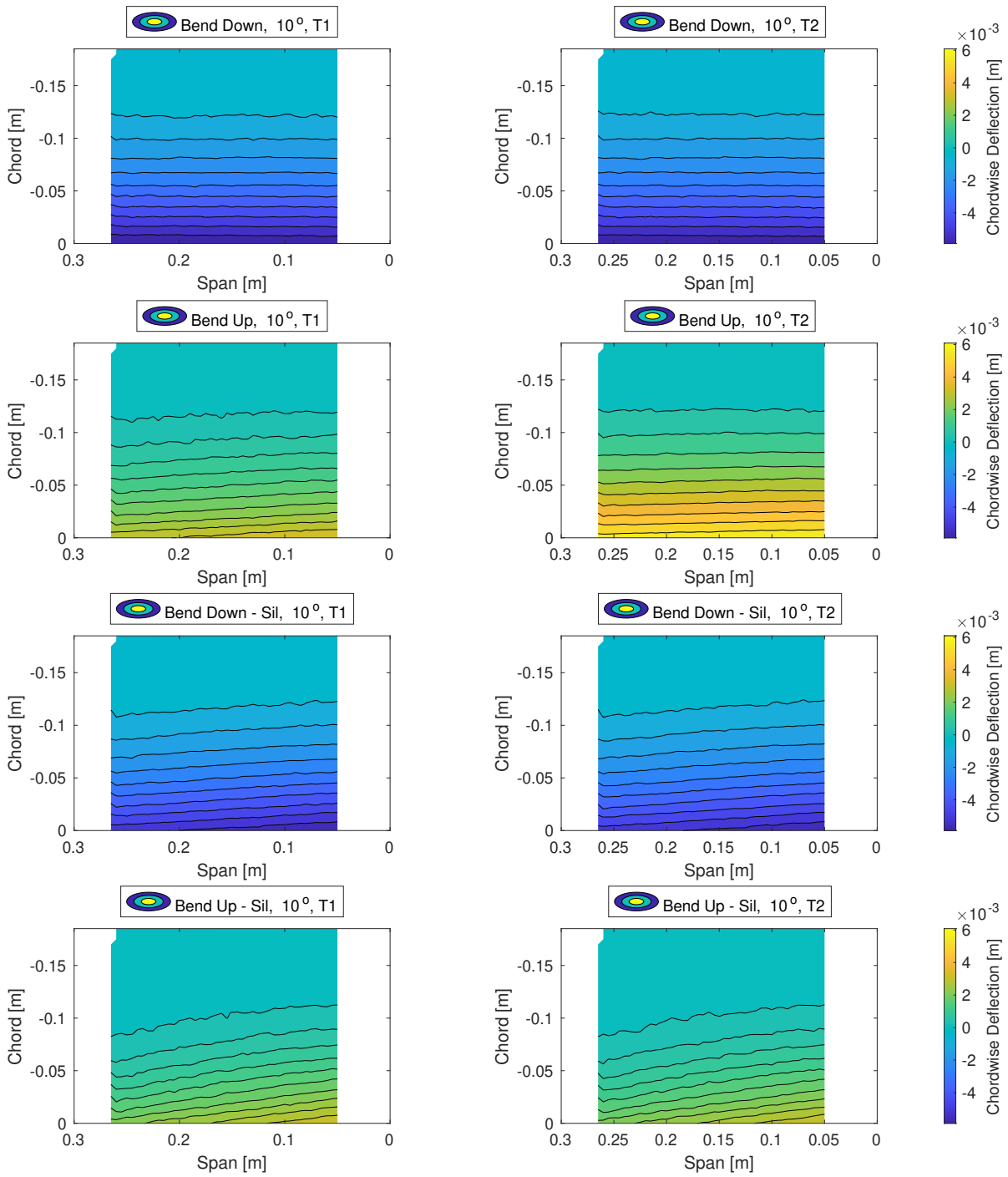


Figure C.16: Chordwise translation measurements on top surface surface for all tests at 10° actuation

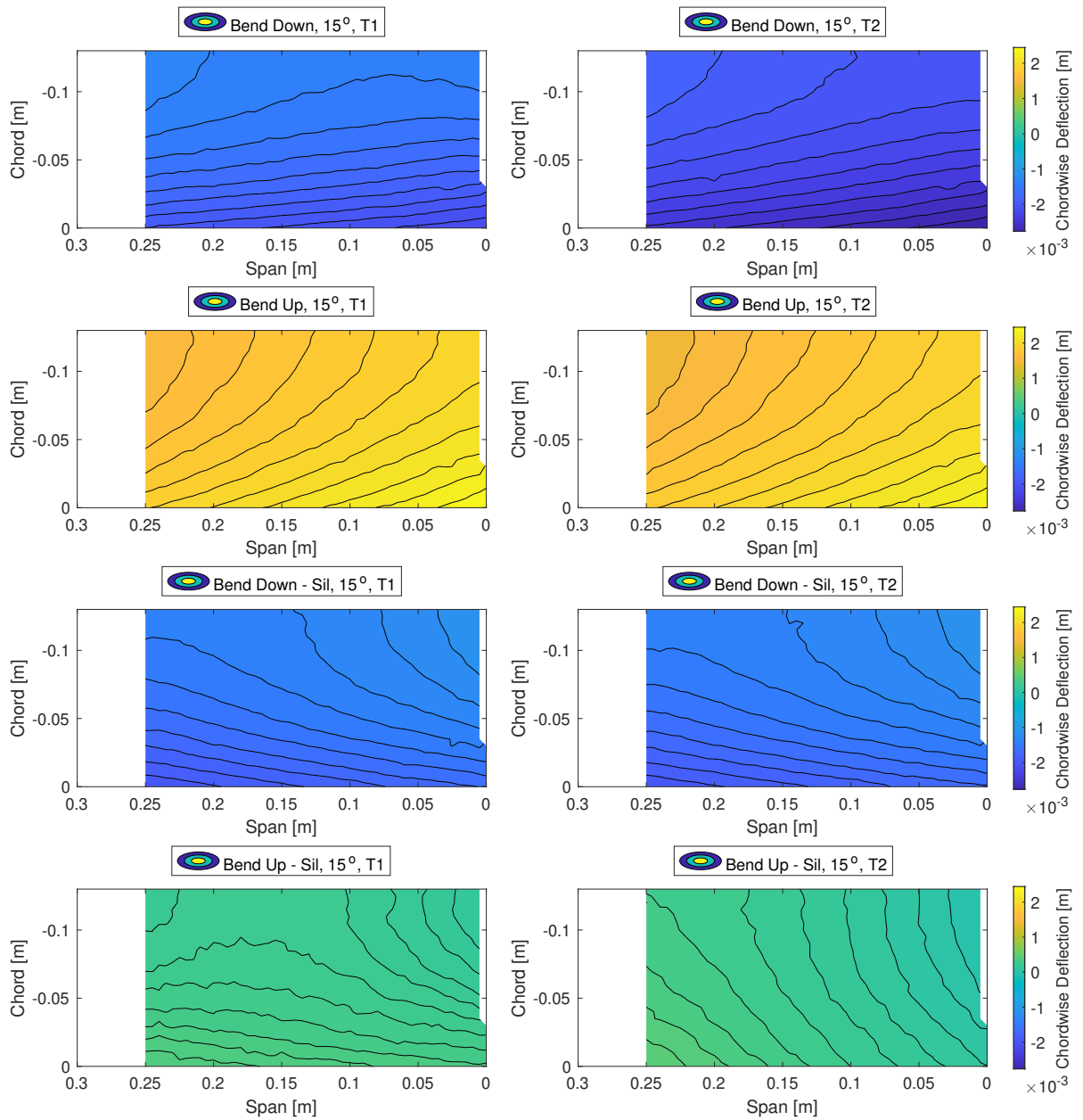


Figure C.17: Chordwise translation measurements on bottom surface for all tests at 15° actuation

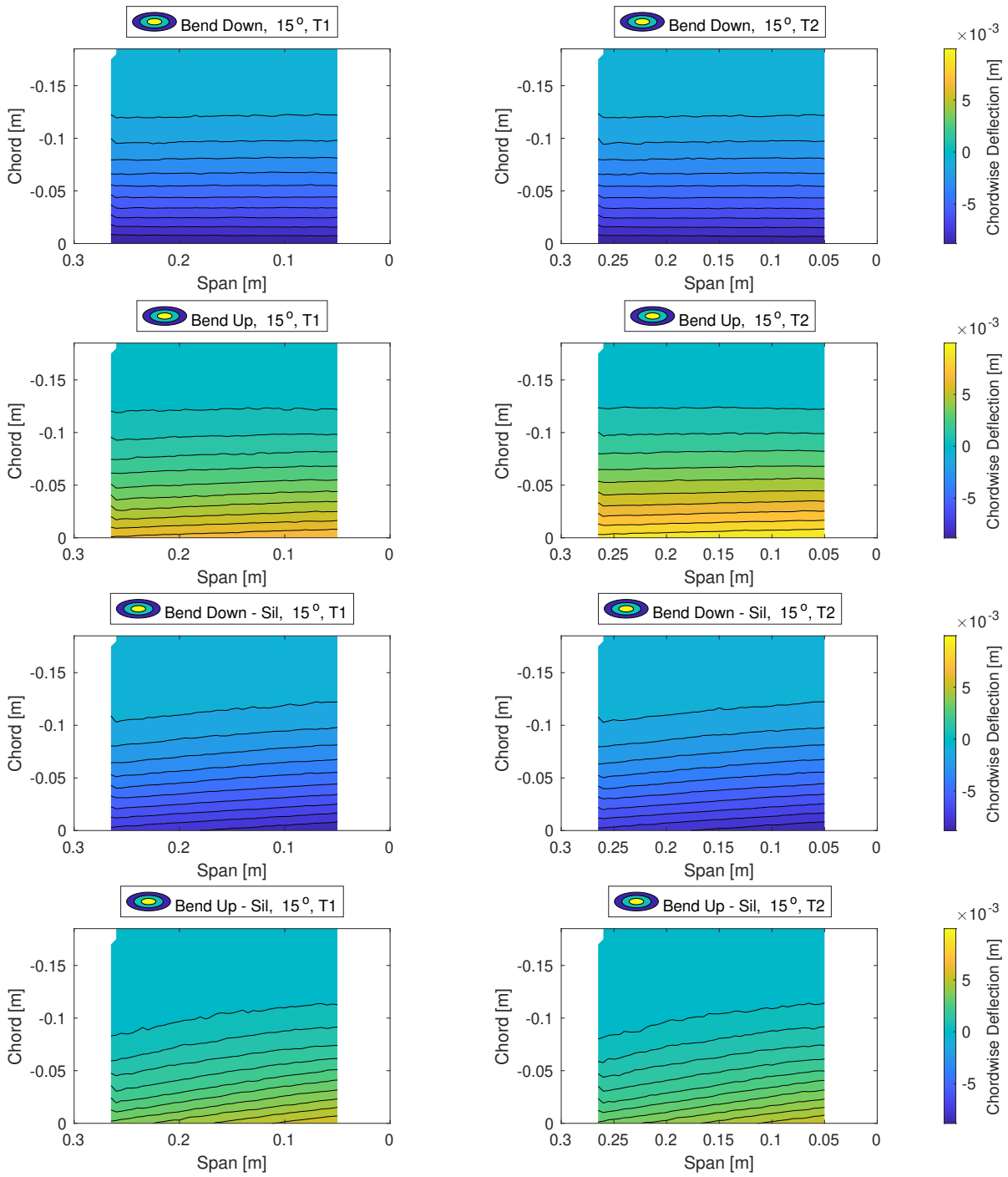


Figure C.18: Chordwise translation measurements on top surface surface for all tests at 15° actuation

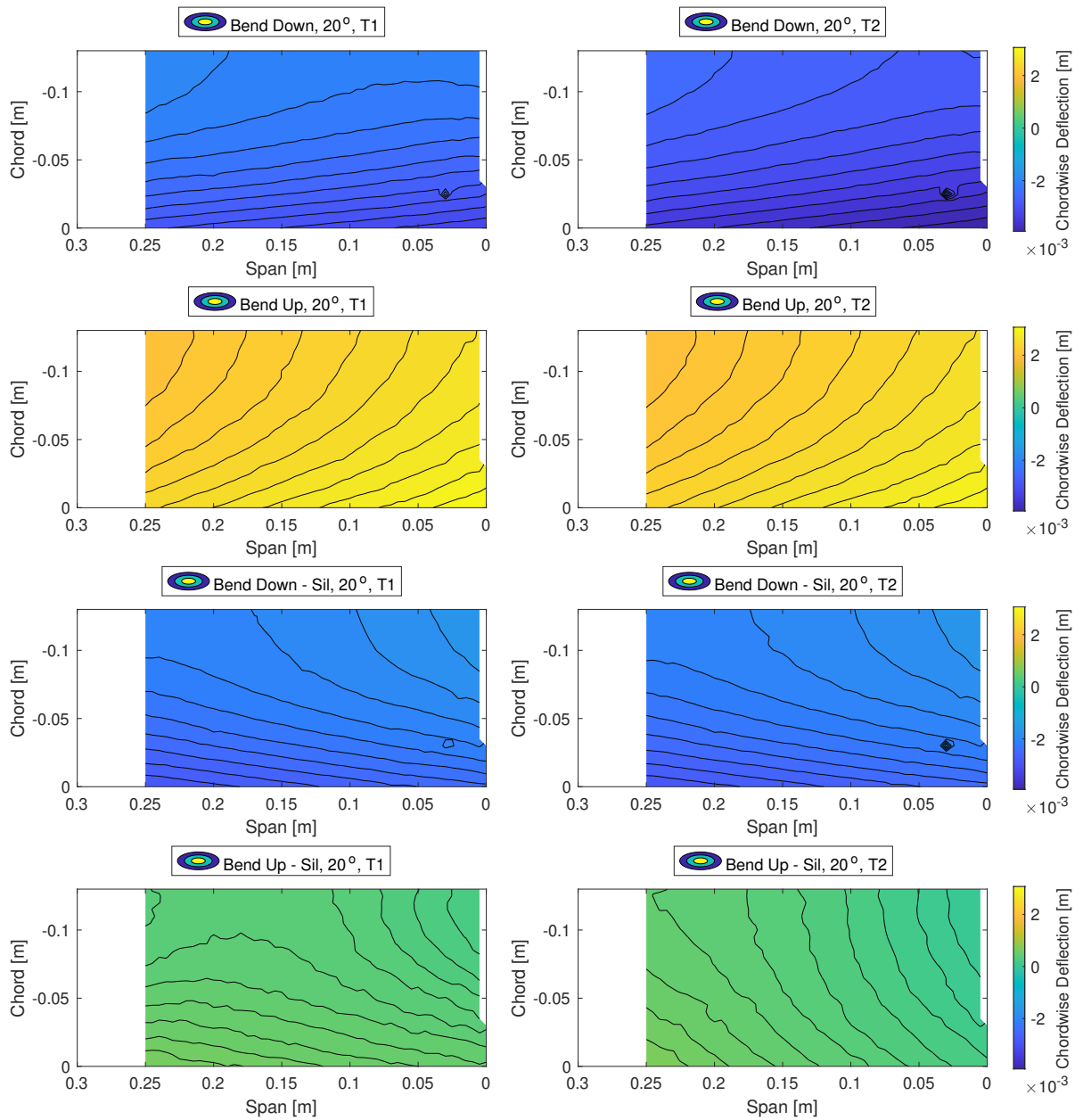


Figure C.19: Chordwise translation measurements on bottom surface for all tests at 20° actuation

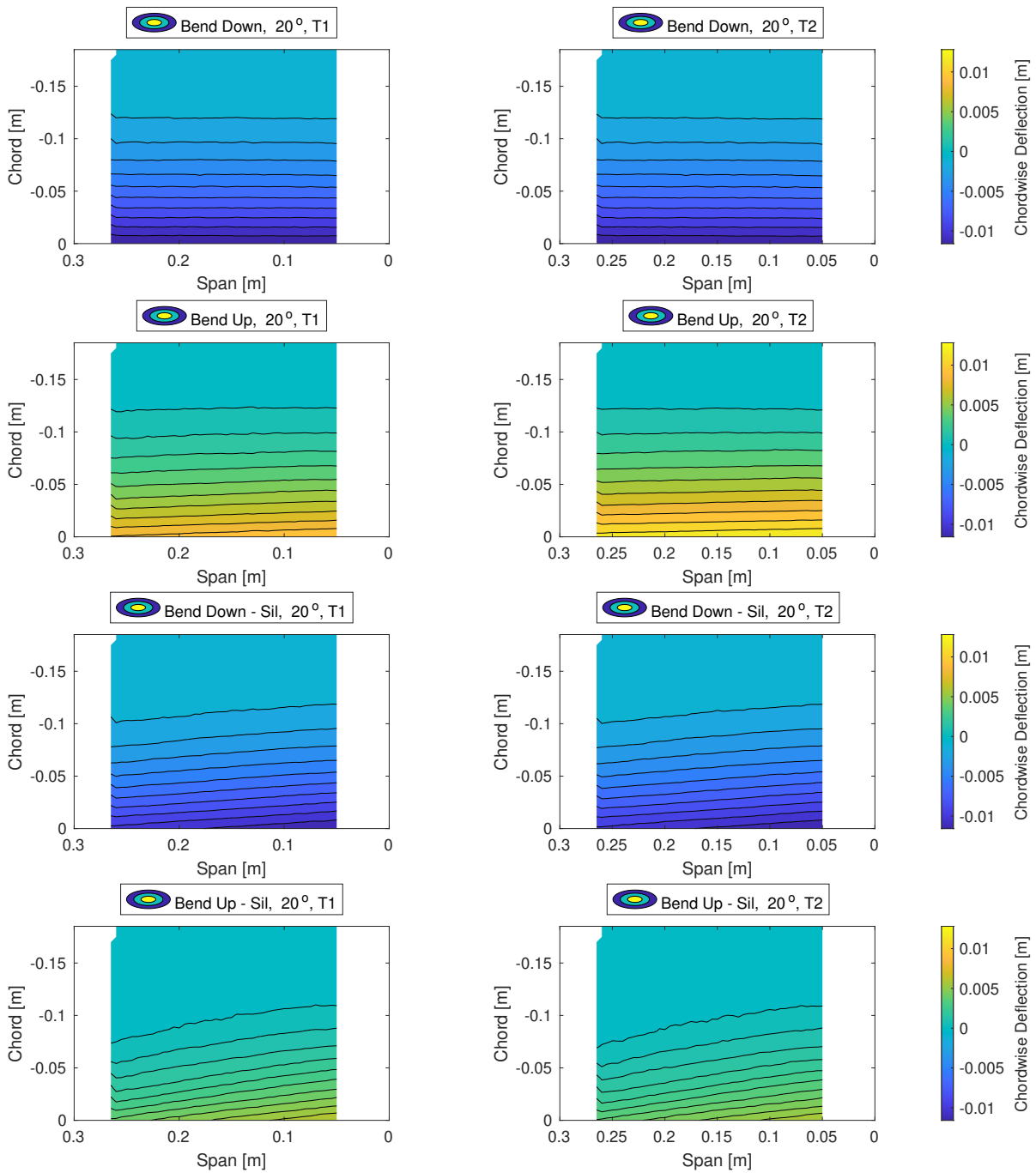


Figure C.20: Chordwise translation measurements on top surface surface for all tests at 20° actuation

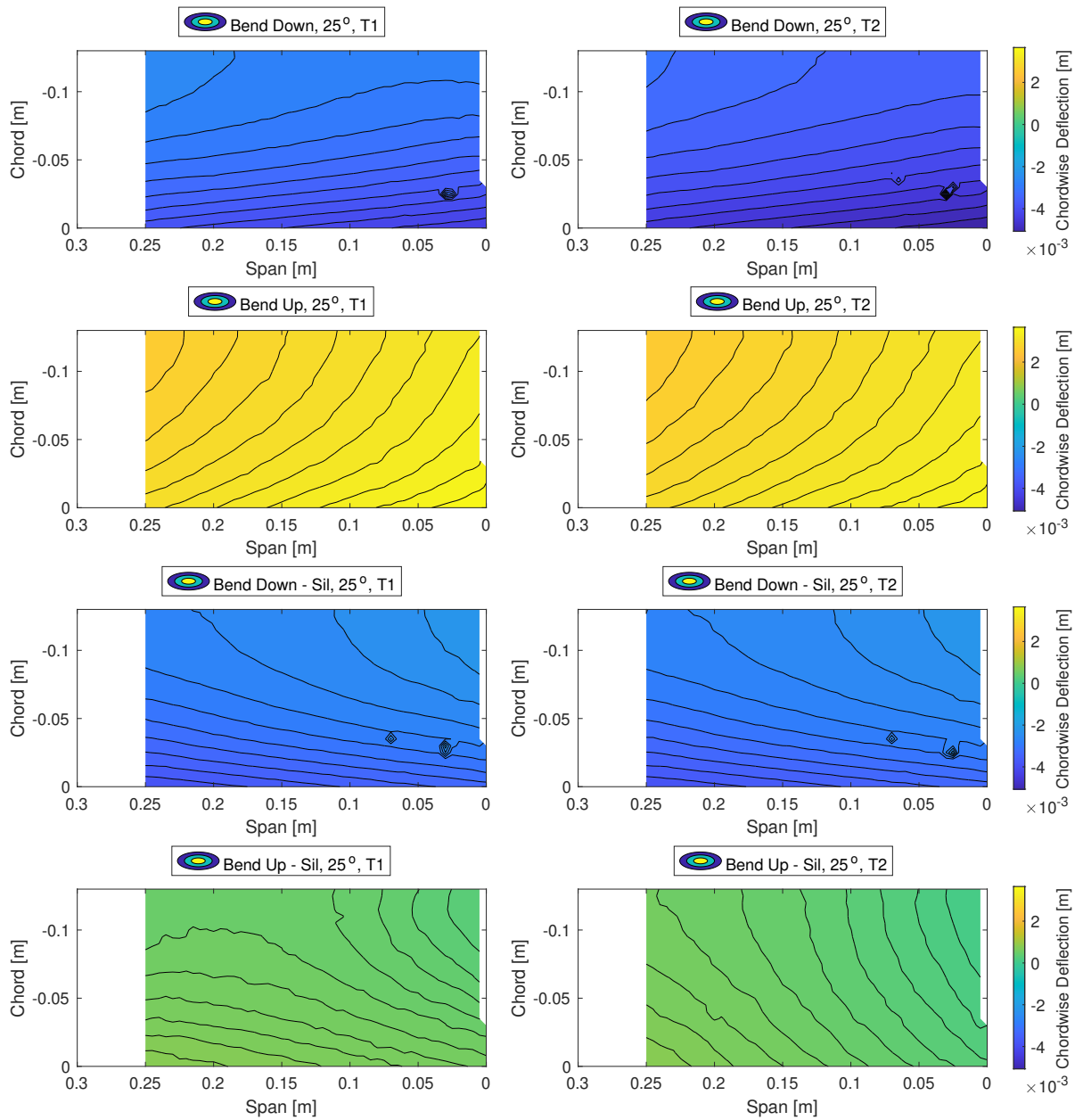


Figure C.21: Chordwise translation measurements on bottom surface for all tests at 25° actuation

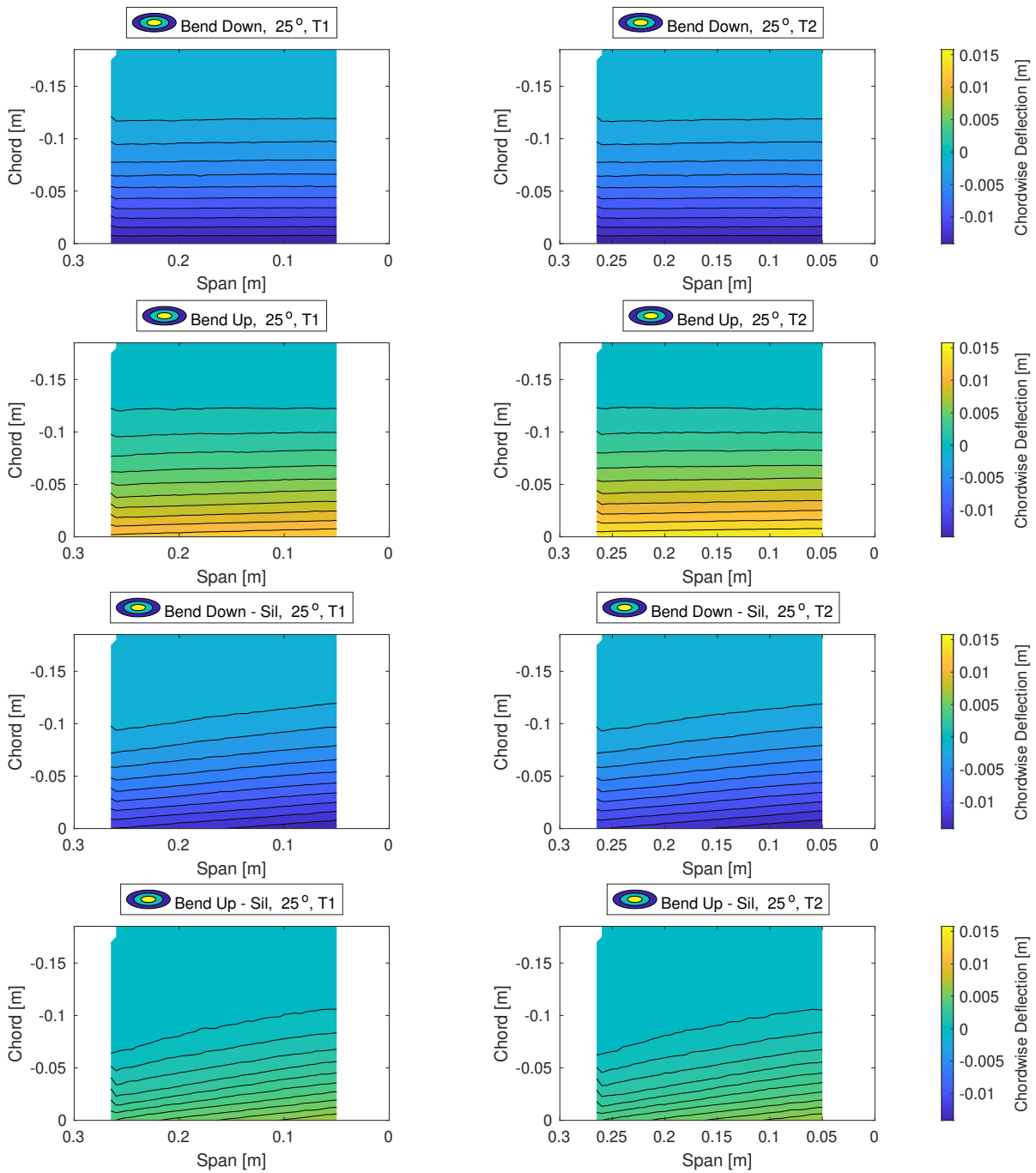


Figure C.22: Chordwise translation measurements on top surface surface for all tests at 25° actuation

Bibliography

- [1] URL <https://www.permabond.com/resource-center/silicone-bonding/>.
- [2] URL <https://www.flxsys.com/>.
- [3] . URL <https://www.mscsoftware.com/product/msc-nastran>.
- [4] . URL <https://www.ansys.com/>.
- [5] . URL <https://nl.mathworks.com/products/matlab.html>.
- [6] . URL <https://hypersizer.com/>.
- [7] . URL <https://www.esteco.com/modelfrontier>.
- [8] . URL <https://www.altair.com/optistruct/>.
- [9] URL <https://www.dow.com/content/dam/dcc/documents/en-us/tech-art/11/11-37/11-3716-01-durometer-hardness-for-silicones.pdf?iframe=true>.
- [10] URL <https://www.viba.nl/nl/catalog/lijmen-tapes/flexibele-lijmen-kitten/siliconen/wacker/groups/g+c+p+t+view>.
- [11] URL <https://volz-servos.com/produkte/standard/>.
- [12] Quertriebskoerper mit veraenderbarer profilierung, insbesondere flugzeugtragfluegel, 1979.
- [13] 2008. URL https://www.mscsoftware.com/assets/MDNastran_DS.pdf.
- [14] Digital morphing wing, 2016. URL <https://news.mit.edu/2016/morphing-airplane-wing-design-1103>.
- [15] 2019. URL <https://www.3ds.com/products-services/simulia/products/abaqus/abaquscae/>.
- [16] ACARE. Strategic research & innovation agenda, 2017 update. Report, ACARE, 2017.
- [17] Altair. Hyperworks 13.0 optistruct user's guide. Report, 2014.
- [18] Silvestro Barbarino, Onur Bilgen, Rafic Ajaj, Michael Friswell, and Daniel Inman. A review of morphing aircraft. *Journal of Intelligent Material Systems and Structures - J INTEL MAT SYST STRUCT*, 22, 2011. doi: 10.1177/1045389X11414084.
- [19] Onur Bilgen and Michael I Friswell. Piezoceramic composite actuators for a solid-state variable-camber wing. *Journal of Intelligent Material Systems and Structures*, 25(7):806–817, 2014. doi: 10.1177/1045389x13500575. URL <https://journals.sagepub.com/doi/abs/10.1177/1045389X13500575>.
- [20] Onur Bilgen, Michael Friswell, Kevin Kochersberger, and Daniel Inman. Surface actuated variable-camber and variable-twist morphing wings using piezocomposites. *Collection of Technical Papers - AIAA/ASME/ASCE/AHS/ASC Structures, Structural Dynamics and Materials Conference*, 2011. doi: 10.2514/6.2011-2072.

- [21] Onur Bilgen, Lauren M Butt, Steven R Day, Craig A Sossi, Joseph P Weaver, Artur Wolek, William H Mason, and Daniel J Inman. A novel unmanned aircraft with solid-state control surfaces: Analysis and flight demonstration. *Journal of Intelligent Material Systems and Structures*, 24(2):147–167, 2013. doi: 10.1177/1045389X12459592. URL <https://doi.org/10.1177/1045389X12459592>.
- [22] Edward A. Bubert, Benjamin K.S. Woods, Keejoo Lee, Curt S. Kothera, and N.M. Wereley. Design and fabrication of a passive 1d morphing aircraft skin. *Journal of Intelligent Material Systems and Structures*, 21(17):1699–1717, 2010. doi: 10.1177/1045389x10378777. URL <https://journals.sagepub.com/doi/abs/10.1177/1045389X10378777>.
- [23] Nicholas B. Cramer, Daniel W. Cellucci, Olivia B. Formoso, Christine E. Gregg, Benjamin E. Jenett, Joseph H. Kim, Martynas Lendraitis, Sean S. Swei, Greenfield T. Trinh, Khanh V. Trinh, and Kenneth C. Cheung. Elastic shape morphing of ultralight structures by programmable assembly. *Smart Materials and Structures*, 28(5):055006, 2019. ISSN 0964-1726 1361-665X. doi: 10.1088/1361-665x/ab0ea2. URL <http://dx.doi.org/10.1088/1361-665X/ab0ea2>.
- [24] Stephen Daynes and Paul Weaver. Morphing Blade Fluid-Structure Interaction. *Structures, Structural Dynamics, and Materials and Co-located Conferences*. American Institute of Aeronautics and Astronautics, 2012. doi: doi:10.2514/6.2012-166710.2514/6.2012-1667. URL <https://doi.org/10.2514/6.2012-1667>.
- [25] Iman Dayyani, Michael Friswell, Hamed Khodaparast, and Benjamin Woods. The design of a corrugated skin for the fishbac compliant structure. 22nd AIAA/ASME/AHS Adaptive Structures Conference, 2014.
- [26] Alessandro De Gaspari and Sergio Ricci. A two-level approach for the optimal design of morphing wings based on compliant structures. *Journal of Intelligent Material Systems and Structures*, 22(10):1091–1111, 2011. ISSN 1045-389X. doi: 10.1177/1045389X11409081. URL <https://doi.org/10.1177/1045389X11409081>.
- [27] Mark Drela. Xfoil: An analysis and design system for low reynolds number airfoils. *Low Reynolds Number Aerodynamics*, pages 1–12. Springer Berlin Heidelberg. ISBN 978-3-642-84010-4.
- [28] W. R. Graham, C. A. Hall, and M. Vera Morales. The potential of future aircraft technology for noise and pollutant emissions reduction. *Transport Policy*, 34:36–51, 2014. ISSN 0967-070X. doi: <https://doi.org/10.1016/j.tranpol.2014.02.017>. URL <http://www.sciencedirect.com/science/article/pii/S0967070X14000481>.
- [29] Ashwin C. Henry, Giulio Molinari, Jose R. Rivas-Padilla, and Andres F. Arrieta. Smart morphing wing: Optimization of distributed piezoelectric actuation. *AIAA Journal*, 57(6):2384–2393, 2019. doi: 10.2514/1.J057254. URL <https://arc.aiaa.org/doi/abs/10.2514/1.J057254>.
- [30] Benjamin Jenett, Sam Calisch, Daniel Cellucci, Nick Cramer, Neil Gershenfeld, Sean Swei, and Kenneth C. Cheung. Digital morphing wing: Active wing shaping concept using composite lattice-based cellular structures. *Soft Robotics*, 4(1):33–48, 2016. ISSN 2169-5172. doi: 10.1089/soro.2016.0032. URL <https://doi.org/10.1089/soro.2016.0032>.
- [31] H. JEX and F. CULICK. Flight control dynamics of the 1903 Wright Flyer. doi: 10.2514/6.1985-1804. URL <https://arc.aiaa.org/doi/abs/10.2514/6.1985-1804>.
- [32] Michael Kikuta. Mechanical properties of candidate materials for morphing wings. 2004.
- [33] Markus Kintscher, S. Geier, H. P. Monner, and M. Wiedemann. Investigation of multi-material laminates for smart droop nose devices.
- [34] Sridhar Kota, Peter Flick, and Fayette S. Collier. Flight Testing of FlexFloilTM Adaptive Compliant Trailing Edge. doi: 10.2514/6.2016-0036. URL <https://arc.aiaa.org/doi/abs/10.2514/6.2016-0036>.

- [35] Sridhar Kota, Joel Hetrick, Russell Osborn, Donald Paul, Edmund Pendleton, Peter Flick, and Carl Tilmann. Design and application of compliant mechanisms for morphing aircraft structures. *Proc SPIE*, 5054, 2003. doi: 10.1117/12.483869.
- [36] Guohong Li, Erasmo Carrera, Maria Cinefra, Alberto G. de Miguel, Gennady M. Kulikov, Alfonso Pagani, and Enrico Zappino. Evaluation of shear and membrane locking in refined hierarchical shell finite elements for laminated structures. *Advanced Modeling and Simulation in Engineering Sciences*, 6(1):8, 2019. ISSN 2213-7467. doi: 10.1186/s40323-019-0131-1. URL <https://doi.org/10.1186/s40323-019-0131-1>.
- [37] Eli Livne, Nathan Precup, and Marat Mor. Design, Construction, and Tests of an Aeroelastic Wind Tunnel Model of a Variable Camber Continuous Trailing Edge Flap (VCCTEF) Concept Wing. doi: 10.2514/6.2014-2442. URL <https://arc.aiaa.org/doi/abs/10.2514/6.2014-2442>.
- [38] G. Molinari, M. Quack, V. Dmitriev, M. Morari, P. Jenny, and P. Ermanni. Aero-structural optimization of morphing airfoils for adaptive wings. *Journal of Intelligent Material Systems and Structures*, 22(10):1075–1089, 2011. ISSN 1045-389X. doi: 10.1177/1045389X11414089. URL <https://doi.org/10.1177/1045389X11414089>.
- [39] Giulio Molinari, Andres F. Arrieta, and Paolo Ermanni. Aero-structural optimization of three-dimensional adaptive wings with embedded smart actuators. *AIAA Journal*, 52(9):1940–1951, 2014. doi: 10.2514/1.J052715. URL <https://arc.aiaa.org/doi/abs/10.2514/1.J052715>.
- [40] MSC. Msc nastran design sensitivity and optimization user's guide. Report, 2018.
- [41] MSC. Msc nastran quick reference guide. Report, 2018.
- [42] Nhan Nguyen, Nathan Precup, Eli Livne, James Urnes, Eric Dickey, Chester Nelson, Jonathan Chiew, David Rodriguez, Eric Ting, and Sonia Lebofsky. Wind Tunnel Investigation of a Flexible Wing High-Lift Configuration with a Variable Camber Continuous Trailing Edge Flap Design. 2015. doi: 10.2514/6.2015-2417.
- [43] Kingnidé R. Olympio and Farhan Gandhi. Flexible skins for morphing aircraft using cellular honeycomb cores. *Journal of Intelligent Material Systems and Structures*, 21(17):1719–1735, 2009. ISSN 1045-389X. doi: 10.1177/1045389X09350331. URL <https://doi.org/10.1177/1045389X09350331>.
- [44] Alexander Pankonien, Cassio Faria, and Daniel Inman. Synergistic smart morphing aileron: Experimental quasi-static performance characterization. *Journal of Intelligent Material Systems and Structures*, 26, 2014. doi: 10.1177/1045389X14538530.
- [45] Francesco Previtali, Andres F. Arrieta, and Paolo Ermanni. Performance of a three-dimensional morphing wing and comparison with a conventional wing. *AIAA Journal*, 52(10):2101–2113, 2014. doi: 10.2514/1.J052764. URL <https://arc.aiaa.org/doi/abs/10.2514/1.J052764>.
- [46] Jurij Sodja, Marcias J Martinez, John C Simpson, and Roeland De Breuker. Experimental evaluation of a morphing leading edge concept. *Journal of Intelligent Material Systems and Structures*, 30(18-19):2953–2969, 2019. doi: 10.1177/1045389x19862369. URL <https://journals.sagepub.com/doi/abs/10.1177/1045389X19862369>.
- [47] G.B. Spirlet. Design of Morphing Leading and Trailing Edge Surfaces for Camber and Twist Control. Thesis, 2015.
- [48] C. Thill, Julie Etches, Ian Bond, Kevin Potter, and Paul Weaver. Morphing skins. *Aeronautical Journal*, 112:117–139, 2008. doi: 10.1017/S000192400002062.
- [49] G. A. A. Thuwis, M. M. Abdalla, and Z. Gürdal. Optimization of a variable-stiffness skin for morphing high-lift devices. *Smart Materials and Structures*, 19(12):124010, 2010. ISSN 0964-1726 1361-665X. doi: 10.1088/0964-1726/19/12/124010. URL <http://dx.doi.org/10.1088/0964-1726/19/12/124010>.

- [50] D. F. Watson. *Contouring: a guide to the analysis and display of spatial data*. Contouring: a guide to the analysis and display of spatial data, 1992. ISSN 00983004. doi: 10.1016/0098-3004(93)90069-h.
- [51] Noud Werter, Jurij Sodja, Gregory Spirlet, and Roeland De Breuker. Design and Experiments of a Warp Induced Camber and Twist Morphing Leading and Trailing Edge Device. doi: 10.2514/6.2016-0315. URL <https://arc.aiaa.org/doi/abs/10.2514/6.2016-0315>.
- [52] Benjamin Woods, Michael Friswell, and Onur Bilgen. Wind tunnel testing of the fishbone active camber morphing concept. *Journal of Intelligent Material Systems and Structures*, 25, 2014. doi: 10.1177/1045389X14521700.
- [53] Benjamin K. S. Woods, Michael I. Friswell, and Norman M. Wereley. Advanced kinematic tailoring for morphing aircraft actuation. *AIAA Journal*, 52(4):788–798, 2014. doi: 10.2514/1.J052808. URL <https://arc.aiaa.org/doi/abs/10.2514/1.J052808>.
- [54] Benjamin K. S. Woods, Iman Dayyani, and Michael I. Friswell. Fluid/structure-interaction analysis of the fish-bone-active-camber morphing concept. *Journal of Aircraft*, 52(1):307–319, 2015. doi: 10.2514/1.C032725. URL <https://arc.aiaa.org/doi/abs/10.2514/1.C032725>.